

**THERMOTECTONIC EVOLUTION OF THE NORTHERN MONASHEE
COMPLEX, SOUTHERN OMINECA BELT, SOUTHEASTERN BRITISH
COLUMBIA**

by

H. Daniel Gibson

**A thesis submitted to the Faculty of
Graduate Studies and Research in partial fulfillment
of the requirements for the degree of
Master of Science, Department of Earth Sciences**

Carleton University

Ottawa, Ontario

May 1997

©copyright

May 5, 1997, H. Daniel Gibson

The undersigned hereby recommend to the Faculty of Graduate
Studies and Research acceptance of the thesis
“Thermotectonic Evolution of the Northern Monashee
Complex, Southern Omineca Belt, Southeastern British
Columbia”

Chairman, Department of Earth Sciences

Thesis Co-supervisor

Thesis Co-supervisor

Carleton University
May 5, 1997

ABSTRACT

Recent geochronologic and structural investigations have provided new knowledge of U-Th-Pb systematics for monazite in high-grade terranes and new constraints specifically for thermotectonic modeling of the northern Monashee complex within the southeastern Canadian Cordillera. Of particular importance to this study and the model is the Sibley Creek syncline (SCS), located within the footwall of a major crustal-scale thrust fault termed the Monashee décollement (MD). The SCS belongs to a regional-scale fold system which dominates the western part of the complex and controls map-scale distribution of lithologies. These structures represent the earliest stages of Cordilleran deformation within the complex. Also found within the footwall associated with the SCS is evidence of inverted amphibolite-facies metamorphism, with higher-grade sillimanite-K-feldspar gneiss and extensive anatexis in the immediate hanging wall. Constraining the timing for the deformation and metamorphism within the footwall is an essential requirement for developing a thermotectonic model of the region.

Monazite and zircon extracted from six samples taken at systematically deeper structural levels within the footwall were dated by U-Th-Pb isotope dilution using a mixed U-Th-Pb spike to (1) test the assumption that excess ^{206}Pb is the only significant cause of reverse discordance, (2) to assess the extent of Th-U mobility in monazite and zircon, and (3) arrive at more confident interpretations of crystallization age via the additional Th-Pb decay system.

All analyses were sequentially assessed, and it was discovered that approximately 40% of the monazite analyses demonstrate relative U loss of 2-7%, resulting in exaggerated U-Pb ages. Additionally, it was found that structurally higher samples have increasingly complex systematics with evidence of U loss, preservation of excess ^{206}Pb , and a substantial spread of ages of up to 10 Ma (resulting from Pb loss and/or protracted crystal growth), with older ages at highest levels closest to the overlying allochthon. Conversely, the structurally lowest sample has the simplest systematics, with complete agreement between four analyses and little or no evidence for Th-U mobility. This sample also demonstrates that reverse discordance can be explained entirely by initial incorporation of excess ^{230}Th . Necessary corrections and changes to the Pb/U ages were performed to account for the excess ^{206}Pb and U loss.

The U-Th-Pb chronometry also revealed a systematic younging of peak metamorphic ages (from ca. 77 to 59 Ma) with increased structural depth across the SCS. The restricted structural distance between the above ages (1.7-2.5 km) is not compatible with previous models which proposed that the preservation of inverted metamorphism was accomplished primarily by heat transfer from an overlying heat source (i.e., Selkirk allochthon). The data require that the inversion of ages and isograds was primarily accomplished mechanically. Therefore, a coupled thermomechanical model is proposed in which substantial easterly directed shear strain and attendant attenuation in the footwall led to relative lateral transfer of rocks preserving evidence of diachronous metamorphism. This model incorporates a clear role for shear strain and a probable but less important role for heat transfer from the allochthon. Thermochronologic and structural data suggest that the SCS initiated in pre-peak metamorphic conditions and was modified by diachronous and penetrative syn-peak metamorphic deformation. Thus, in its earliest stages the SCS evolved in a cool environment, possibly as a buckle fold. With

progressive burial and heating the SCS approximated a passive flow fold; during this flow hot rocks at deeper structural levels were translated eastward resulting in the present fold geometry. This model accounts for the diachronous upward increase in peak metamorphic ages within the footwall across the SCS while requiring negligible downward transmission of heat from the overlying allochthon.

Significant implications of these data are the following: (1) U loss in monazite is not detectable using only U-Pb dating; if U loss is present, U-Pb dates will be inflated. This situation is entirely cryptic without Th-Pb measurements. There seems little doubt this previously undetected problem has clouded interpretations of many monazite U-Pb studies. (2) The apparent inversion of metamorphic ages and isograds within this part of the complex was accomplished primarily by thermally aided deformation requiring negligible heat transfer from the overthrust allochthon.

ACKNOWLEDGEMENTS

Fieldwork and U-Pb laboratory procedures were supported by the Geological Survey of Canada (GSC) and NSERC operating grants to R.R. Parrish and R.L. Brown, respectively. Randy Parrish and Richard Brown are thanked for their patience and for co-supervision of the thesis. Both provided excellent insight, guidance, input, and critical reviewing of the thesis. Special thanks are extended to Randy Parrish who very patiently guided me through all the geochemical and mass spectrometry aspects of the study and provided much insight that helped with the geochronologic interpretations made in this study. Thanks to Jim Crowley for help with geochronology sample preparation at Carleton University and insightful discussions concerning all aspects of this thesis. Additional expertise in this area provided by Sharon Carr is gratefully acknowledged. Jesse Coburn is recognized for providing excellent assistance and comic relief in the field. Dennis “Rainman” Johnston is thanked for the stimulating radio conversations. Paul Williams and Richard Brown are thanked for their sagacious and sometimes amusing outcrop discussions. I am grateful for the expert helicopter support provided by Duncan Wassick and his crew at Canadian Helicopters, Revelstoke, BC. Many thanks to Lois Hardy for help with the manuscript. I gratefully acknowledge James “The Chief” McLelland and all other people who piqued my interest in geology and had an integral part in fostering its growth. Thanks are extended to Mr. and Mrs. P. Cheney for their generosity. I extend my gratitude to both of my older brothers who were my role models growing up and are largely responsible for my motivation in life (as well as a few cuts, bruises, and scars). I especially thank my mom and dad for their patience, understanding, and sage advice. Last, I would like to extend very special thanks and gratitude to Yolande Cheney for her unwavering support.

ORIGINAL CONTRIBUTIONS

During two months of fieldwork in the summer of 1995 I mapped lithologies, structures, and metamorphic assemblages and collected geochronologic samples at 1:10 000 scale in the following 1:20 000 sheets (North American Datum 1983, UTM zone 11): 82M.056, 82M.057, 82M.066, and 82M.067. These data were compiled with previous detailed mapping (1:15 000) by Scammell (1986) to produce a composite lithological and structural map of northern Frenchman Cap dome. Additionally, for the purposes of this study the data were applied to a more regional data base which included the work of Brown (1980), Journeay (1986), and Scammell (1986). All samples collected for petrography and geochronology were collected by myself and my field assistant Jesse Coburn. I selected, cut, and polished all thin section chips, which were then precisely ground and mounted by Anett Briggs. I performed all thin section analyses for this study. For the geochronologic component of this study, I performed both U-Pb and Th-Pb chronometry on four pelitic schist samples, one cross-cutting mafic dyke, and one pyroclastic horizon, from which a total of 28 fractions of monazite and zircon were analyzed. I performed all stages of crushing, grinding, and mineral separation at Carleton University. The picking of fractions, U-Pb and Th-Pb chemistry, and mass spectrometry were performed by myself at the Geologic Survey of Canada under the guidance of Dr. R.R. Parrish. I created a spread sheet program in Excel Version 5.0[®] capable of performing the functions necessary for Th-Pb data reduction and estimation of Pb/Th age errors based on isotope dilution equations from Faure (1986) and principles established by Roddick (1987), respectively. With the help of Dr. R.R. Parrish, I formulated all the equations presented in this thesis based on principles established by various workers who have been referenced accordingly.

TABLE OF CONTENTS

	Page
ACCEPTANCE SHEET	ii
ABSTRACT	iii
ACKNOWLEDGEMENTS	v
ORIGINAL CONTRIBUTIONS	vi
TABLE OF CONTENTS	vii
LIST OF TABLES	
viii	
LIST OF FIGURES AND MAPS	ix
LIST OF PLATES	ix
LIST OF APPENDICES	x
 CHAPTER 1. Introduction	 1
Foreword.....	1
The Canadian Cordillera and the Monashee complex.....	1
Previous models.....	2
Study objectives.....	3
 CHAPTER 2. U-Th-Pb systematics in metamorphic terranes using Th-Pb and U-Pb chronometry: northern Monashee complex, southeastern Canadian Cordillera	 5
Introduction.....	5
Geologic setting.....	6
Geochronology.....	7
Analytical methodology	7
Additional Th-Pb procedures.....	8
Background of samples.....	10
Monazite analyses.....	11
DG-105-95.....	11
DG-136-95.....	12
DG-122-95.....	12
DG-167-95.....	12
Zircon analyses.....	13
DG-107-95.....	13
DG-118-95.....	13
Isotopic results.....	14
DG-167-95.....	14
DG-136-95.....	15
DG-105-95.....	16
DG-122-95.....	16
DG-107-95.....	16
DG-118-95.....	17
U-Th-Pb systematics.....	18

	Page
Excess ^{206}Pb and relative Th-U Mobility.....	19
Correction for ^{206}Pb	20
Correction for U loss.....	22
Dispersion of data in U-Th-Pb space.....	25
Residual dispersion of data, DG-167-95.....	27
Possible mechanisms affecting DG-136,-105, & -122-95.....	28
Complexities associated with U loss correction.....	31
Summary of U-Th-Pb systematics.....	32
Apparent metamorphic age inversion.....	33
Further complexities in Pb/U age interpretations.....	34
Possible thermotectonic model.....	35
Conclusions.....	36
 CHAPTER 3. Thermotectonic evolution of the Sibley Creek syncline, northern Monashee complex, southeastern Canadian Cordillera.....	 50
Introduction.....	50
Geologic setting.....	51
Structural setting of the footwall: northern Monashee complex.....	53
Summary.....	58
Timing constraints of deformation and metamorphism.....	59
Summary of geochronology.....	59
DG-105-95.....	60
DG-136-95.....	60
DG-122-95.....	61
DG-167-95.....	61
Timing of deformation and metamorphism.....	62
Thermotectonic models.....	63
Apparent metamorphic age inversion.....	63
Rapid Paleocene burial and Eocene denudation.....	64
Problems with heat transfer model.....	66
Coupled thermomechanical model.....	67
Summary of current thermotectonic model.....	69
Conclusions.....	70
 CHAPTER 4. Summary of conclusions.....	 91
 REFERENCES.....	 94

LIST OF TABLES

Table 2-1. U-Th-Pb analytical data.....	38
Table 2-2. Determination of $(\text{Th}/\text{U})_{\text{'metamorphic fluid'}}$ Values.....	39

LIST OF FIGURES AND MAPS

	Page
Figure 2-1. Tectonic map of southern Omineca Belt.....	40
Figure 2-2. Lithologic compilation of northern Frenchman Cap dome.....	42
Figure 2-3. Generalized cross section of the Sibley Creek syncline.....	43
Figure 2-4. U-Th-Pb concordia diagrams.....	44
Figure 2-4. U-Th-Pb concordia diagrams, continued.....	45
Figure 2-5. Corrected U-Th-Pb concordia diagrams.....	46
Figure 2-5. Corrected U-Th-Pb concordia diagrams, continued.....	47
Figure 2-6. Concordia plot for DG-118-95 with modified York regression through fractions G, A, and C.....	48
Figure 2-7. Hypothetical concordia diagram for monazite experiencing continuous Pb- loss.....	48
Figure 2-8. Metamorphic age versus depth below Monashee décollement plot.....	49
Figure 3-1. Tectonic map of southern Omineca Belt.....	72
Figure 3-2. Geologic compilation map of Frenchman Cap dome.....	73
Figure 3-3. Cross section of northern Frenchman Cap dome.....	74
Figure 3-4. Lithologic compilation of northern Frenchman Cap dome.....	76
Figure 3-5. Diagrammatic table of structural elements for northern Monashee complex.....	77
Figure 3-6. Structural map and stereonet plots for current study.....	78
Figure 3-7a. Generalized cross section (A-B) of the Sibley Creek syncline.....	79
Figure 3-7b. Generalized cross section (C-D) of the Sibley Creek anticline and syncline.....	80
Figure 3-8. Metamorphic age versus depth below Monashee décollement plot.....	81
Figure 3-9. Thermotectonic model for the Monashee complex.....	83
Map 1. Station location map for current study.....	back pocket
Map 2. Color lithologic compilation map for northern Monashee complex.....	back pocket
Map 3. Structural map.....	back pocket

LIST OF PLATES

Plate 3-1. Profile of the Sibley Creek syncline.....	84
Plate 3-2. Cross bedding preserved in overturned limb of SCS.....	85
Plate 3-3. Second generation (D2) S-fold parasitic to SCS.....	86
Plate 3-4. Second generation (D2) U-fold parasitic to SCS with first generation (D1) foliation surface folded around the hinges.....	87
Plate 3-5. Third generation (D3) folds refolded by fourth generation (D4) folds.....	88
Plate 3-6. Two examples of characteristic D4 fold geometries.....	89
Plate 3-7. Brittle normal fault assigned to the fifth generation of deformation (D5).....	90

APPENDICES

	Page
Appendix 1. Errors for Th-Pb chronometry.....	100
Appendix 2. Description of spike preparation.....	102
Appendix 3. Pb/Th age calculations.....	103
Appendix 4. Calculations for Pb/U and/or Pb/Th ages corrected for U loss.....	107
Appendix 5. Minerals identified in thin section and hand specimen.....	111

Chapter 1. Introduction

Foreword

The purpose of this thesis is to present data that test previous models of orogenic processes, with particular focus on the Monashee complex of the southeastern Canadian Cordillera. Chapters 2 and 3 have been written in paper format. Both have relevance to each other and should not be considered as separate entities. Chapter 2 focuses on geochronology with emphasis on the U-Th-Pb systematics of monazite and zircon. Chapter 3 describes the structural elements of the northern Monashee complex and draws upon conclusions of Chapter 2 to constrain the timing of deformation and metamorphism for the purpose of constructing a thermotectonic model.

The Canadian Cordillera and the Monashee complex

The orogenic evolution of the Canadian Cordillera involved a protracted and complex interplay between rifting (Sears and Price 1978, Scammell and Brown 1990), contraction, and extension (Gabrielse and Yorath 1992 and references therein). Many questions remain to be addressed, and it is generally agreed that deeper crustal levels must be evaluated in order to find answers. As a result, much emphasis has been focused upon the Monashee complex, located in the southern Omineca Belt (Fig. 2-1), where some of the deepest levels within the Cordillera are exposed. The unique preservation of deep-seated thrusting and related thermal events provides an excellent laboratory for studying mid-crustal orogenic processes. Thus, in the recent past there has been extensive regional

mapping (e.g., Wheeler 1965, McMillan 1970, Reesor and Moore 1971, Brown 1980, Höy and Brown 1980, Read 1980, Read and Brown 1981, Höy 1982, Journeay 1986, McNicoll and Brown 1995), geochronologic dating (Parrish 1995 and references therein, J.L. Crowley unpublished data 1997), metamorphic studies (Journeay 1986, Scammell 1986), and Lithoprobe deep seismic reflection imaging (Cook et al. 1992 and references therein) conducted throughout the complex.

Previous models

In the past decade, modeling of the complex has evolved substantially. It is generally agreed that the complex was buried during crustal thickening associated with the Cordilleran orogeny (170 - 50 Ma), but the timing of initial burial and metamorphism remains uncertain. Brown (1980) first suggested that burial occurred as early as the Jurassic. Journeay (1986) and Brown et al. (1986) modified this idea by proposing a duplex model of crustal thickening of the complex beneath the Selkirk allochthon. This model implied eastwardly displacement developing in the Jurassic and progressing into the Tertiary. The complex was modeled as being exhumed initially during the late stages of compression with final exhumation occurring as the result of extension and tectonic denudation in the Eocene (Brown and Journeay 1987). More recently using structural arguments based on crustal cross sections and palinspastic restorations, Johnson and Brown (1996) suggested that the complex was deeply buried during Cretaceous time followed by partial exhumation during the Late Cretaceous. Final exhumation from middle crustal depths (~12 km) was facilitated by Tertiary extension.

Parrish (1995) reinterpreted the tectonic history of the complex based on new geochronologic data. He argued that the complex is autochthonous and was not deeply

buried until Paleocene time. Parrish proposed that rapid burial beneath the hot Selkirk allochthon, followed by exhumation in the Paleocene to Eocene allowed for the inversion and preservation of the present-day metamorphic isograds.

Study objectives

To test the above-mentioned models this study is focused on the northern flank of the Monashee complex (Fig 2-2) where the Sibley Creek syncline (SCS) has been mapped by Brown (1980), Journeay (1986), and Scammell (1986). This structure is thought to be part of a regional-scale easterly vergent isoclinal fold system that includes, from south to north, the Mount Grace syncline, the Kirbyville anticline, and the Sibley Creek syncline (Figs. 2-1c, 2-2, and 3-2) whose axial surfaces dip moderately away from the complex toward the northwest and southwest (Brown 1980). These folds involve both the basement and cover sequence lithologies and are thought to be concomitant with the earliest phases of Cordilleran deformation recorded in the complex (Journeay 1986, Scammell 1986). Therefore, knowledge of the timing of the SCS relative to related structures and metamorphism is an essential requirement for developing a tectonic model of the region.

Detailed mapping (1:10 000) and geochronology were carried out during this study to further complement the data base already established for this part of the complex. Additionally, during this study Th-Pb chronometry and dual U-Pb analyses were performed on a suite of high-grade metamorphic rocks. This was done in order to test previous assumptions concerning U-Th-Pb systematics in monazite and zircon, as well as to attempt to arrive at more confident interpretations of crystallization age via the additional Th-Pb decay system. Samples were collected at systematically deeper

structural levels within the footwall lithologies of the complex across the SCS as a further test of the diachroneity of the metamorphism and deformation within this part of the complex.

The goals of this thesis are as follows:

- (1) To present the geochronologic, structural, and metamorphic elements of the SCS area.
- (2) To examine the U-Th-Pb systematics of monazite and zircon using U-Th-Pb chronometry and determine possible avenues for correcting any U-Th-Pb disturbance that may be affecting the minerals; also, to consider what implications this may have with regards to interpretations made in this and other studies.
- (3) To constrain the timing of deformation and metamorphism by drawing upon the superposition of structures, fabrics, and metamorphic assemblages in conjunction with the U-Th-Pb geochronology.
- (4) To apply these data to a more regional scale in order to test previous models and, if necessary, propose a new model that accounts for the thermotectonic evolution of the northern Monashee complex.

Chapter 2. U-Th-Pb systematics in metamorphic terranes using Th-Pb and U-Pb chronometry: northern Monashee complex, southeastern Canadian Cordillera

Introduction

Accurate thermal and deformational chronology is essential to construct viable tectonic models of orogenic belts and processes. In particular, coupled U-Pb analyses (^{235}U - ^{207}Pb and ^{238}U - ^{206}Pb) on accessory minerals such as zircon and monazite have been extensively used and accepted as reliable chronometers for constraining ages of magmatism, metamorphism, and deformation. Because U-Pb analyses have the potential to resolve detailed events with high precision, the faith in and the importance pinned to the ages produced have increased proportionally with the evolution of the analytical precision and accuracy attained in the last few decades. Thus, the interpretations accompanying U-Pb studies that yield seemingly straightforward data are usually accepted with little hesitation. However, as this chapter will show, there are situations where data can be misleading when only the U-Pb chronometer is used in the analyses of rocks that experienced a complex thermal history or that have been disturbed.

Consider the case of monazite, a Th-rich mineral, which commonly plots as reversely discordant data with conspicuously low or negative $^{207}\text{Pb}/^{206}\text{Pb}$ ages. This phenomenon is thought to be the result of an excess accumulation of ^{206}Pb in monazite due to a large component of ^{230}Th incorporated during crystallization, causing low $^{207}\text{Pb}/^{206}\text{Pb}$ ages concurrent with reverse discordance produced by an exaggerated $^{206}\text{Pb}/^{238}\text{U}$ ratio (Schärer 1984, Parrish 1990). Schärer outlines a procedure that corrects for this disequilibrium effect using measurements of Th/U ratios of the monazite and of the

magma from which it crystallized. This concept is widely applied in monazite geochronology even though it is based on theoretical assumptions that have never been rigorously tested. Additionally, the potential relative mobility of U and Th have not been addressed.

To address these problems, a suite of high-grade metamorphic rocks (upper amphibolite to granulite facies) from the northern flank of the Monashee complex of southeastern British Columbia (Figs. 2-1 and 2-2) were studied. ^{232}Th - ^{208}Pb analyses were carried out in conjunction with U-Pb chronometry in an attempt to more fully understand the U-Th-Pb systematics. Since the intermediate daughter isotopes in the ^{232}Th - ^{208}Pb decay chain are short-lived, the ^{232}Th - ^{208}Pb chronometer does not suffer from significant unsupported daughter isotopic complexities and should yield correct ages. Using these chronometers together allows for an evaluation of the explanation for monazite discordance in U-Pb space (Schärer 1984, Parrish 1990) and also provides a means to examine the possibility of U and/or Th loss or gain as a mechanism in monazite systematics. The Th-Pb dating technique was applied to zircon as well. The focus of this chapter is to present the newly acquired data and their interpretations in order to provide additional insight into monazite-zircon systematics, U-Th leaching, and Pb loss, and their relevance to past and future geochronologic studies.

Geologic setting

I have chosen a study area containing amphibolite-facies metamorphic rocks within the footwall of a major crustal-scale thrust fault in British Columbia, termed the Monashee décollement (MD; Read and Brown 1981) (Figs. 2-1 and 2-2), which may be responsible for inverted metamorphism (Figs. 2-2 and 2-3) and related heating of the

footwall rocks. These rocks are best exposed in the northern flank of the Monashee complex (Fig. 2-1c), which is a domed metamorphic core complex exposed through a structural window in the southeastern part of the Omineca Belt within the hinterland of the Canadian Cordillera. High-grade deformation and metamorphism within the complex occurred during Late Mesozoic to Paleocene compression and crustal thickening (Brown 1980, Journeay 1986, Brown et al. 1992, McNicoll and Brown 1995). Tertiary extension (Parrish et al. 1988, Carr 1990, Parrish 1995 and references therein) facilitated the exhumation and exposure of some of the deepest structural levels within the Cordillera, preserving excellent evidence of deep-seated thrusting and related thermal processes.

Locally, the focus of this study centres on the Sibley Creek syncline (SCS, Fig. 2-2) (Wheeler 1965, Brown 1980, Journeay 1986, Scammell 1986), which is a recumbent kilometre-scale fold that controls map-scale (1:20 000) geometry of stratigraphic units and is thought to belong to a regional-scale easterly vergent fold system found in the western flank of the complex (Brown 1980). The tectonic implications of this structure and its timing are important to the overall understanding of the deformation history within the complex and the Canadian Cordillera as a whole and are described in more detail in Chapter 3.

Geochronology

Analytical methodology

With the exception of the procedures outlined below, the U-Th-Pb analytical methods for all samples closely followed those applied to U-Pb dating described by Parrish et al. (1987). These methods included Teflon[®] micro-capsules (0.35 ml) for

mineral dissolution (Parrish 1987), multicollector mass spectrometry (MAT261, Geologic Survey of Canada in Ottawa; Roddick et al. 1987), and estimation of U-Pb errors using numerical error propagation (Roddick 1987). Only zircons from DG-118-95 were abraded according to procedures described by Krogh (1982). Mineral selection and U-Th-Pb chemistry were performed at the Geological Survey of Canada (GSC) in Ottawa where U blanks were <1 pg, Pb blanks were 5-10 pg, and Th blanks were estimated at 4 pg. All steps of the U-Th-Pb analyses were performed by the author under the guidance of Dr. R.R. Parrish.

Additional Th-Pb procedures

An additional set of ion exchange columns was added to the procedure to separate and purify Th isotopes. We used Th-Spec Eichrome[®] resin with HCl and HNO₃. For all analyses a mixed spike consisting of ²³⁰Th-²³³U-²³⁵U-²⁰⁵Pb isotopic tracers was used. This spike was prepared by R.R. Parrish at the GSC in Ottawa and carefully calibrated against a freshly prepared gravimetric U-Th-Pb metal solution of known concentration. The ²³³U-²³⁵U isotopic composition of the spike was precisely determined using a three-isotope critical mixture procedure (Hofmann 1971) in order to make U-fractionation corrections for individual analyses; a description of this process is given in Appendix 2. The Th mass spectrometric analysis included the use of double Re filaments, which were loaded using H₃PO₄ combined with 2N HNO₃ and analyzed as the metal ion. Conditions of 2.5-3.0 A for evaporation and 5.0-6.0 A for ionization filaments produced stable and relatively strong Th⁺ beams (100-500 mV) which were measured mainly in faraday cups; the temperature of ionization, as measured using an optical pyrometer, was 1850-2000°C.

Unfortunately, absolute Th fractionation during mass spectrometric ionization could not be determined due to the lack of an independent isotopic standard. However, an assessment of internal variability was attained by repeated measurement of a Th isotopic solution ($^{230}\text{Th}/^{232}\text{Th} \approx 7.0826 \pm 0.0036$ at 1 standard deviation (σ) of 10 measurements); this indicated that the error arising from fractionation variability was of the order of 0.025%/atomic mass unit (a.m.u.) at 1 σ . We also measured simultaneously the three U and two Th isotopes. Under these conditions of mutual ionization of Th and U, the absolute fractionation of U isotopes was determined to be 0.1%/a.m.u., and we have assumed this value to be equal to the absolute Th fractionation in this study. The atomic Th/U ratio of the sample as measured by isotope dilution has been added to Table 1 to allow a direct comparison with the model atomic $^{232}\text{Th}/\text{U}_{\text{total}}$ ($\text{U}_{\text{total}} = ^{238}\text{U} + ^{235}\text{U}$) as calculated from their respective decay constants and stable radiogenic daughter products (i.e., $^{208}\text{Pb}/(^{207}\text{Pb} + ^{206}\text{Pb})$). Discrepancies between the two atomic ratios are ascribed to relative loss of Th or U. This is discussed in more detail below. A spreadsheet program in Excel Version 5.0[®] capable of performing the functions necessary for Th-Pb data reduction (Appendix 3) was created using isotope dilution equations from Faure (1986) and error propagation calculation formulas outlined in Appendix 1. A description of the errors incorporated into the calculations for the final isotopic ratios are described in Appendix 1. Finally, in addition to the traditional U-Pb concordia diagrams (Wetherill 1956), U-Th-Pb ‘concordia’ plots were constructed to allow for the immediate visual comparison of the Pb/Th versus Pb/U ages (Figs. 2-4 and 2-5).

Background of samples

Numerous samples were taken from a variety of lithologies, which included pelitic schists, amphibolite, pegmatite, a pyroclastic horizon, mafic dikes, and quartzite. Of these, six samples were strategically chosen for the following reasons: (1) their key locations at systematically deeper structural levels (Figs. 2-3 and 2-8), (2) their likelihood of yielding peak metamorphic accessory minerals such as monazite and metamorphic zircon, (3) their potential to test previously published ages that remain questionable, and (4) their ability to bracket metamorphic and structural events. U-Th-Pb analyses are shown on three cascading ‘concordia’ diagrams for each of the six samples in Figure 2-4 (a-r), all relevant isotopic data and mineral characteristics are found in Table 1, and sample localities are indicated in Figure 2-2. This section will provide sample descriptions for each analysis, beginning with monazite analyses presented in order of highest to lowest structural level, followed by the zircon analyses. Grains were selected based on their clarity (absence of inclusions), magnetic susceptibility, size, and morphology. For each sample, the vertical distance beneath the extrapolated Monashee décollement surface has been provided in the sample description subheadings and was determined from the following calculation:

$$V_{md} = (D \tan \alpha) \pm d \quad [1]$$

where V_{md} is the vertical separation between the sample location and the extrapolated MD surface overhead, D is the distance between the sample location and MD surficial expression (MD_{se}), α is the apparent dip angle of the MD surface (true dip $\approx 27^\circ$) using

azimuthal direction between the MD_{se} and sample location as dip azimuth, and d is the difference in elevation between the MD_{se} and the sample location. Sample localities have been projected onto a cross section (Fig. 2-3) which intersects approximately orthogonally with the axial surface trace of the SCS. The projection of sample localities assumes a two-dimensional model with very little along-strike variation.

Monazite analyses

Sample DG-105-95, unit 7P, highest structural level, ~510 m below MD¹

Four multigrain monazite analyses using metamorphic equant crystals were carried out on DG-105-95, a Ky-Bt-Ms-Pl-Qtz (mineral symbols used are from Kretz 1983) pelitic schist of unit 7P found within the upper overturned limb of the SCS and closest to the MD (Figs. 2-1c, 2-2, 2-3).

Mapping by the author during this study and by Scammell (1986) suggests that the thickness of this unit has been dramatically attenuated at this locality, probably due to its proximity to the MD (Fig. 2-2). In both hand sample and thin section there is visible a planar fabric that parallels the penetrative foliation found throughout the mapping area. The above mineral assemblage parallels and overgrows this fabric, indicating peak metamorphism was syn- to post-kinematic. DG-105-95 was chosen because it represents the highest structural level closest to the MD of all samples taken from its footwall, and hence its age brackets approximately peak metamorphic and syn- to post-deformation conditions closest to the shear zone and presumed heat source.

Sample DG-136-95, unit 7P, ~600 m below MD

Four monazite analyses were performed on equant single grains from sample DG-136-95, a Ky-Sil-Grt-Bt-Pl-Qtz-bearing pelitic schist also from unit 7P. The thickness of this stratigraphic unit at this location is more than double that of DG-105-95. The fabric found in this sample is not as strongly developed as in DG-105-95, and more of the peak metamorphic minerals grew after the deformation. It appears as though the deformation at this locality was not as pronounced as at DG-105-95, consistent with it being located structurally further beneath the MD (Figs. 2-2 and 2-3).

Sample DG-122-95, unit 11P, ~2200 m below MD

Four multigrain monazite analyses on equant to elongate crystals were conducted on DG-122-95, a Ky-Grt-Bt-Qtz-Pl-bearing semi-pelitic schist from unit 11P, found in the overturned limb of the SCS. Evident in hand sample and thin section is a well developed foliation mainly defined by the preferred orientation of biotite. Most kyanite is aligned parallel to the fabric and displays a significant amount of embayment by quartz and biotite. The quartz crystals appear to be mylonitized because of their small, equant, and aligned (parallel to the main fabric) character, suggesting dynamic recrystallization. The above observations indicate that peak metamorphism in this rock was approximately coeval with deformation.

Sample DG-167-95, unit 7P, lowest structural level, ~3010 m below MD

Four multigrain monazite analyses on relatively equant crystals were carried out on DG-167-95, a Ky-Sil-Bt-Ms-Pl-Qtz-Grt-bearing pelitic schist from unit 7P, located in the lower, upright limb of the SCS. Thin section analyses showed that much of the

¹ Distance below extrapolated surface of the Monashee décollement.

kyanite, sillimanite, and biotite were aligned in the main fabric of the rock, paralleling the regional penetrative foliation. However, some garnets did preserve an earlier fabric defined by the alignment of quartz inclusions, intersecting the main fabric at a high angle. The preservation of the earlier fabric may be attributed to the structural depth at which this sample was found, insulating it from the subsequent penetrative overprint of the deformation recorded in the rocks above it.

Zircon analyses

Sample DG-107-95, unit 9Q, ~1215 m below MD

Four multigrain metamorphic zircon fractions were taken from DG-107-95, a nearly vertical metamorphosed and recrystallized mafic dyke containing evidence of shortened melt veins and a strongly divariant mineral fabric. Most of the zircon grains were small ($<100\ \mu\text{m}$), inclusion-free, euhedral with well formed prismatic crystalline faces, equant and elongate (aspect ratios (a.r.) $\sim 1:1$ to $1:2$), and non-magnetic at 1.80 A. Additionally, because the microscopic analyses suggested no evidence of inheritance or damage due to Pb loss, the grains were not abraded.

Sample DG-118-95, unit 9Q, ~1046 m below MD

Eight single grain zircon analyses were completed on DG-118-95, which came from a felsic pyroclastic horizon of unit 9Q, in the upper, overturned limb of the SCS. In the hope of finding magmatic zircons to constrain the age of deposition, all grains chosen were elongate (a.r. $\sim 1:2$ to $1:4$) square prisms. Most grains were abraded for 9-12 hours,

had a size of $> 100 \mu\text{m}$, and were nonmagnetic at 1.8 A on a 1° side slope.²

Isotopic results

Results are described below and are illustrated in Table 1 and Figure 2-4 (a-r), beginning with the data that appear to be most straightforward. Additionally, the first three samples described below (DG-167-95, DG-136-95, and DG-105-95) are all taken from the same lithologic unit (unit 7P pelitic schist) but at systematically shallower structural levels beneath the MD and across the SCS from its lower to upper limb. All sample localities with regards to geographic and structural placement are provided in Figures 2-2 and 2-3.

DG-167-95 (Fig. 2-4 a-c)

Sample DG-167-95 was taken from the lowest structural level in the field area for the present study. In plot (a) all four analyses form a cluster above ~ 60 Ma on the concordia curve in U-Pb space, suggesting that the duration of monazite crystallization at this level was short-lived. In the $^{208}\text{Pb}/^{232}\text{Th}$ - $^{206}\text{Pb}/^{238}\text{U}$ diagram (plot b) the data remain reversely discordant, whereas fractions in the $^{207}\text{Pb}/^{235}\text{U}$ - $^{208}\text{Pb}/^{232}\text{Th}$ plot (c) agree almost within error, plotting on or immediately below concordia between ~ 59.5 and 60.5 Ma. These plots, considered in conjunction with the significantly younger $^{207}\text{Pb}/^{206}\text{Pb}$ ages (Table 1), strongly suggest that there is a disequilibrium in the ^{238}U - ^{206}Pb decay series which does not significantly affect the other two chronometers. The argument by Schärer (1984) which favors accumulation of excess ^{206}Pb due to an initial disequilibrium of ^{230}Th during monazite crystallization appears to be a valid explanation,

² Using a FrantzTM electro-magnetic separator.

although in the present case the crystallization was metamorphic rather than magmatic. Based on this conclusion, Pb loss is interpreted to be insignificant because the excess accumulation of ^{206}Pb is very rapid due to the relatively short half life of its parent isotope, ^{230}Th . Thus, if Pb loss had occurred in these relatively young rocks, the isotopic composition data would have quickly migrated back towards the concordia curve in an asymptotic path (Parrish 1990), and would likely plot with very little or no reverse discordance. The residual discordance found in the $^{207}\text{Pb}/^{235}\text{U}$ - $^{208}\text{Pb}/^{232}\text{Th}$ plot suggests that other factors still need to be considered.

DG-136-95 (Fig. 2-4 d-f)

This sample is located structurally higher than DG-167-95 and is composed of single grain monazite analyses. The U-Pb concordia diagram (plot d) for this sample displays the analyses spread out from 65.9 ± 0.1 to 77.5 ± 0.3 Ma ($^{207}\text{Pb}/^{235}\text{U}$) along the concordia curve. The range of ~10 Ma in age for this sample is in sharp contrast to the tight grouping of ages observed in DG-167-95, suggesting that this locality experienced a more complex and protracted thermal history. Additionally, the $^{208}\text{Pb}/^{232}\text{Th}$ ages sit both above and below the concordia curve when plotted against the $^{206}\text{Pb}/^{238}\text{U}$ and $^{207}\text{Pb}/^{235}\text{U}$ data, respectively, showing that neither of the U-Pb analyses agree with the Th-Pb chronometry. The two additional plots indicate that there are complicated U-Th systematics not readily apparent when considering only the U-Pb analysis and suggest that the concordant U-Pb data may be fortuitous and misleading. The mechanisms that may explain the ~10 Ma range of ages and conspicuous Pb/Th - Pb/U plots are considered below in the U-Th-Pb systematics section.

DG-105-95 (Fig. 2-4 g-i)

DG-105-95 represents the structurally highest locality, closest to the Monashee décollement. Like DG-136-95, this sample is spread out along the concordia curve in U-Pb space over an approximate range of 11 Ma from 71.4 ± 0.1 to 82.3 ± 0.1 Ma ($^{207}\text{Pb}/^{235}\text{U}$ ages). However, unlike DG-136-95 where all fractions plot both reversely and normally discordant in U-Th-Pb space, only fractions M-3 and M-4 of this sample clearly plot in this manner, whereas M-1 and M-2 fall very near concordia (plots h and i).

DG-122-95 (Fig. 2-4 j-l)

Sample DG-122-95 was taken from an intermediate structural level within the unit 11P pelitic schist. All the fractions for this sample plot in a tighter spread (~ 4 Ma in U-Th-Pb space) than those taken from structurally higher levels (DG-136-95, DG-105-95). It is also worth noting that these fractions all remain to some degree above concordia in U-Pb space suggesting that these monazites retain some or all of the initial accumulation of excess ^{206}Pb . Both of these observations for DG-122-95 suggest that the thermal history at this particular structural level compared to higher levels was not as complex and monazite crystallization was shorter in duration. This will be discussed in more detail below.

DG-107-95 (Fig. 2-4 m-o)

The fractions in this sample consisted of multiple grain zircon analyses taken from a mafic dyke that displays obvious signs of internal deformation (i.e., shortened leucocratic melt veins and a strong mineral fabric) but preserves fairly straight margins. The zircons in this sample are interpreted to be metamorphic. In U-Pb space the data plot

normally discordant in a tight cluster with $^{207}\text{Pb}/^{235}\text{U}$ ages of 58.2 ± 0.9 to 59.2 ± 0.2 Ma, $^{206}\text{Pb}/^{238}\text{U}$ ages of 56.5 ± 0.5 to 57.0 ± 0.2 Ma, and $^{207}\text{Pb}/^{206}\text{Pb}$ ages of 130-160 Ma. DG-107-95 is located at an intermediate structural level and has U-Pb dates that are slightly younger than those produced for DG-122-95, which is calculated to be approximately 985 m structurally below it. The significance of this and the normal discordance will be discussed below.

The $^{208}\text{Pb}/^{232}\text{Th}$ ages produced for this sample have quite large errors which fortuitously overlap concordia when plotted in U-Th-Pb space. Most of the error for Th-Pb analyses on zircon results from the uncertainty introduced by the common Pb correction due to its low radiogenic ^{208}Pb content (total Pb < 6 ppm, Table 1). Accordingly, the age of zircon crystallization is best interpreted using U-Pb data.

DG-118-95 (Fig. 2-4 p-r)

Eight single grain zircon fractions were analyzed from this felsic pyroclastic horizon (1 fraction rejected due to poor mass spectrometry conditions) in the attempt to reproduce the ~388 Ma zircon age documented by Scammell and Parrish (1993) and tentatively interpreted as a magmatic age for a similar horizon found immediately to the south. Unfortunately, all zircons dated were Proterozoic in age and are interpreted to be xenocrystic. Three colinear analyses G, A, and C were regressed (Fig. 2-6) by a modified York program described in Parrish et al. (1987) and yield an upper age intercept of $\sim 1778.7 \pm 2.7$ Ma, interpreted to reflect timing of crystallization and a lower intercept of $\sim 62.1 \pm 6.1$ Ma (MSWD = 0.32), suggesting a younger thermal event causing either Pb loss or metamorphic overgrowth on the Meso-Proterozoic zircons. These three grains could be cogenetic although their colinearity could also be entirely coincidental. In their

study, Scammell and Parrish (1993) also produced a similar array of ages (with the exception of the concordant Devonian zircon) and concluded that a discordia with upper and lower intercept ages of $1772 \pm 5/-4$ Ma and 68 ± 60 Ma, respectively, was the best fit for their data.

U-Th-Pb systematics

Only the U-Th-Pb systematics of the monazite-bearing samples will be considered in this section because the lack of precision achieved for Th-Pb analyses of zircon fractions renders their Pb/Th ages to be of little value. Of the upper level monazite analyses, DG-136-95 will be examined most thoroughly because it consists of single grain fractions unaffected by the interpretation complexity introduced by multigrain analyses (DG-105-95, DG-122-95), whose ages and potential inhomogeneity are averaged together. However, the apparent similarities in the plots of the upper level samples argue that mechanisms affecting DG-136-95 were likely present in varying degree in the other samples. Although the sample for the lowest level (DG-167-95) consisted of multigrain fraction analyses, the tight clustering of data above concordia suggest that if there were past U-Th-Pb disturbances, they were too insignificant to affect the data in U-Th-Pb space. Therefore, the confidence in the interpretation for this sample is thought to be comparable to that of DG-136-95.

Excess ^{206}Pb and relative Th-U mobility

The luxury of being able to perform and compare U-Pb and Th-Pb analyses in the manner discussed above provides an excellent opportunity to examine some interesting and important U-Th-Pb systematics associated with monazite geochemistry. To begin with, the previously noted problem of reverse discordance of monazite data in U-Pb

space caused by excess accumulation of ^{206}Pb (Schärer 1984, Parrish 1990) will be examined. The above description of the U-Th-Pb concordia plots for DG-167-95 combined with the conspicuously low $^{207}\text{Pb}/^{206}\text{Pb}$ ages (Table 1) clearly show that the ^{206}Pb value is inflated, strongly suggesting that there is unsupported ^{206}Pb which does not significantly affect the other two chronometers. As mentioned earlier, the argument by Schärer (1984) which favors accumulation of excess ^{206}Pb due to an initial disequilibrium of ^{230}Th during monazite crystallization appears to be a valid explanation. A variation of the formula for the correction of the $^{206}\text{Pb}/^{238}\text{U}$ age outlined by Schärer (1984) is applied below in the attempt to compensate for the apparently excessive ^{206}Pb value.

Another interesting observation is that U-Th-Pb plots (Fig. 2-4 e and f) for sample DG-136-95 (as well as DG-105 and 122-95) have data falling both above and below concordia. A disturbance such as U loss or Th gain (i.e., U-Th fractionation) following monazite crystallization could move the isotopic composition of the data away from concordia in such a manner. An inspection of the $(\text{Th}/\text{U})_{\text{model}}$ versus $(\text{Th}/\text{U})_{\text{measured}}$ ratios for sample DG-136-95 in Table 1 shows that the measured ratios are consistently 4.0-5.7% higher than the model ratios, which is proportional to the difference between the Pb/Th and related Pb/U ages. This observation supports the idea that a loss/gain of U and/or Th is responsible for the discordance of ages for DG-136-95 in U-Th-Pb space and suggests that these grains experienced a U-Th disturbance not detectable using only U-Pb chronometry. A correction for this apparent U-Th disturbance based on the difference between the model and measured Th/U values is also outlined below.

Correction for ^{206}Pb

Examination of the model and measured Th/U values for DG-167-95 in Table 1

shows a clear discrepancy between the two values, indicating potential U-Th disturbance. However, the cause of this apparent disturbance is not the result of Th-U mobilization but is attributable to the incorporation of excess ^{206}Pb , which biases the determination of the $(\text{Th}/\text{U})_{\text{model}}$ ratio because it is calculated using the measured radiogenic daughter isotopes of Th and U ($^{208}\text{Pb}/^{206}\text{Pb}_{\text{U-derived}}$; the denominator is the total radiogenic Pb derived from ^{238}U and ^{235}U). Because some of the ^{206}Pb is unsupported, the excess ^{206}Pb results in an exaggerated value for the U denominator in the $(\text{Th}/\text{U})_{\text{model}}$ ratio causing this ratio to be smaller than it should be. This problem can be circumvented by recalculating the $(\text{Th}/\text{U})_{\text{model}}$ after making a correction for the excess ^{206}Pb . This can be accomplished by employing a slightly modified version of Schärer's (1984) equation:

$$\Delta^{206}\text{Pb} = (\lambda_{238\text{U}}/\lambda_{230\text{Th}}) (f-1) [1/(e^{\lambda_{238} \times t} - 1)]^{206}\text{Pb}_{\text{measured}} \quad [2]$$

where $\Delta^{206}\text{Pb}$ is the excess ^{206}Pb , $\lambda_{238\text{U}}$ is the ^{238}U decay constant ($1.55125 \times 10^{-10}/\text{a}$), $\lambda_{230\text{Th}}$ is the ^{230}Th decay constant ($9.22 \times 10^{-6}/\text{a}$), f is the Th-U fractionation factor between the mineral and the magma from which it crystallized ($f = (\text{Th}/\text{U})_{\text{mineral}} \div (\text{Th}/\text{U})_{\text{magma}}$, Schärer 1984), t is the age of crystallization (which for this study is taken to be the Pb/Th age), and $^{206}\text{Pb}_{\text{measured}}$ is the actual ^{206}Pb value (nanomoles/gram) determined using mass spectrometry. Schärer (1984) applied his correction to magmatic rocks on the assumption that the whole rock Th/U value approximated that of the magma during crystallization of monazite. In this study, we deal with solid state crystallization in a metamorphic environment, and analogous measurement of the Th/U ratio available to monazite during crystallization is not possible, since it is unknown to what extent U and

Th were already trapped in other mineral phases. Thus, no measurement of the fractionation factor, f , is possible in metamorphic rocks. Instead, we used the following equation to calculate the Th/U of the ‘metamorphic fluid’ which would yield $^{206}\text{Pb}/^{238}\text{U}$ ages equal to the calculated $^{208}\text{Pb}/^{232}\text{Th}$ ages:

$$(\text{Th/U})_{\text{‘metamorphic fluid’}} = \frac{(\text{Th/U})_{\text{measured in monazite}}}{[(1 - e^{\lambda_{238} \times t}) + ^{206}\text{Pb}/^{238}\text{U}]/(\lambda_{238}/\lambda_{230}) + 1} \quad [3]$$

The $(\text{Th/U})_{\text{‘metamorphic fluid’}}$ values calculated (Table 2) are considered reasonable estimates because they are similar to whole rock values from a number of studies carried out in the southern Monashee complex on rocks from similar metamorphic terranes (e.g., 0.5, Carr 1990; 0.6-1.4, Carr 1992). Using equation [2], the excess ^{206}Pb for each fraction was determined (Table 2) and subtracted from their measured ^{206}Pb value, which was used to recalculate the $(\text{Th/U})_{\text{model}}$ ratios of these fractions (Table 2).

Similar calculations were carried out on DG-122-95 because of its obvious reverse discordance in U-Pb space. However, a slight modification was performed to account for the likelihood of a U-Th disturbance because the U-Th-Pb plots for DG-122-95 (Fig. 2-4 j and k) display very similar characteristics to other U-Th-Pb plots belonging to samples which are interpreted to have suffered a U and/or Th disturbance (i.e., DG-105-95, DG-136-95). Also, the $(\text{Th/U})_{\text{model}}$ versus $(\text{Th/U})_{\text{measured}}$ ratios indicate a loss of U for all the samples in DG-122-95. Thus, assuming that the $(\text{Th/U})_{\text{measured}}$ ratio used in the calculation of the $(\text{Th/U})_{\text{‘metamorphic fluid’}}$ was affected to some degree by U mobilization, the $^{207}\text{Pb}/^{235}\text{U}$ age is applied as t in the denominator because it will also have been affected by a U disturbance. In general, this should compensate for the effect

of the disturbance and produce a more accurate $(\text{Th}/\text{U})_{\text{'metamorphic fluid'}}$ value than if the $^{208}\text{Pb}/^{232}\text{Th}$ ages were used which would not reflect this U disturbance. Once the $(\text{Th}/\text{U})_{\text{'metamorphic fluid'}}$ value is confidently determined, the $\Delta^{206}\text{Pb}$ value is calculated using the $^{208}\text{Pb}/^{232}\text{Th}$ ages because it is assumed that essentially no ^{206}Pb has been lost (because the data plot with significant reverse discordance in U-Pb space as alluded to above), and therefore the best approximation of this value is determined using the chronometer least affected by any U-Th-Pb disturbance (i.e., Th-Pb).

Correction for U loss

Above, we interpret samples (especially the upper level samples) displaying discordance on either side of the concordia curve in U-Th-Pb space and having proportionate differences between their model and measured Th/U values and their Pb/U - Pb/Th ages to have suffered some degree of a U and/or Th disturbance. Accepting this, logic dictates that loss of U and/or Th is more probable than addition because the concentration gradient is strongly from crystal to matrix in these samples with very high U and Th concentrations. Also, for monazite, it could be argued that U loss is more probable than Th loss because Th is a major element of monazite and would have higher crystal chemical stability. Accordingly, other studies have shown that in situations such as this, U loss is considered to be the most probable mechanism when considering Th-U systematics due to U's apparent affinity to mobilize more readily than Th. This concept was investigated in a study of high-grade metamorphic rocks by Keppler and Wyllie (1990) in which the role of fluids in the transport and fractionation of U and Th at magmatic temperatures was examined. They concluded that fluids high in CO_2 or HCl

preferentially complexed with U and not Th, which causes a depletion of U relative to Th in granulite-facies rocks. Accordingly, many of the mafic dykes and lithologies examined in this study contain evidence of secondary carbonate precipitation in cracks and joints, suggesting circulation of CO₂- rich fluids which may have preferentially complexed with U. Thus, assuming DG-136-95 has suffered U loss that is directly proportional to the difference between the model and measured Th/U ratios, a correction has been formulated that accounts for the U loss affecting measured U concentration (U_{measured}) which gives U_o , the corrected U concentration:

$$U_o = U_{\text{measured}} \times (\text{Th/U})_{\text{measured}} \div (\text{Th/U})_{\text{model}} \quad [4]$$

The ‘measured’ values come from isotope dilution analyses, and the $(\text{Th/U})_{\text{model}}$ ratio is calculated using the radiogenic Pb products of Th and U. This equation does not provide the actual quantity of U or Th lost, or the timing at which it happened. The model Th/U value calculated from their respective radiogenic daughter Pb isotopes ($^{208}\text{Pb}/^{208}\text{Pb}_{\text{U-derived}}$; the denominator is the total radiogenic Pb derived from ^{238}U and ^{235}U) represents an averaged rate of Pb accumulation. It does, however, provide the most accurate representation of the actual Th/U concentration that would be responsible for the total accumulation of radiogenic Pb throughout the mineral’s history (this is examined in more detail below). Additionally, if there appears to be obvious retention of excess ^{206}Pb (i.e., significant reverse discordance in U-Pb space), corrections for this must be applied first as described above in equation [2].

Once U_o is calculated, the corresponding ^{235}U and ^{238}U concentrations are

determined based on their natural abundances ($^{238}\text{U}/^{235}\text{U} \approx 137.88$). Their respective $^{207}\text{Pb}/^{235}\text{U}$ and $^{206}\text{Pb}/^{238}\text{U}$ ratios and ages are recalculated. The estimation of errors ($E_{\text{corrected}}$) for the corrected ages includes the following uncertainties:

a = the error given for the uncorrected Pb/U ratio (1 σ of mean in percent).

b = the error associated with the $(\text{Th}/\text{U})_{\text{model}}$ ratio. This is thought to be approximately equal to the radiogenic $^{207}\text{Pb}/^{206}\text{Pb}$ error because it is proportional to the measured radiogenic $^{208}\text{Pb}/^{206}\text{Pb}$. The error may be a bit less since the common Pb correction is much lower for ^{208}Pb than ^{207}Pb in Th-rich monazites, but the $^{207}\text{Pb}/^{206}\text{Pb}$ error is considered as an adequate estimate.

c_1, c_2, c_3 = the errors associated with the $(\text{Th}/\text{U})_{\text{measured}}$ ratio, which must include both of the uncertainties associated with the measured U and Th concentrations. Ultimately this comes back to how well the Th concentration in the spike is known and the fractionation of Th isotopes in the mass spectrometer. c_1 = uncertainty of Th concentration in spike (1 σ of mean in percent) = $\sim 0.1\%$, based on reproducibility of 10 repeated measurements of spike against standard solution; c_2 = uncertainty of Th fractionation during the 10 repeated measurements of an isotopic standard (1 σ of mean in percent) = $\sim 0.05\%$, as explained in the Analytical Methodology section above; c_3 = uncertainty associated with the mass spectrometric measurement of the $^{230}\text{Th}/^{232}\text{Th}$ for each analysis.

The resulting calculation for the corrected age errors ($E_{\text{corrected}}$) is approximated as follows:

$$E_{\text{corrected}} (2 \sigma \text{ of mean in percent}) = 2 \sqrt{(a)^2 + (b)^2 + (c_1)^2 + (c_2)^2 + (c_3)^2} \quad [5]$$

The above calculations for the corrected ages and their errors were performed by the author using the Excel Version 5.0[®] spreadsheet program. Once the new data were reduced, the corrected ages and their errors were plotted on U-Pb and U-Th-Pb concordia diagrams (Fig. 2-5 a-l). In a few of the fractions, the (Th/U)_{model} value was greater than the (Th/U)_{measured} value (Table 1), suggesting either U gain or Th loss, but these differences were < 1% and may not be significant. Even so, Th loss has been interpreted as the most probable candidate and the calculations were adjusted accordingly.

Dispersion of data in U-Th-Pb space (Fig. 2-5 a-l)

Once initial corrections for excess ²⁰⁶Pb were performed on DG-167-95 and DG-122-95 in the attempt to produce more accurate (Th/U)_{model} values, and all monazite samples and their fractions were corrected for apparent U loss or Th loss, the data were replotted in U-Th-Pb space (Fig. 2-5 a-l). The following is a summary of these plots with regard to success or failure of the above-mentioned corrections. The enormity of the errors in the zircon analyses basically invalidates the U-Th loss correction, and therefore will not be examined any further. Also, there is only one monazite fraction that apparently suffered very minor Th loss (DG-105-95, M-2). It would appear that when there is post-crystallization U-Th fractionation, U loss is the norm. Hence, from this point on, the correction will be referred to as the U loss correction.

All monazite samples show considerable improvement with respect to their positioning around the concordia curve in U-Th-Pb space. In these samples, almost all

fractions are concordant within error except for M-3 of DG-122-95 (Fig. 2-5 f), which remains reversely discordant and may be attributable to an underestimation of the amount of excess ^{206}Pb to be removed. This is also a multigrain fraction which may partly account for the calculation falling a bit short. Additionally, fractions M-1, M-3, and M-4 of DG-167-95 display noticeable normal discordance in the $^{207}\text{Pb}/^{235}\text{U}$ - $^{208}\text{Pb}/^{232}\text{Th}$ plot (Fig. 2-5c) (this is considered in more detail below). Nevertheless, the data decreased in age approximately proportionally to the percentage of U loss (or Th loss) assigned to each fraction and produced U-Th-Pb ages that are in very good agreement. If you assume the Pb/Th ages to be the best approximation of the timing of crystallization, then the good agreement displayed by the U-Th-Pb plots for the corrected data suggest that the U loss calculation is a legitimate procedure for correcting U and/or Th loss suffered by the analyzed grains. This also indicates the potential hazards of interpreting ages using only U-Pb chronometry. For example, if a U-Pb plot contains nicely concordant data, then these data may be used to constrain the age of an important thermal event; however, if the grains analyzed have suffered a significant amount of U loss, the calculated ages will be older than the age of the event in question.

Residual dispersion of data, DG-167-95

Accepting that the reverse discordance of monazite data in U-Pb space is caused by the accumulation of excess ^{206}Pb from the decay of preferentially integrated ^{230}Th during crystallization, then the positioning of the data in the U-Pb plot for DG-167-95 suggests that the monazite grew in a stable closed-system environment. The data for this sample would not remain at such a degree of reverse discordance in a tight clustering above the concordia curve if complexities such as continuous or episodic high-

temperature Pb loss were significant factors. Parrish (1990) provides adequate descriptions and illustrations regarding these complexities and the probable migratory paths of affected monazite data which clearly differ from the U-Pb plot of DG-167-95. Therefore, we suggest that the monazites grew in a relatively simple closed-system environment that allowed near-complete retention of radiogenic Pb both during and after crystallization..

The slight normal discordance displayed by fractions M-1, M-3, and M-4 in plot c (Fig. 2-5) was a common phenomenon for the corrected monazite data in Schärer (1984). Following the same line of reasoning used in his $^{206}\text{Pb}/^{238}\text{U}$ age correction, Schärer speculates that the normal discordance may be attributable to an initial disequilibrium of ^{231}Pa during crystallization. This isotope is the longest-lived ($\lambda = 3.25 \times 10^4$ years) intermediate daughter nuclide found in the ^{235}U - ^{207}Pb decay chain, suggesting that it has the potential to cause an excess accumulation of ^{207}Pb , which would result in inflated $^{207}\text{Pb}/^{235}\text{U}$ ages. Schärer finds support for this theory in a study of oceanic sediment by Bacon and Rosholt (1982), which suggests Pa and Th have a similar chemical behavior. Consequently, Schärer concludes that the timing of crystallization is best approximated by his corrected $^{206}\text{Pb}/^{238}\text{U}$ ages because the $^{207}\text{Pb}/^{235}\text{U}$ ratios may be exaggerated, causing the data to plot slightly below concordia. However, this interpretation is tenuous because Pa has an unknown oxidation state at magmatic conditions, which could affect its geochemical affinity. The monazites in this analysis come from rocks thought to have been buried at pressures in excess of 6.4-7.1 kbar and heated to 640-679°C (Scammell 1986). In addition, the likelihood that assumptions in Schärer's correction procedure are met has been doubted (Parrish 1990); this is most certainly an improper model for

metamorphic growth of monazite. Suffice it to say that this correction cannot be quantitatively made in metamorphic monazite.

Possible mechanisms affecting DG-136-95, DG-105-95, and DG-122-95

Three scenarios will be considered to explain the dispersion of data found in these samples: (1) high-temperature episodic Pb loss, (2) high-temperature continuous Pb loss immediately after crystallization, and (3) growth of monazite over a protracted period of time in a metamorphic environment.

Scenario 1 involves high-temperature Pb loss at a time, t_2 , following crystallization (t_1), during a second discrete event. Depending on the timing and extent of Pb loss the data will (a) plot on a normally discordant line that fortuitously intersects concordia at a time younger than t_1 , (b) remain reversely discordant, spread out in a line that may or may not inadvertently intersect concordia at a time slightly older than t_2 (figs. 9 and 10, in Parrish 1990), or (c) plot as a combination of the above.

Scenario 2 requires that peak temperatures persisted after monazite crystallization, driving high-temperature Pb diffusion. If all initial excess ^{206}Pb diffused out, the isotopic composition would migrate asymptotically towards and eventually intersect with the concordia curve (in U-Pb space) and continue to migrate down the concordia until full retention of radiogenic Pb were achieved (Fig. 2-7). Conversely, if Pb loss terminated before all initial ^{206}Pb diffused out, then the isotopic composition would migrate towards but remain above the concordia curve. Varying degrees of Pb loss could explain the data for the samples in question, which have fractions on or very near the concordia curve or hanging just above it (DG-136-95, M-3). If Pb loss is accepted as a plausible mechanism, then the dispersion of ages found in these samples

suggests an apparent contrast in the extent of Pb loss for each the fractions analyzed, possibly being related to grain size within a sample and/or in duration of heating between samples. Higher cooling rates, larger grain sizes, and cylindrical geometries will lead to less diffusion (and higher closure temperatures (T_c), Dodson 1973), which in turn result in older isotopic cooling ages. These factors could explain the ages of single grain fractions of DG-136-95. The three larger grains, M-1, M-3, and M-4, are significantly older (~9-10 Ma) than the smallest grain, M-2, and the only cylindrical grain, M-4, produced the oldest age of the lot (Table 1, Figs. 2-4 d-f and 2-5 g-i).

To quantify the effect these differences in size and shape have on the relative spread of ages, the cooling rate must be known. However, no lower temperature accessory minerals such as titanite were analyzed to give us a control on the cooling rate at this location. Therefore, a moderate estimate of $10^\circ\text{C}/\text{Ma}$ for metamorphic terranes (Heaman and Parrish 1991) is used to calculate the difference between the T_c of the largest grain (+300 mm cylindrical, $T_c \geq 710^\circ\text{C}$) and smallest grain (+150 mm spherical, $T_c \geq 670^\circ\text{C}$) in this sample. The difference of $\sim 40^\circ\text{C}$ yields a maximum age difference of ~ 4 Ma, well short of the 10 Ma spread found in this data set. However, other variables not considered in the T_c equation of Dodson (1973) could have an effect on the rate of Pb diffusion and T_c for a given mineral. For instance, lattice-scale disruptions (e.g., dislocations) caused by pre- to syn-tectonic crystallization could act as a conduit system for Pb diffusion. As identified above, there is definite evidence for deformation of peak metamorphic mineral assemblages at this level (and at DG-105 and 122-95), so it is quite likely that the fractions analyzed contain micro-structural defects. The degree to which each mineral was affected and the permeability of the defects could influence the extent

and duration of Pb diffusion. Presently, this cannot be tested but is important to keep in mind and warrants further micro-analyses.

The third scenario considers a protracted duration of monazite growth in a metamorphic environment. The limiting factors in this scenario would either be sufficient elevated temperatures and/or the availability of elements (i.e., phosphate, Th, Ce, La) required for sustained monazite growth. Either of these factors considered in conjunction with other kinetic arguments affecting mineral growth such as size, shape, and impurities could greatly influence the initiation and termination of monazite crystallization, resulting in the observed spread of ages. Additionally, the relative abundance of available ^{230}Th during crystallization could influence the position of monazite data in U-Pb space. If ^{230}Th is readily incorporated during crystal growth then the data should plot reversely discordant, but if there is none present then the data should plot on or near concordia (assuming no other complexities).

Given the current data set, none of these options can be ruled out as possible mechanisms (separately or together). However, the systematic pattern of the data from higher to lower structural levels and the knowledge that there were thermal events affecting the upper part of the footwall at ca. 60 Ma suggest that both continuous Pb loss and protracted growth may be the most acceptable explanation.

Complexities associated with the U loss correction

Ideally the percent difference between the $(\text{Th}/\text{U})_{\text{measured}}$ and the $(\text{Th}/\text{U})_{\text{model}}$ reflects the actual loss of U experienced by the analyzed grain. If the timing of U loss is effectively at $t = 0$ Ma, then the above statement is valid because the $(\text{Th}/\text{U})_{\text{model}}$ is based on the assumption that the ^{208}Pb and ^{206}Pb which decay from ^{232}Th and ^{238}U , respectively,

accumulate through the entire history of the mineral and only in recent times is the Th/U disturbed, thus having little effect on the integrated $^{208}\text{Pb}/^{206}\text{Pb}$. However, if there is a Th-U disturbance at some intermediate point in the history of the grain, then the ratio of accumulation of ^{208}Pb to ^{206}Pb will change, and ultimately, this will affect the $(\text{Th}/\text{U})_{\text{model}}$ value, as is best illustrated by the following example.

A monazite crystallizes at 80.0000 Ma incorporating 3.2000 nmol of ^{232}Th and 1.0000 nmol ^{238}U , yielding a Th/U ratio of 3.2000 (note: to simplify the calculation ^{235}U is not considered; this does not affect the legitimacy of the example). After 20 Ma, $\sim 3.1648 \times 10^{-3}$ nmol ^{208}Pb and $\sim 3.0977 \times 10^{-3}$ nmol ^{206}Pb accumulate from the decay of the ^{232}Th and ^{238}U , respectively. Accordingly, the remaining amount of ^{232}Th and ^{238}U would now be ~ 3.1968 and 0.9969 nmol (i.e., after 20 Ma). If at this time there is a disturbance that causes 50% U loss lowering the ^{238}U value to ~ 0.4985 nmol, then the subsequent accumulation (for 60 Ma) of ^{208}Pb and ^{206}Pb would be $\sim 9.4757 \times 10^{-3}$ and $\sim 4.6178 \times 10^{-3}$ nmol, respectively. The resulting U-Th-Pb measured values for the 80 Ma monazite would be as follows:

Total $^{232}\text{Th} \approx 3.1874$ nmol
 Total $^{238}\text{U} \approx 0.4938$ nmol
 Total $^{208}\text{Pb} \approx 1.2641 \times 10^{-2}$ nmoles
 Total $^{206}\text{Pb} \approx 7.7155 \times 10^{-3}$ nmoles

This would yield a $(\text{Th}/\text{U})_{\text{model}}$ ratio of ~ 5.1587 and a $(\text{Th}/\text{U})_{\text{measured}}$ value of ~ 6.4543 .

The percent difference between the $(\text{Th}/\text{U})_{\text{measured}}$ and the $(\text{Th}/\text{U})_{\text{model}}$ at the present time will be around 25% compared to the 50% U loss suffered at 60 Ma. However, the measured $^{208}\text{Pb}/^{232}\text{Th}$ and $^{206}\text{Pb}/^{238}\text{U}$ values yield ages of 80.0000 Ma and 99.9381 Ma, respectively, resulting in a percent difference of $\sim 25\%$. Applying the U loss correction

described above (equation [4]), the new ^{238}U concentration would be ~ 0.6179 , generating a corrected $^{206}\text{Pb}/^{238}\text{U}$ age of 80.0000 Ma. Therefore, based on this example we have demonstrated that the formula outlined in equation [4] is a valid technique for correcting Pb/U ages affected by U loss. However, the calculation cannot account for the timing or the actual amount of U loss if the disturbance occurred at an intermediate point in the grain's history.

Summary of U-Th-Pb systematics

The importance of Th-Pb chronometry is profound especially in the dating of Th-rich accessory minerals such as monazite because the ^{232}Th - ^{208}Pb decay chain is less susceptible to U-Th-Pb disturbances or disequilibria than both U-Pb decay series. For instance, the ^{206}Pb disturbance commonly affecting monazite analyses may be corrected using the equation set up by Schärer (1984) but only if the mineral crystallized from a magma which evolved under ideal conditions; this is highly improbable in a metamorphic environment. Also, the data in this study suggest that samples with more complex thermal histories not only sustained probable Pb loss, but also indicate varying degrees of U loss not detected by the U-Pb chronometers. Fortunately, the ^{232}Th - ^{208}Pb decay series does not seem to be affected by either of these problems and can be relied upon to yield more accurate ages for minerals (at least for monazite) that grew in less than ideal conditions. Additionally, the Th-Pb analyses when used in conjunction with the U-Pb analyses provides a method to account for and correct the U loss (equations [4]). Even though the correction cannot accurately estimate the timing or the amount of U loss for disturbances occurring intermediate in the grain's history, the excellent agreement between the corrected Pb/U and Pb/Th ages suggests that this is a valid technique to

correct U loss. Also, and just as importantly, the U-Th-Pb analyses and the U loss correction have illustrated the commonality of U disturbances in U-bearing minerals such as monazite and the inherent problems of using U-Pb analyses as the sole chronometer.

Apparent metamorphic age inversion

The monazite data in this study display a distinct trend of ages becoming consistently younger with increasing structural depth below the MD (Figs. 2-3 and 2-8). Additionally, mineral assemblages and thin section analyses indicate that the monazites grew during metamorphism, apparently coeval with the peak assemblage. Therefore, based on these observations it is clear that the rocks in this study record an apparent metamorphic age inversion which is consistent with data produced to the south within the Monashee complex (J.L. Crowley, unpublished data, 1997). This apparent inversion appears to support conclusions made by Parrish (1995) which argue that the Monashee complex records a peak thermal inversion caused by a rapid underthrusting beneath the hot Selkirk allochthon during the Paleocene. However, some older ages in the current data set are inconsistent with the above conclusion. Monazites in sample DG-105-95 (M-3) crystallized at least by 77.7 ± 0.3 Ma, suggesting peak thermal conditions were reached prior to the Paleocene.

Another observation to take note of is the tightening of the age spread for the samples as you progress structurally downwards (Fig. 2-8), with the greatest range in ages closest to the Monashee décollement (DG-105-95, ~10 Ma) compared to those of the deepest level (DG-167-95, ~0.5 Ma). This trend has been noted further south in the complex and is thought to reflect a decreasing duration of peak thermal conditions at

structurally deeper levels (J.L. Crowley, personal communication, 1996). Thus, given the current data set and the interpretations made above, it appears inescapable that rocks sampled closest to the Monashee décollement experienced metamorphic conditions prior to and for a longer period of time than those located deeper in the tectonic pile.

Further complexities in Pb/U age interpretations

The last problem to be addressed is the age discrepancy between the metamorphic zircon ages produced for sample DG-107-95 (Pb/U ages $\approx 59.2 \pm 0.2$ to 56.5 ± 0.5 Ma) and the metamorphic monazite ages of DG-122-95, (Pb/Th ages $\approx 61.8 \pm 0.3$ to 57.6 ± 0.2 Ma). DG-107-95 is a mafic dyke found at a structurally higher level than DG-122-95, yet the metamorphic zircon ages for DG-107-95 are younger than or equal in age to the metamorphic monazites of DG-122-95. This is inconsistent with the downward younging pattern of metamorphic monazite ages (interpreted to be coeval with peak metamorphism) found throughout this study. One explanation could be that the chemical elements necessary for zircon growth in the mafic dyke were not immediately available when monazites began to grow in the pelitic schist layer of DG-122-95. It is possible that at a later time during high-temperature metamorphism at this level, dehydration of certain lithologies hydrated the mafic dyke and facilitated Zr-liberating metamorphic reactions in the dyke. Another and perhaps better explanation is that the actual structural distances of DG-107-95 and DG-122-95 below the extrapolated MD surface (Figs. 2-3 and 2-8b) are less than what are predicted by the geometrical calculation (equation [1]). Equation [1] does not consider moderate shallowing of the MD extrapolated surface as it crests over the top of the Monashee complex. However, previous workers (e.g., Journeay

1986, Scammell 1986) have postulated that there must be some lessening of dip for the MD extrapolated surface as it passes over the hump of the Monashee complex. Figure 2-3 is a cross section through the present study area which incorporates very moderate shallowing of the MD surface as it crests the dome of the Monashee complex. In this cross section the approximate structural distance below the MD thrust surface for both samples is ~1200 m. With this in mind, the ages at both locations are similar with only minor discrepancies and could be regarded as dating the thermal peak.

Possible thermotectonic model

The above observations and interpretations in conjunction with the model proposed by Parrish (1995) suggest that this part of the Monashee complex experienced an inverted thermal regime where rocks closest to the overlying heat source (Selkirk allochthon) were maintained at peak thermal conditions for an extended duration of time. Shortly after the heat front progressed through the tectonic pile to the level of DG-167-95, the heat source dissipated resulting in the quenching of the system and the locking in of metamorphic ages and assemblages. Parrish (1995 and references therein) attributes the quenching of this system to tectonic unloading on oppositely verging Eocene normal faults (Columbia River fault and Okanagan Valley fault, Fig. 2-1c). The rates of heat diffusivity through the tectonic pile and the mechanical role of thermally aided deformation have not been fully considered in this model. However, first order approximations using average crustal conductivities and heat diffusivities predicted by England and Thompson (1984) of ~ 1.5 to $3.0 \text{ W m}^{-1} \text{ K}^{-1}$ and 1.2×10^{-6} to $6.0 \times 10^{-7} \text{ m}^2 \text{ s}^{-1}$, respectively, strongly suggest that there has to be more than just vertical conduction of heat causing the discrepancy in ages (~ 18 -20 Ma) between the highest (DG-105-95) and

lowest (DG-167-95) sample localities. The limited distance between these levels (~1.7~2.5 km) requires heat conductivities and diffusivities to be orders of magnitude lower than the above values. Therefore, considering the above and given the overwhelming evidence for syn-peak metamorphic deformation, the current juxtaposition of ages requires a significant thermomechanical component. These topics are addressed in Chapter 3, which examines the structural data in conjunction with the geochronology presented in this chapter for the purpose of thermotectonic modeling.

Conclusions

- (1) Reverse discordance in U-Pb space for monazite analyses is caused by excess ^{206}Pb .
- (2) The calculation proposed by Schärer (1984), which presents a correction procedure for excess ^{206}Pb , cannot be applied to metamorphic rocks.
- (3) The $^{208}\text{Pb}/^{232}\text{Th}$ chronometer is an essential tool for monazite geochronology; it lacks long-lived intermediate daughter products and related isotopic complexities, and it is the only way to evaluate U or Th loss in minerals and perform the related corrections to calculate ages of crystallization.
- (4) The U correction outlined in equation [4] is valid for correcting Pb/U ratios and ages. Although it cannot determine the actual amount or timing of U loss if that event occurred in the past, it does nevertheless accurately correct for the U loss effect.
- (5) The minor residual discordance of the corrected data in U-Th-Pb space could be caused by an initial disequilibrium of ^{231}Pa in the ^{235}U - ^{207}Pb decay chain; this cannot be clearly demonstrated.
- (6) Within the current study area, burial, heating and growth of metamorphic monazite began in the Late Cretaceous prior to 77.7 ± 0.3 Ma and continued at lower structural

levels to at least 59.5 Ma. Monazite ages produced in this study suggest that there is a systematic inversion of peak metamorphic ages and that the higher level samples grew for a longer duration of time in a more complex thermal regime.

Table 2-1. U-Th-Pb analytical data

Fraction ^a	Weight ^b (mg)	U (ppm)	Pb ^c (ppm)	²⁰⁶ Pb/ ²⁰⁴ Pb ^d	Pb ^c (pg)	²⁰⁶ Pb/ ²³⁸ U ^f	²⁰⁷ Pb/ ²³⁵ U ^f	²⁰⁷ Pb/ ²⁰⁶ Pb ^f	²⁰⁶ Pb ^g / ²³⁸ U ^g	²⁰⁷ Pb ^g / ²³⁵ U ^g	Correlation coefficient	²⁰⁷ Pb ^g / ²⁰⁶ Pb (Ma)	Th (ppm)	²⁰⁸ Pb/ ²⁰⁴ Pb ^d	Th ^h / U ^h (meas.)	Th ⁱ / U ⁱ (model)	²⁰⁸ Pb/ ²³² Th ^f	²⁰⁸ Pb ^g / ²³² Th ^g (Ma)
DG-167-95																		
M1-7.er,+110	0.060	5142	158.5	1851	101	0.00950±0.11	0.06097±0.19	0.04656±0.11	60.9±0.1	60.1±0.2	0.86	26.9±5.2	43197	4998	8.62	8.43	0.002961±0.21	59.8±0.3
M2-7.er,+110	0.050	5941	200.6	1675	107	0.00959±0.15	0.06103±0.23	0.04615±0.13	61.5±0.2	60.2±0.3	0.84	5.4±6.1	56158	5045	9.70	9.41	0.002969±0.23	59.9±0.3
M3-10.er,+100	0.099	4094	129.8	1762	136	0.00945±0.10	0.06059±0.18	0.04650±0.11	60.6±0.1	59.7±0.2	0.84	23.7±5.4	35979	4975	9.01	8.82	0.002946±0.21	59.5±0.2
M4-10.er,+100	0.111	4571	141.3	1564	191	0.00942±0.09	0.06077±0.18	0.04677±0.12	60.5±0.1	59.9±0.1	0.83	37.4±5.7	38862	4281	8.72	8.56	0.002945±0.20	59.4±0.2
DG-136-95																		
M1.s.er,+300	0.030	4876	172.1	882.8	123	0.01167±0.14	0.07621±0.24	0.04736±0.21	74.8±0.2	74.6±0.4	0.53	67.7±0.2	38213	2155	8.04	7.65	0.003529±0.21	71.2±0.3
M2.s.er,+150	0.016	4475	151.1	1263	37	0.01027±0.09	0.06692±0.17	0.04724±0.12	65.9±0.1	65.8±0.2	0.71	61.1±5.8	38984	3460	8.94	8.59	0.003140±0.21	63.4±0.3
M3.s.er,+250	0.019	3883	139.5	1088	51	0.01185±0.08	0.07704±0.20	0.04717±0.16	75.9±0.1	75.4±0.3	0.68	57.7±7.5	30607	2669	8.09	7.68	0.003576±0.21	72.2±0.3
M4.s.lf,+300	0.028	4884	173.1	1171	89	0.01213±0.08	0.07928±0.17	0.04738±0.13	77.8±0.1	77.5±0.3	0.73	68.5±6.0	36627	2722	7.69	7.28	0.003649±0.20	73.6±0.3
DG-105-95																		
M1-10.er,+100	0.035	5577	134.4	4498	32	0.01177±0.08	0.07739±0.10	0.04770±0.06	75.4±0.1	75.7±0.1	0.77	84.5±3.1	22537	5966	4.15	4.14	0.003730±0.20	75.2±0.3
M2-14.er,+100	0.021	6126	156.9	4534	19	0.01115±0.06	0.07287±0.09	0.04740±0.06	71.5±0.1	71.4±0.1	0.75	69.5±3.0	29810	7316	4.99	5.03	0.003573±0.20	72.1±0.3
M3-12.lf,+125	0.027	8084	179.6	7297	24	0.01282±0.07	0.08447±0.09	0.04779±0.04	82.1±0.1	82.3±0.1	0.92	88.8±1.8	25002	7026	3.17	3.00	0.003851±0.20	77.7±0.3
M4-13.lf,+100	0.025	5287	88.5	6560	14	0.01119±0.08	0.07349±0.10	0.04763±0.06	71.7±0.1	72.0±0.1	0.75	80.8±3.1	11879	4528	2.31	2.15	0.003308±0.21	66.8±0.3
DG-122-95																		
M1-10.er,+100	0.032	3430	128.8	3612	18	0.00967±0.06	0.06275±0.10	0.04705±0.07	62.0±0.1	61.8±0.1	0.76	52.0±3.1	37324	12398	11.2	10.7	0.002959±0.20	59.7±0.2
M2-11.er,+100	0.020	5601	186.3	2554	26	0.00943±0.08	0.06084±0.11	0.04680±0.08	60.5±0.1	60.0±0.1	0.67	38.9±3.9	53086	7724	9.72	9.46	0.002918±0.20	58.9±0.2
M3-13.er,+100	0.021	4151	182.3	2507	20	0.00925±0.07	0.05854±0.12	0.04589±0.10	59.4±0.1	57.8±0.1	0.58	-8.3±4.7	577934	11078	14.3	13.8	0.002854±0.20	57.6±0.2
M4-11.er,+125	0.0086	9551	374.8	5067	10	0.00973±0.07	0.06292±0.10	0.04692±0.07	62.4±0.1	62.0±0.1	0.72	45.1±3.4	106130	18287	11.4	11.3	0.003062±0.21	61.8±0.3
DG-118-95																		
A-a.s.el,+100	0.0046	134.7	39.87	847.7	12	0.26473±0.17	3.95928±0.23	0.10847±0.18	1514.0±4.6	1625.9±3.7	0.65	1773.9±6.4	80.50	195.3	0.62	0.65	0.080783±2.00	1570.2±62.8
C-a.s.el,+100	0.0050	362.4	105.4	4000	7.9	0.28112±0.09	4.20509±0.10	0.10849±0.07	1597.0±2.6	1675.0±1.6	0.75	1774.2±2.5	114.4	412.3	0.32	0.32	0.081229±0.99	1578.6±31.2
D-a.s.el,+100	0.0042	433.5	115.8	2714	11	0.26702±0.14	3.96953±0.12	0.10782±0.11	1525.7±3.7	1628.0±2.0	0.67	1762.8±3.8	117.3	187.0	0.28	0.19	0.053048±5.86	1044.8±122.4
E-a.s.el,+100	0.0040	353.0	113.4	2049	12	0.28396±0.10	4.32350±0.12	0.11045±0.08	1611.0±2.9	1697.9±1.9	0.75	1806.9±2.9	221.1	452.6	0.64	0.70	0.089761±0.60	1737.4±20.8
F-a.s.el,+110	0.0118	109.0	32.57	2562	8.4	0.26799±0.06	4.17257±0.09	0.11292±0.05	1530.6±1.7	1668.7±1.4	0.80	1847.0±1.9	58.52	502.7	0.55	0.63	0.088394±0.29	1712.0±10.1
G-a.s.lf,+100	0.0050	391.9	75.97	3423	5.4	0.15206±0.08	2.23594±0.09	0.10665±0.06	912.5±1.3	1192.4±1.2	0.73	1742.9±2.2	249.2	1307	0.65	1.28	0.086301±0.23	1673.1±7.82
H-a.s.lf,+110	0.0065	326.9	58.46	3145	6.8	0.16191±0.06	3.63821±0.08	0.16297±0.05	967.4±1.1	1557.9±1.2	0.81	2486.7±1.5	69.74	414.2	0.22	0.43	0.088673±4.07	1717.2±139.9
DG-107-95																		
I-80.u.eq,+50	0.050	537.9	4.330	1480	10	0.00888±0.20	0.05974±0.32	0.04878±0.27	57.0±0.2	58.9±0.4	0.55	137.0±12.7	9.18	45.9	0.018	0.018	0.002915±13.6	58.8±16.1
J-41.u.eq,+80	0.027	367.7	2.932	779.3	7.1	0.00881±0.43	0.05903±0.82	0.04860±0.75	56.5±0.5	58.2±0.9	0.42	128.6±35.4	6.94	41.2	0.019	0.015	0.002165±38.6	42.9±33.2
K-80.u.el,+60	0.031	757.5	6.046	1767	7.3	0.00882±0.24	0.05964±0.27	0.04905±0.24	56.6±0.3	58.8±0.3	0.56	150.0±11.2	10.95	45.0	0.015	0.013	0.002484±15.6	50.1±15.7
L-39.u.el,+100	0.030	813.0	6.498	1877	7.3	0.00883±0.08	0.06002±0.17	0.04930±0.14	56.7±0.1	59.2±0.2	0.57	162.2±6.7	N/A	N/A	N/A	N/A	N/A	N/A

^aM1-4, monazite fraction # and grains per fraction (monazites unabraded); all other analyses are zircon; s, single grain analyzed; el, euhedral and elongate; eq, euhedral & equant; er, equant and rounded; lf, elongate and rounded. Number refers to size in μm.

^bWeighing error = 0.001 mg.

^cRadiogenic Pb.

^dMeasured ratio, corrected for spike, and Pb fractionation of 0.09% ± 0.03%/AMU.

^eTotal common Pb in analysis corrected for fractionation and spike.

^fCorrected for blank Pb, U, and Th, and common Pb (Stacey-Kramers model Pb composition equivalent to the interpreted age of the individual grains); errors are 1 standard deviation of the mean in percent for ratios and 2 standard deviations of the mean when expressed in Ma.

^gCorrected for blank and common Pb, errors are 2 standard deviations of the mean in Ma.

^hAs measured by isotope dilution; uncertainty is approximately ± 0.5% (2σ)

ⁱAs calculated from radiogenic ²⁰⁸Pb/U derived (206 & 207)Pb such that: Th/U_{model} = P₂₃₂ / P₂₃₈ + P₂₃₅ = $\frac{[D_{208} / (e^{2.28 \times 10^9 t} - 1)]}{[D_{206} / (e^{2.28 \times 10^9 t} - 1)] + [D_{207} / (e^{2.25 \times 10^9 t} - 1)]}$; where P and D are atoms of radiogenic Parent and Daughter respectively and λ is the decay constant.

Table 2-2: Determination of (Th/U) _{metamorphic fluid} ^a = $\frac{(Th/U)_{mineral}}{[(1 - e^{-\lambda_{238} \times t}) + \frac{{}^{206}Pb/{}^{238}U}{(\lambda_{238}/\lambda_{230})}] + 1}$										
Values, Corrected ²⁰⁶ Pb, & Corrected (Th/U) _{model}										
Constants:										
$\lambda_{238} = 1.55125 \times 10^{-10}$ $\lambda_{238}/\lambda_{230} = 1.6825 \times 10^{-5}$										
$\lambda_{230} = 9.22000 \times 10^{-6}$ $1/\lambda_{238} = 6.4464 \times 10^9$										
$\Delta^{206}Pb = (\lambda_{238}/\lambda_{230}) (t-1) [(1/(e^{\lambda_{238} \times t} - 1))] {}^{206}Pb_{measured}^d$ f = $\frac{(Th/U)_{mineral}^a}{(Th/U)_{metamorphic fluid}^b}$										
${}^{206}Pb_{corrected} = {}^{206}Pb_{measured} - \Delta^{206}Pb$										
Analysis	²⁰⁸ Pb/ ²³² Th age (Ma)	²⁰⁶ Pb/ ²³⁸ U measured	Th/U mineral	Th/U metamorphic fluid ^c	f value	²⁰⁶ Pb (nmol/g) measured ^d	$\Delta^{206}Pb$	²⁰⁶ Pb (nmol/g) corrected	Error ^e ± 1 s.d. (%)	(Th/U) _{model} corrected
DG-167-95										
M-1	59.8 ± 0.25	0.00950 ± 0.11	8.617	0.71930713	11.84	203.6795	3.987562	199.6919	0.2388	0.116219
M-2	59.9 ± 0.28	0.00959 ± 0.15	9.696	0.60072826	13.32	237.6913	5.275627	232.4157	0.2768	0.103765
M-3	59.5 ± 0.25	0.00945 ± 0.10	9.014	0.76368914	12.38	161.3695	3.334231	158.0353	0.2281	0.110963
M-4	59.4 ± 0.24	0.00942 ± 0.09	8.721	0.82860495	11.98	179.6744	3.582644	176.0918	0.2181	0.114514
	Average Th/U _{metamorphic fluid} ⁱ = 0.72808237									
DG-122-95 ^f										
M-1	59.7 ± 0.24	0.00967 ± 0.06	11.162	3.35352141	5.31	138.3717	1.076984	137.2947	0.2076	0.092525
M-2	58.9 ± 0.24	0.00943 ± 0.08	9.723	1.74260750	4.62	220.2538	1.462173	218.7916	0.2168	0.105110
M-3	57.6 ± 0.23	0.00925 ± 0.07	14.282	0.91270876	6.79	160.2078	1.738460	158.4693	0.2109	0.071497
M-4	61.8 ± 0.26	0.00973 ± 0.07	11.399	2.40703039	5.42	387.4733	2.990189	384.4831	0.2211	0.088055
	Average Th/U _{metamorphic fluid} ⁱ = 2.10396702									

^a As measured using mass spectrometry and isotope dilution; uncertainty is approximately ± 0.5% (2 s.d.).

^b Representative metamorphic fluid Th/U ratios calculated from average of ideal (Th/U)_{metamorphic fluid} for each fraction of that sample.

^c Ideal (Th/U)_{metamorphic fluid} value determined using ²⁰⁸Pb/²³²Th age (t).

^d As measured by isotope dilution.

^e Generalized error (1 standard error of mean in %) determined using the errors associated with the uncorrected Pb/U ratio and the Pb/Th ratio used to determine the (Th/U)_{metamorphic fluid}. Both are found in Table 1. Formula for error is as follows:

Corrected Pb/U ratio (& ²⁰⁶Pb conc.) error = sqrt [(Pb/U uncorrected error)² + (error associated with Pb/Th ratio used to determine $\Delta^{206}Pb$)²]

^f ²⁰⁷Pb/²³⁵U ages were chosen for calculating the (Th/U)_{metamorphic fluid} ratio for DG-122-95. Reasons for this were explained earlier in the text.

Once the (Th/U)_{metamorphic fluid} is determined, the $\Delta^{206}Pb$ is calculated using of the best approximation of the crystallization age for monazites, which is interpreted to be the ²⁰⁸Pb/²³²Th age.

^a As measured using mass spectrometry and isotope dilution; uncertainty is approximately ± 0.5% (2 s.d.).

^b Representative metamorphic fluid Th/U ratios calculated from average of ideal (Th/U)_{metamorphic fluid} for each fraction of that sample.

^c Ideal (Th/U)_{metamorphic fluid} value determined using $^{208}Pb/^{232}Th$ age (t).

^d As measured by isotope dilution.

^e Generalized error (1 standard error of mean in %) determined using the errors associated with the uncorrected Pb/U ratio and the Pb/Th ratio used to determine the (Th/U)_{metamorphic fluid}. Both are found in Table 1. Formula for error is as follows:

Corrected Pb/U ratio (& ²⁰⁶Pb conc.) error = $\sqrt{[(Pb/U \text{ uncorrected error})^2 + (\text{error associated with Pb/Th ratio used to determine } \Delta^{206}Pb)^2]}$

^f $^{207}Pb/^{235}U$ ages were chosen for calculating the (Th/U)_{metamorphic fluid} ratio for DG-122-95. Reasons for this were explained earlier in the text.

Once the (Th/U)_{metamorphic fluid} is determined, the $\Delta^{206}Pb$ is calculated using of the best approximation of the crystallization age for monazites, which is interpreted to be the $^{208}Pb/^{232}Th$ age.

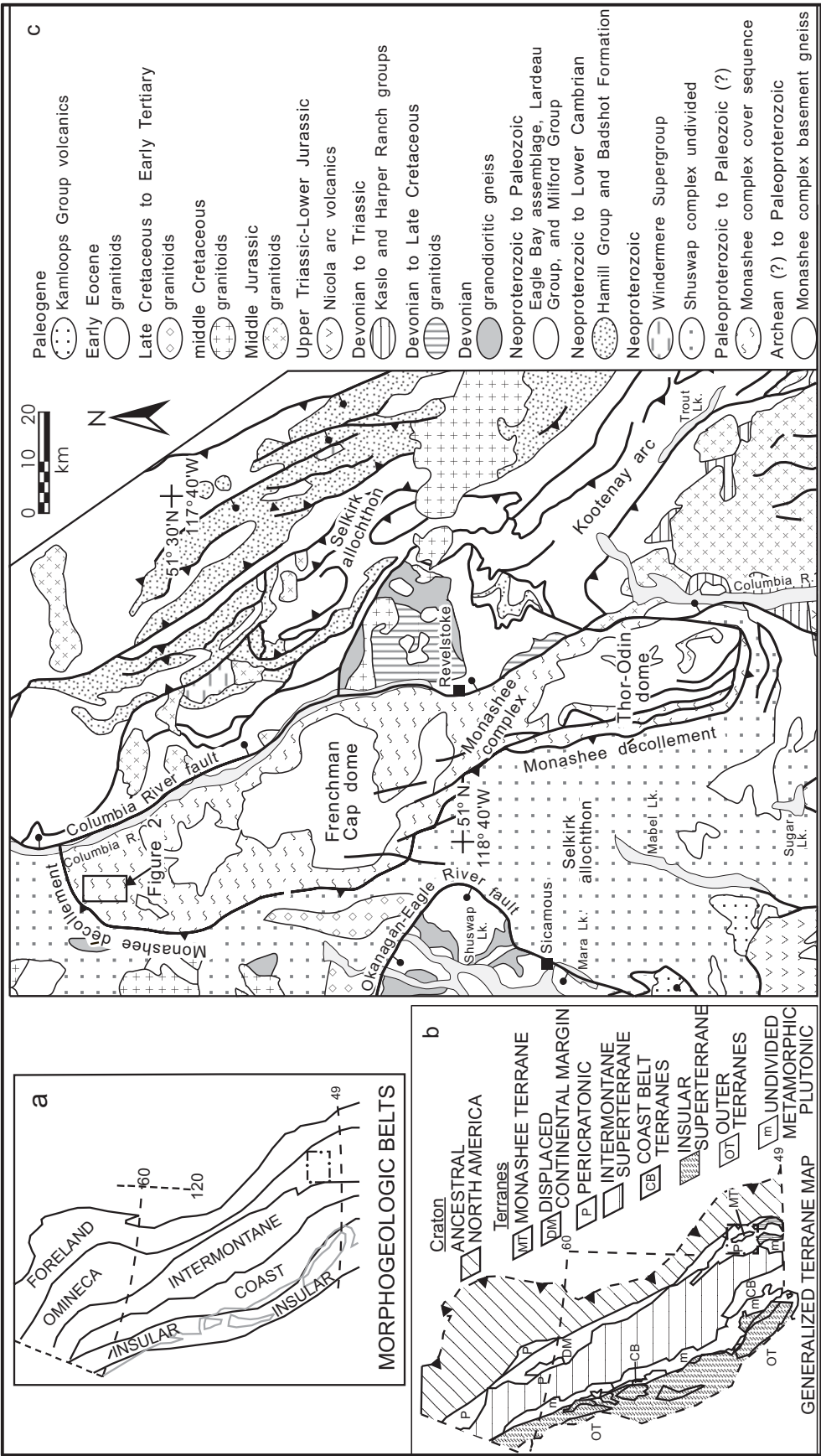


Figure 2-1. (a and b) morphologic belts and terranes of the Canadian Cordillera, modified from Scammell and Brown (1990). Box inset in (a) outlines the map location for (c) within British Columbia and the Omineca Belt. (c) tectonic map of southeastern Omineca Belt, located in the hinterland of the Canadian Cordillera, modified from Scammell and Brown (1990) and Wheeler and McFeely (1991). Included are the major lithologies of the Monashee complex, located within the footwall of the Monashee décollement, and the hanging wall lithologies of the Selkirk allochthon. Where possible the relative timing of lithologies is provided.

Figure 2-2. Lithologic compilation map of northern Frenchman Cap dome incorporating detailed mapping (1:15 000) of Scammell (1986) and the current study. Sample locations (e.g., DG-105-95) for this study's geochronology (both monazite and zircon analyses) are included. A-B indicates cross-section line for this chapter. Contour interval is 100 m.

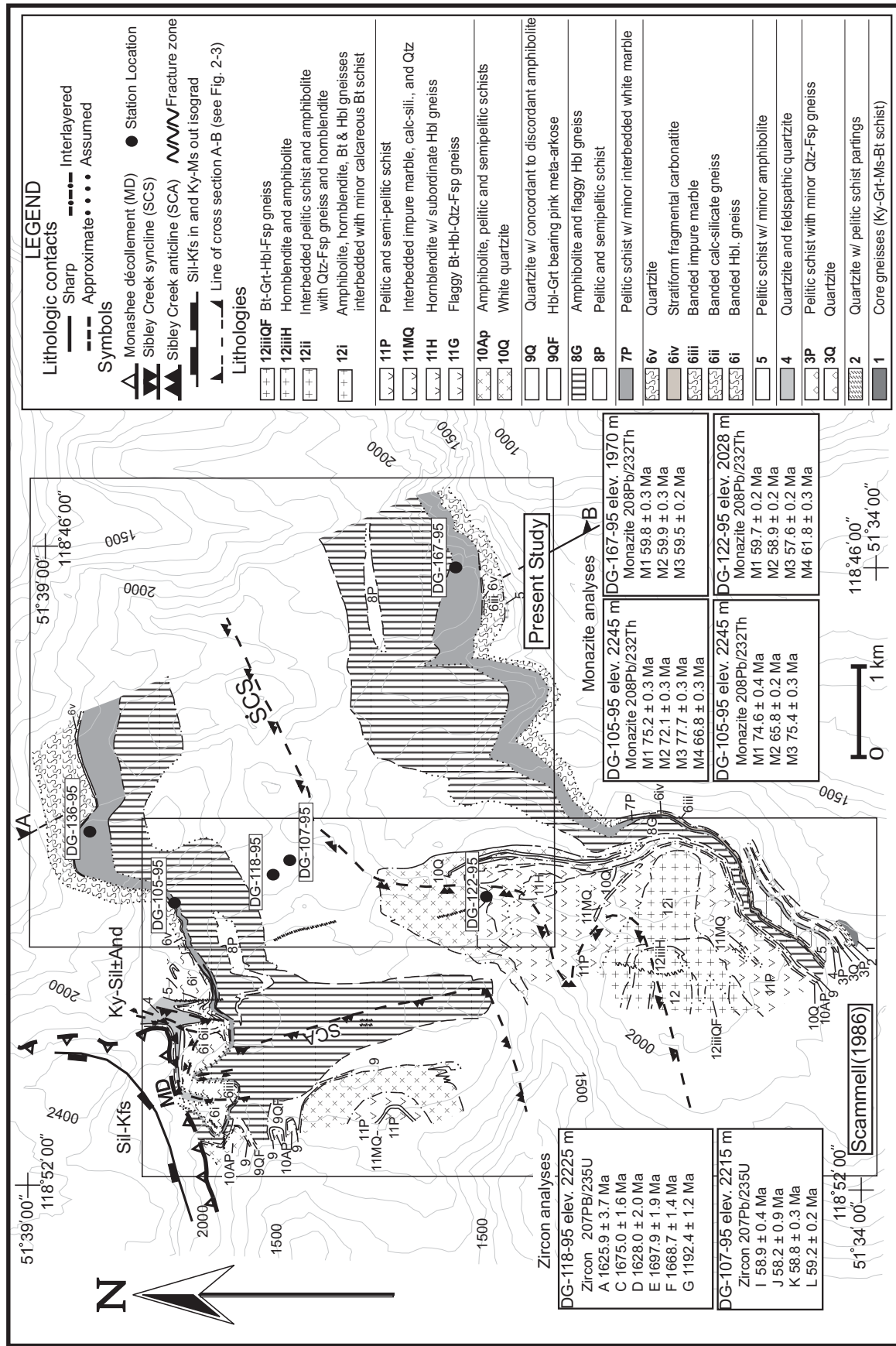
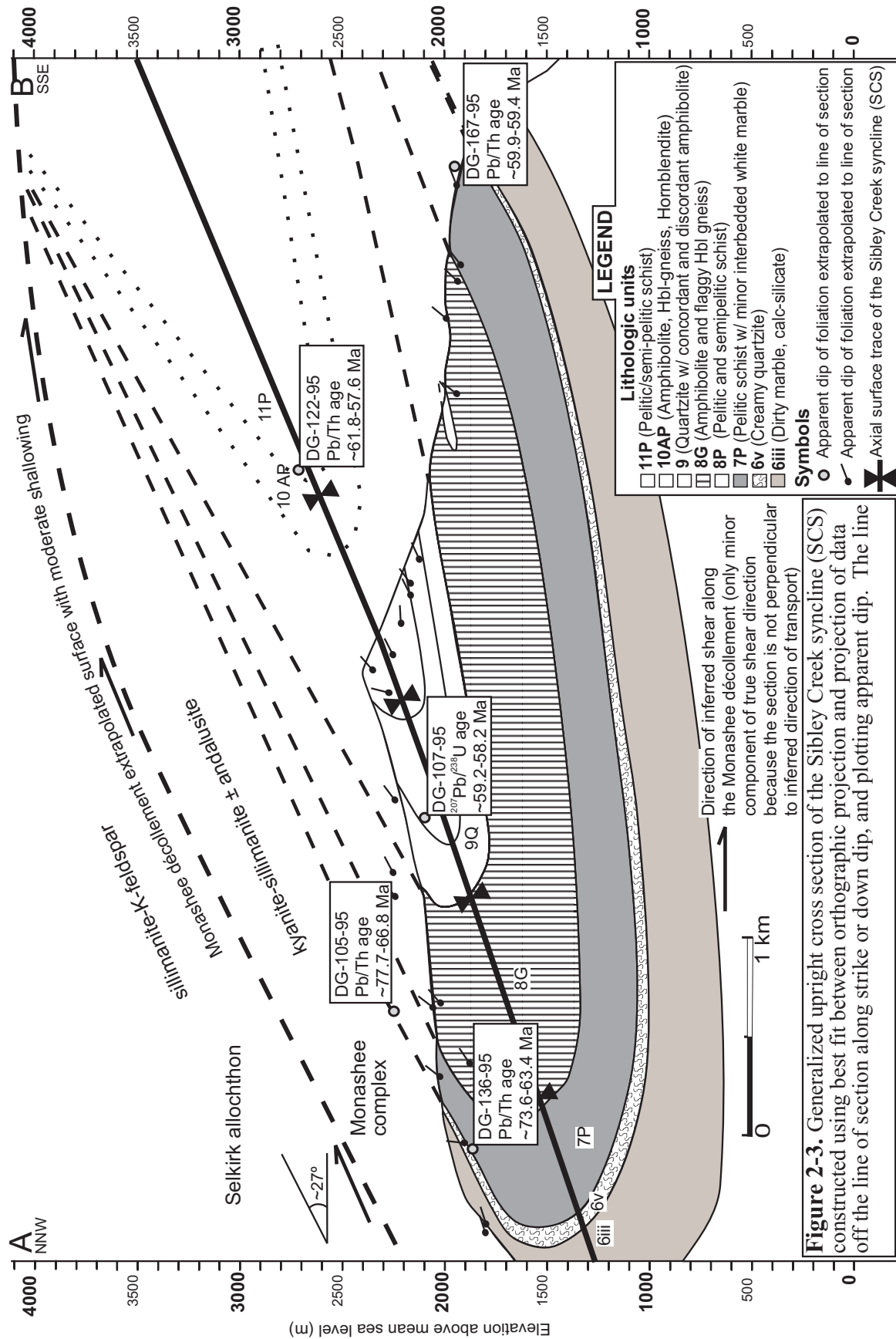
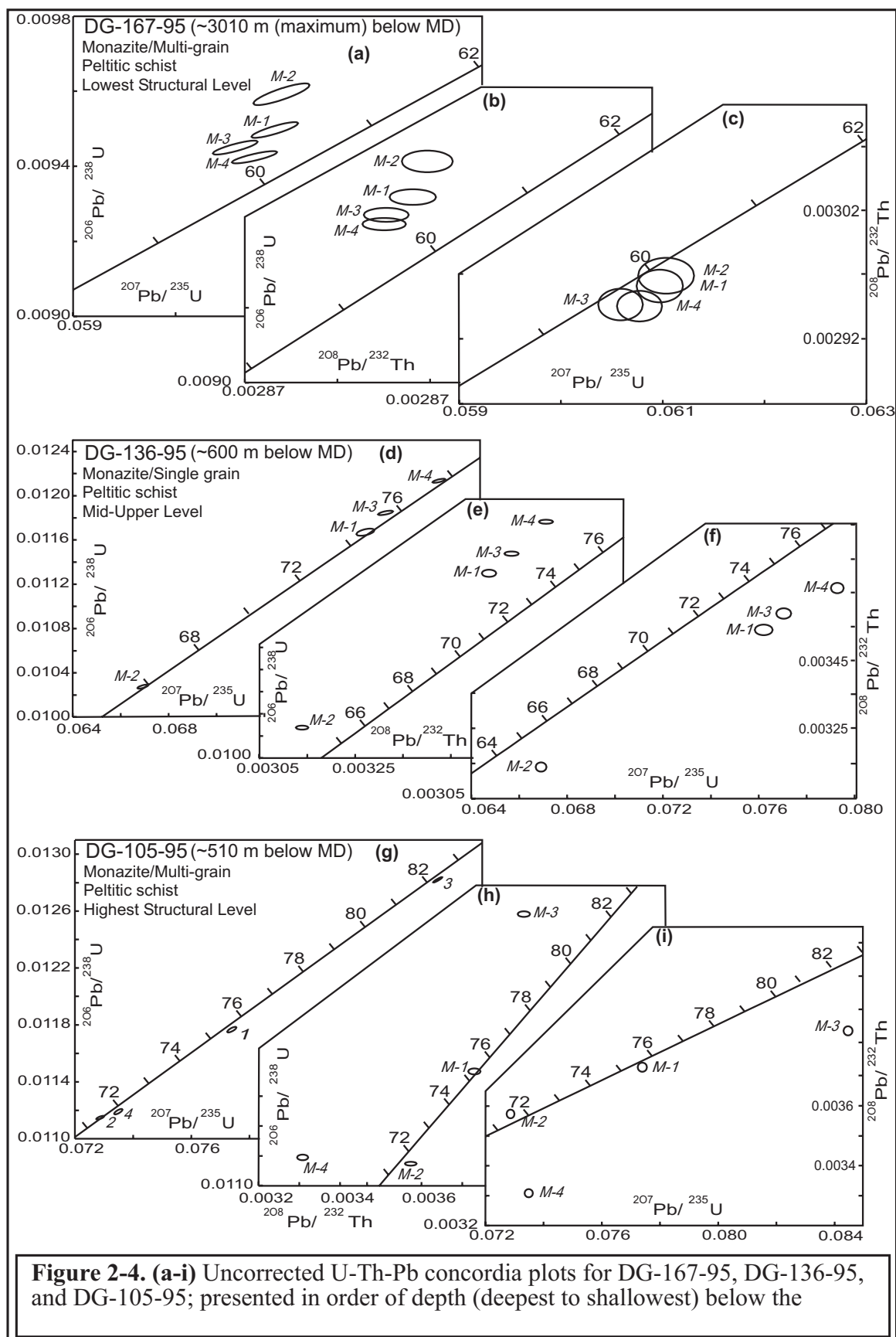
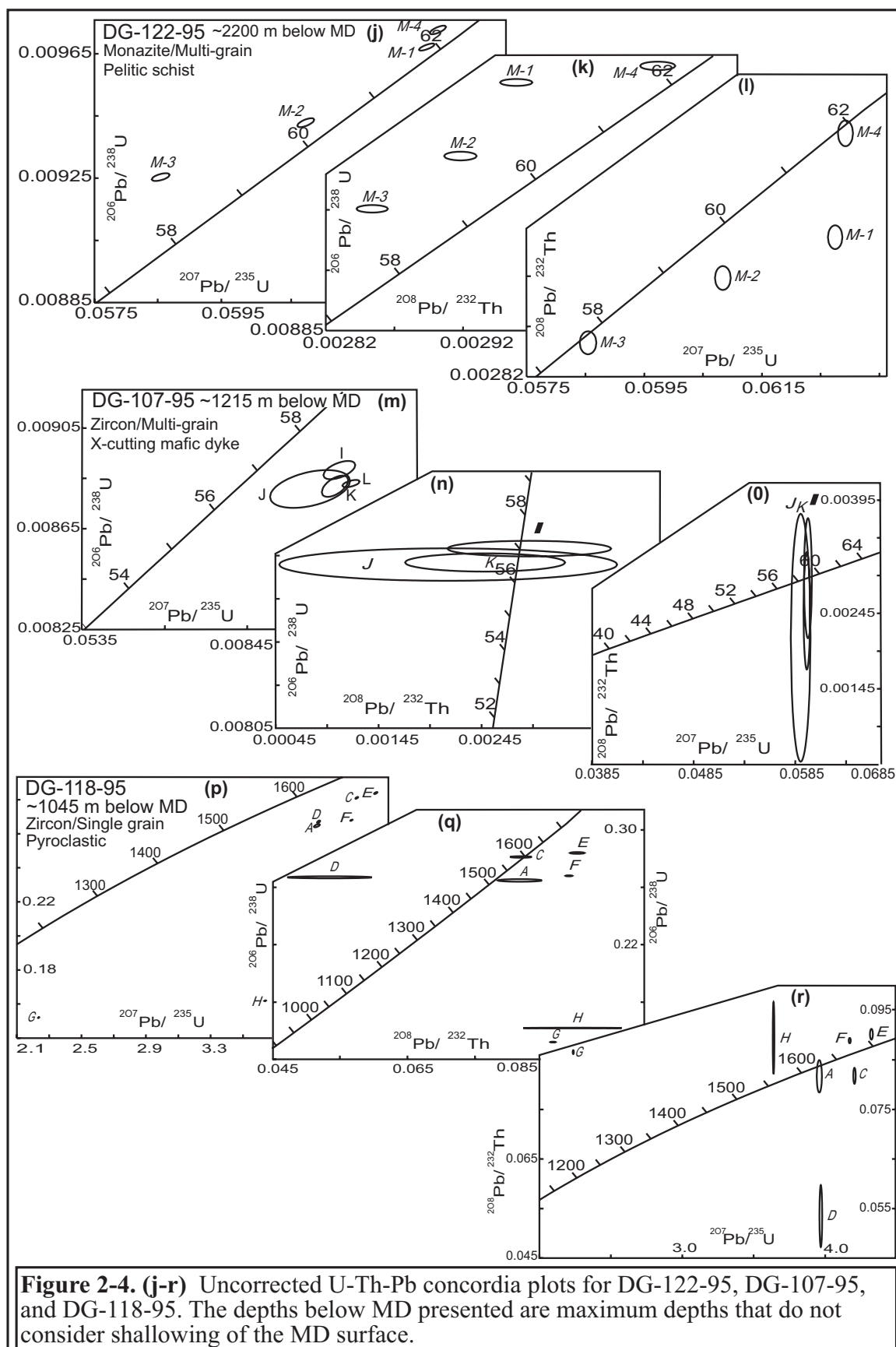
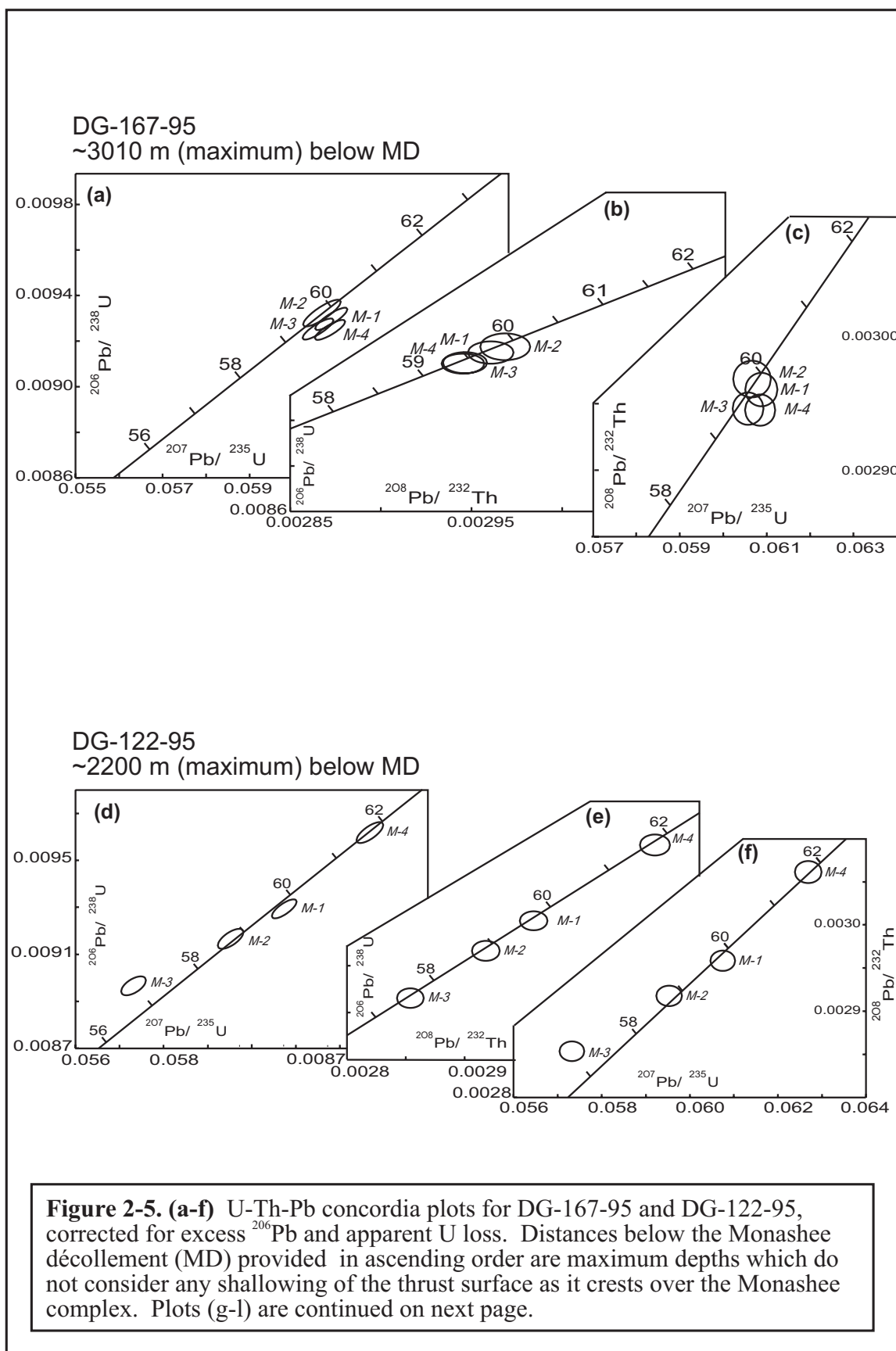


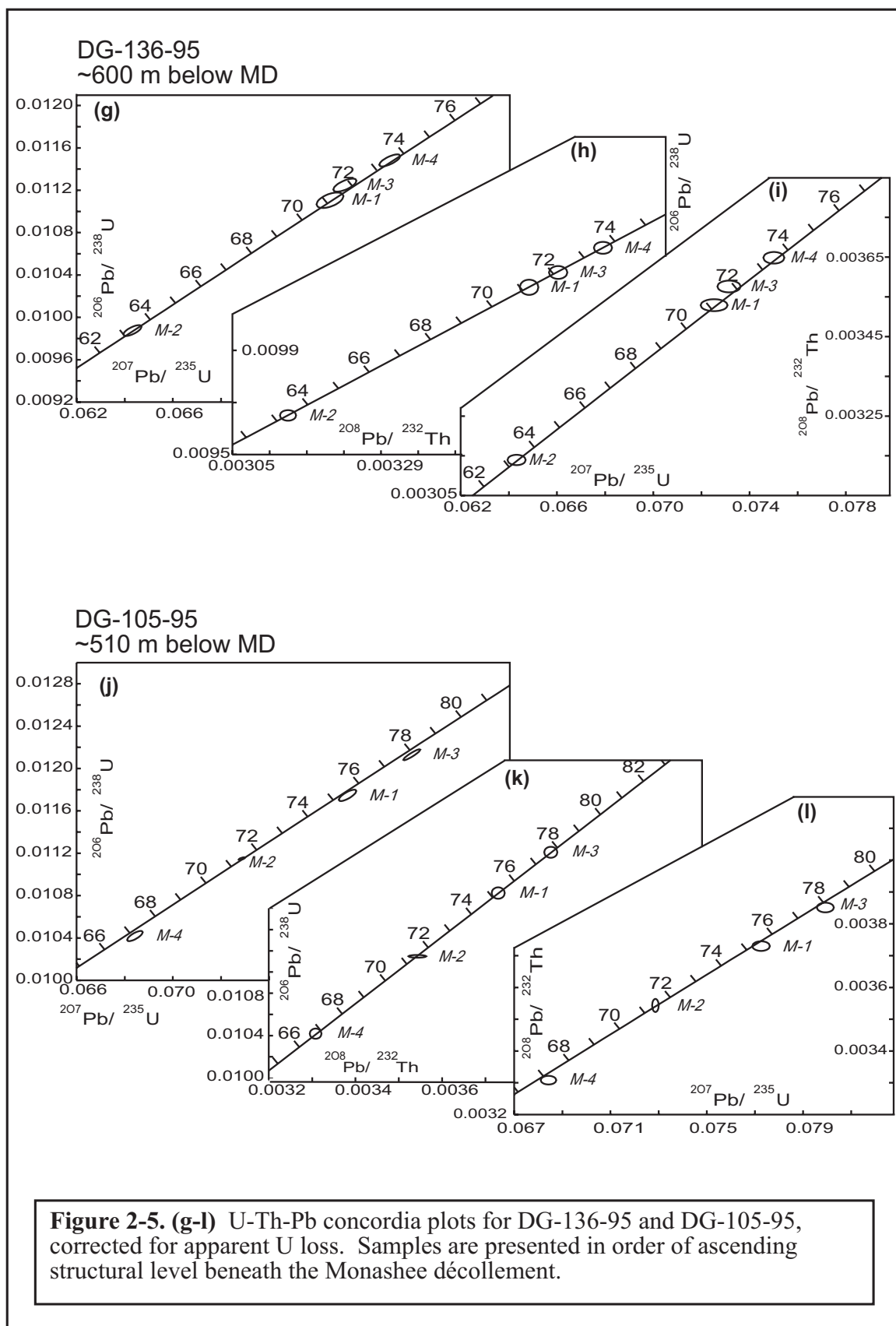
Figure 2-2.











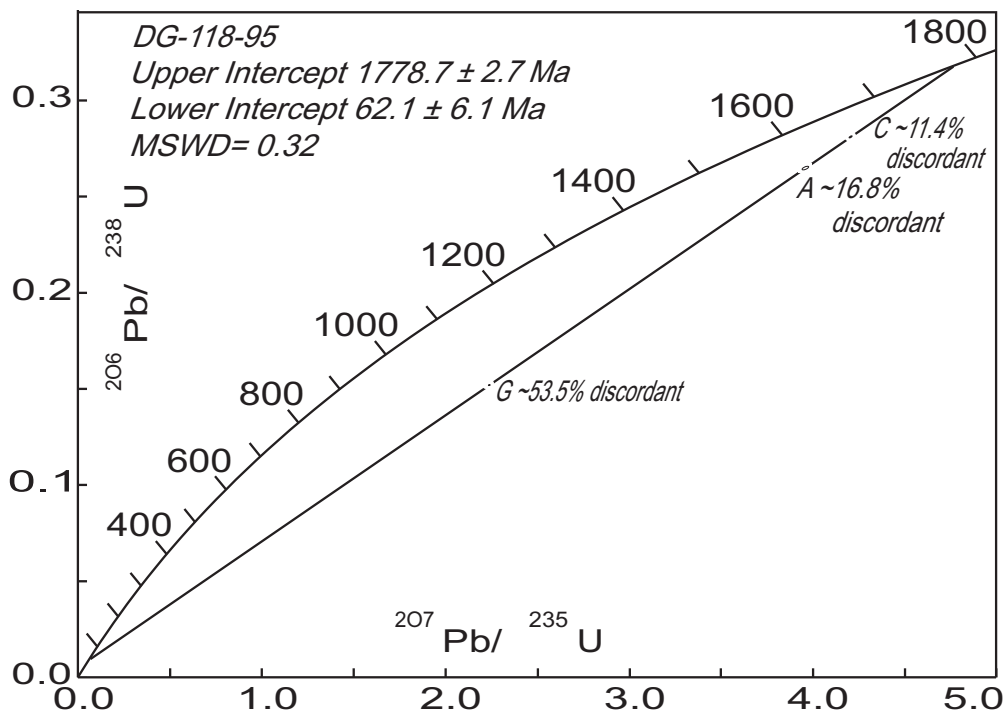


Figure 2-6. Concordia plot displaying the modified York regression discordia line for DG-118-95, through colinear fractions G, A, and C. Upper intercept age of 1778.7 ± 2.7 Ma is interpreted to reflect timing of crystallization. Lower intercept age of 62.1 ± 6.1 Ma suggests a younger

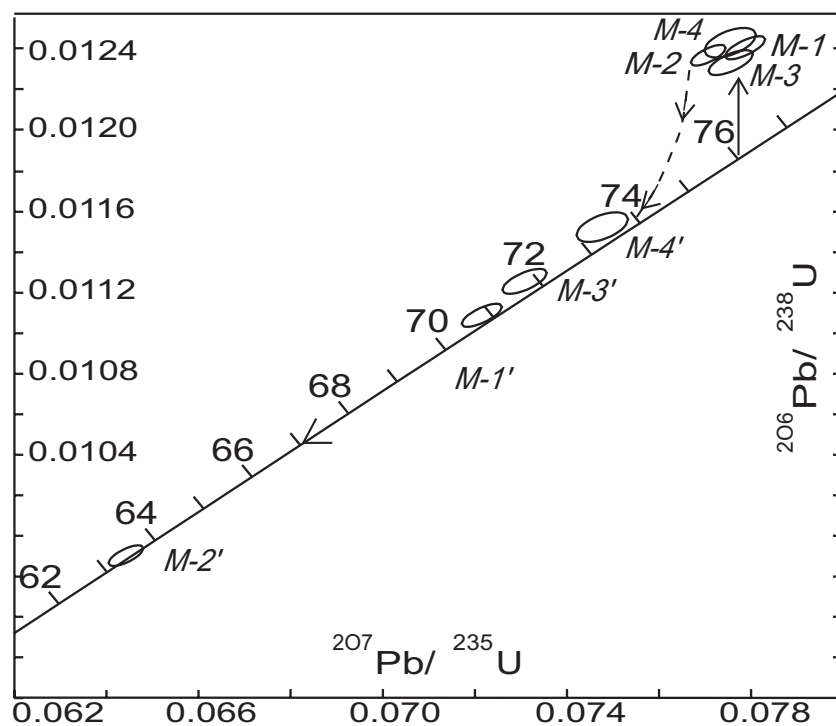


Figure 2-7. U-Pb concordia plot with migratory path of isotopic U-Pb in monazite fractions with time. M-1 through M-4 grew with an initial excess of ^{206}Pb and were affected by post-crystallization continuous Pb loss until full retention was achieved (i.e., M-1'). Factors controlling the amount and duration of Pb loss, which affect the spread of data along the concordia curve are discussed in the text.

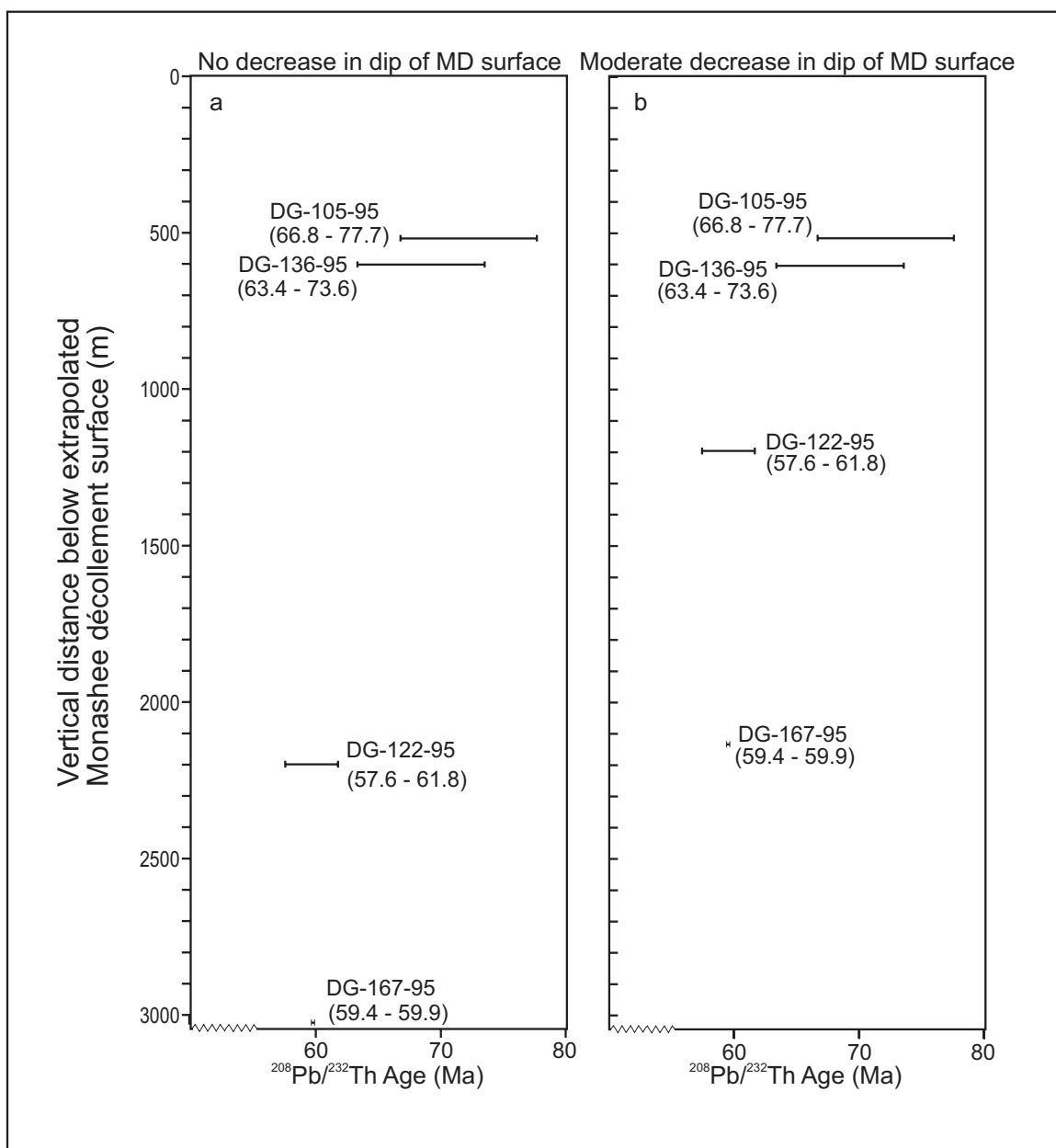


Figure 2-8. Age versus depth (below Monashee décollement, MD) plot illustrating the downward younging and decrease in spread of metamorphic ages within the northern Monashee complex. Plot (a) assumes no decrease in dip of the MD thrust surface, whereas (b) incorporates a moderate decrease.

Chapter 3. Thermotectonic evolution of the Sibley Creek syncline, northern Monashee complex, southeastern Canadian Cordillera

Introduction

Inverted metamorphic isograds are common features in the footwalls of crustal-scale thrust sheets, and understanding the mechanisms responsible for their development is essential for thermotectonic modeling. Some explanations for inversion argue for transmission of heat from above. These include mechanisms such as shear heating along thrust faults (e.g., England and Molnar, 1993) and/or heat transfer to a cool footwall from an overlying hot thrust sheet (e.g., Lefort 1975, Royden 1993, Ruppel and Hodges 1994) causing inversion of thermal gradients with an upward decrease in metamorphic pressures resulting in the inversion of metamorphic gradients (e.g., Hubbard 1989, England and Molnar 1993, Royden 1993). Alternatively, inversion may be the result of mechanical repositioning of metamorphic isograds. This could involve folding of pre-existing isograds (e.g., Tilley 1925, Bhattacharya and Das 1983, Searle et al. 1992), post-metamorphic thrust stacking of isograds from differing structural levels (e.g., Bordet 1961, Treloar et al. 1989), displacement along shear zones (e.g., Jamieson 1986, Brunel and Kienast 1986, Reddy et al. 1993, Hubbard 1996), synmetamorphic ductile shear while preserving structural continuity of the metamorphic sequence (e.g., Grujic et al. 1996), or ductile inversion by progressive shear strain of diachronous isograds (e.g., Jamieson et al. 1996).

Much attention regarding this issue has been focused on the Main Central Thrust zone (MCT) of the Himalayas (e.g., Lefort 1986, Royden 1993, England and Molnar 1993, Ruppel and Hodges 1994, Grujic et al. 1996, Hubbard 1996, Jamieson et al. 1996).

A large quantity of stratigraphic, structural, metamorphic, and chronologic data have been collected, but there remains little agreement concerning the mechanisms responsible for the inversion. Another example of metamorphic inversion is found in the footwall of the Selkirk allochthon in the southern Canadian Cordillera. This footwall is the Monashee complex, which is exposed in a tectonic window through the basal zone of the thrust sheet (Figs. 3-1c, 3-2, and 3-3) (Brown 1980, Read and Brown 1981, Journeay 1986). Journeay (1986) described the inverted isograds in detail and attributed the inversion to heat transfer from the Selkirk allochthon. Parrish (1995) has supported this conclusion, based on analyses of recent geochronologic data. The purpose of this communication is to present new structural and geochronologic data from the Monashee complex that appear to be incompatible with such a heat transfer model. To reconcile these new results with previous data and interpretations, we propose a model that attributes the inversion primarily to diachronous heating due to burial of the footwall, and progressive ductile deformation resulting in the mechanical inversion of isograds. This model does not refute the probability of some degree of downward heat transmission from the allochthon to the complex but does imply that mechanical inversion was the dominant process in this part of the footwall.

Geologic setting

The Monashee complex is exposed through a structural window within the metamorphic hinterland of the southern Canadian Cordillera (Fig. 3-1). It represents an exhumed basement complex of middle crustal rocks interpreted to be an inlier of the North American craton (Armstrong et al. 1991, Parrish 1995 and references therein). The Monashee complex consists of two distinct polydeformed and metamorphosed

assemblages. Coring the complex are Early Proterozoic crystalline orthogneiss and paragneiss rocks of North American cratonic affinity (Armstrong et al. 1991) which are unconformably overlain by the Monashee cover sequence, composed of a 2-3 km thick, laterally extensive assemblage of metasedimentary siliciclastics and carbonates intermixed with metaigneous rocks (Wheeler 1965, Scammell and Brown 1990 and references therein). The cover sequence is thought to have been deposited on a stable coastal platform located on the western margin of paleo-North America that was later affected by synsedimentary rifting and magmatism (Scammell and Brown 1990).

Bounding the Monashee complex to north, west, and south is a crustal-scale northeasterly directed ductile shear zone termed the Monashee décollement (MD) (Read and Brown 1981, Journeay 1986), which is thought to be the westerly continuation of the sole thrust of the Foreland Belt (Fig. 3-1a) (Brown et al. 1992, Cook et al. 1992). The MD separates the basement and cover sequences of the MC from the hanging-wall rocks of the Selkirk allochthon (Figs. 3-1c, 3-2 and 3-3). The eastern limit of the complex is demarcated by the Columbia River fault (CRF) (Figs. 3-1c and 3-2), which is an east-dipping Eocene normal-sense shear zone partly responsible for the tectonic unloading of the complex (Journeay and Brown 1986, Parrish et al. 1988, Carr 1991, Johnson and Brown 1996).

Interpretation of the tectonic history for the complex has evolved substantially over the past decade. It was generally agreed that the complex was buried during crustal thickening associated with the Cordilleran orogeny, but the timing of initial burial at pre-peak metamorphic conditions was uncertain. Brown (1980) first suggested that burial occurred as early as Jurassic time. Journeay (1986) and Brown et al. (1986) modified this idea by proposing a duplex model of crustal thickening of the complex beneath the

Selkirk allochthon. This model implied eastwardly displacement developing in the Jurassic and progressing into the Tertiary. The complex was thought to have been exhumed initially during the late stages of compression, and final exhumation occurred as the result of extension and tectonic denudation in the Eocene (Brown and Journeay 1987). More recently, using structural arguments based on crustal cross sections and palinspastic restorations, Johnson and Brown (1996) suggested that the complex was deeply buried during Cretaceous time followed by partial exhumation during the Late Cretaceous. Final exhumation from middle crustal depths (~12 km) was facilitated by Tertiary extension.

Parrish (1995) reinterpreted the tectonic history of the Monashee complex based on new geochronologic data. He argued that the complex is autochthonous and was not deeply buried until Paleocene time. Parrish proposed that burial of the complex beneath the hot Selkirk allochthon was rapid and was quickly followed by exhumation in the Paleocene to Eocene, which allowed for the inversion and preservation of the present-day metamorphic isograds.

Structural setting of the footwall: northern Monashee complex

The northwest portion of the MC is dominated by a regional-scale isoclinal fold system that includes from south to north the Mount Grace syncline, Kirbyville anticline, and the Sibley Creek syncline whose axial surfaces dip moderately away from the complex toward the northwest and southwest (Brown 1980, Höy and Brown 1980). These folds involve both the basement and cover gneiss sequences of the complex and form kilometre-scale, easterly vergent isoclinal nappes. They are thought to be coeval with the earliest stages of Cordilleran deformation recorded in the complex (Journeay

1986, Scammell 1986) and are therefore important to the overall understanding of its thermotectonic evolution.

This study is focused on the northern flank of the Monashee complex (Figs. 3-1, 3-2 and 3-4) where the Sibley Creek syncline (SCS) and its associated structures are found. Many of the structural elements described herein have been previously documented by Scammell (1986) and are diagrammatically illustrated in Figure 3-5 and Plates 3-1 through 3-7. Ascribing of structures to a “generation” has been based on superposition of one generation upon the other as observed in outcrop and hand-specimen scale. As such, “generations” have geometric and sequential significance, but time correlations (at the regional scale in particular) are not implied. Indeed, data presented here demonstrate that “generations” are diachronous.

The SCS is a second generation structure (D2) which is a pre- to -early metamorphic (Journeay 1986, Scammell 1986) kilometre-scale, overturned and non-planar fold that controls map-scale geometry (Fig. 3-4; Map 2; Plate 3-1). Its axial surface is periclinal and moderately dipping ($\sim 20\text{-}30^\circ$) with a hinge line that plunges shallowly at $\sim 10\text{-}25^\circ$ towards the west-southwest (Scammell 1986). The trend and plunge of the hinge line is based on stereonet calculations using strike and dip measurements of compositional layering in opposing limbs (Scammell 1986, fig. 7), direct measurement of hinge lines in the current study (Fig. 3-6 a-3), and the fact that the axial planar measurements are also shallowly dipping (Fig. 3-6 a-2). Journeay (1986) also measured shallow south-plunging hinge lines for this generation of deformation along the western flank of the complex (The mechanism causing the variation in the orientation of these hinge lines is discussed below). The SCS is well defined by an

established stratigraphy that can be walked around major closures. Stratigraphic facing directions have been determined in this study and by Scammell and Brown (1990) using preserved cross-bedding found in competent quartzites in the hinge zone of the SCS (Plate 3-2).

The SCS has highly attenuated limbs that thicken dramatically towards its core (Fig. 3-4; Map 2). This is especially true for unit 9Q quartzite, which increases from less than 1 m in thickness in the lower limb to greater than 1 km in the core, suggesting that transposition was occurring during the formation of the SCS causing lithologic layering to become subparallel to the axial planes of the SCS. The fact that the trend of the hinge line for the SCS varies between a shallow westerly plunge in the east (Fig. 3-6 a-5) and a southwesterly plunge in the west (Scammell 1986, fig. 7) is likely attributable to the subsequent doming of the complex, bending the SCS around the northwest corner of the dome (Brown 1980). This interpretation is also supported by the change in direction of the axial surface trace of the SCS from east-west in the east to northeast-southwest in the west (Figs. 3-4 and 3-6, Maps 2 and 3) of the field area for this study and that of Scammell (1986).

The SCS and its related macroscopic folds (i.e., Mount Grace syncline, Kirbyville anticline) do not appear on the eastern side of the complex (Psutka 1978, Höy and Brown 1980), thus the development of overturned stratigraphy due to that phase of deformation is restricted to the west flank of the complex. The proximity of these structures to the basal zone of the Selkirk allochthon suggests that their formation is a result of its emplacement.

In the core of the SCS, associated parasitic folds and fabrics are sparse and only clearly identified in the eastern portion of the field area within competent lithologies such

as the unit 9 quartzite (Fig. 3-4). The geometry of the minor folds is close to tight and vary between Class 1C and Class 2 similar folds (Ramsay and Huber 1987) (Fig. 3-5, Plates 3-3 and 3-4). They are usually 1-2 m in scale, symmetric in the hinge zone to strongly asymmetric toward the limbs. Hinges plunge shallowly to the west or west-southwest, and axial planes dip moderately to the north or northwest. In the highly attenuated limbs of the SCS these associated minor structures become completely isoclinal and boudinaged and are rarely preserved.

Folded around the hinges of some of the minor parasitic folds of the SCS is a foliation surface (S_{01}) which is interpreted to be the first observable generation of deformation in this study (D1) (Fig. 3-5, Plate 3-4). These foliation surfaces are defined by the preferred orientation of muscovite-biotite \pm chlorite and appear to pre-date the growth of high-grade metamorphic minerals. The significance of the deformation responsible for the formation of the foliation surfaces is not known, but preservation of sedimentary structures (e.g., cross bedding; Plate 3-2) in the hinge zone of SCS and the other major closures of this generation suggest that any previous deformation was not regionally significant.

Observed in only two locations throughout the field area were folds that are assigned to the third generation of deformation. They are tight to isoclinal with approximately vertical axial planes and shallow west-plunging hinge lines. Outcrop relationships demonstrate that they deform peak metamorphic minerals such as kyanite, biotite, and hornblende. In both locations, these folds are refolded by the subsequent generation of deformation, D4 (Fig. 3-5, Plate 3-5) which is penetrative throughout most of the current field area. The D4 structures overprint earlier generations of deformation at the outcrop scale, but do not have an obvious effect on the larger-scale SCS. The D4

folds vary between northerly and southerly vergent, but do not systematically change vergence across the hinge of the SCS. They are asymmetrical, tight to isoclinal, overturned, reclined, and sometimes disharmonic (Fig. 3-5, Plate 3-6). The axial planes (S4) dip moderately to the west and northwest, paralleling the penetrative foliation found throughout most of the field area (Fig. 3-6; Map 3) and for the most part are parallel to sub-parallel to the compositional layering (Fig. 3-5). Stereonets in Figure 3-6 demonstrate that the hinges of D4 plunge shallowly to the west colinear with the regional mineral lineation defined by stretching of quartz and feldspars and by the alignment of peak minerals such as kyanite, sillimanite, amphibole, and pyroxene (Journey 1986, Scammell 1986). This dominant orientation is approximately parallel to the interpreted direction of transport for the Selkirk allochthon (east-northeast) over the Monashee complex (Journey 1986).

The geometry of these D4 folds indicate that they were products of both passive and flexural flow folding (Scammell 1986), suggesting high temperatures during their formation. This is confirmed by the observations at the outcrop, hand-sample, and thin-section scale which indicate that the peak mineral assemblages both pre-date and overgrew the D4 fabrics. These observations and interpretations agree with those made by Journey (1986) in which he attributes the colinearity between hinge-line orientation of D4 folds (F4) and the regional trend of mineral lineations to high-temperature passive rotation during non-coaxial flow associated with the east-northeast-directed overthrusting of the Selkirk allochthon. In light of the above description, it is quite likely that the SCS and its associated fabrics were significantly modified during generation of D4 structures.

The last generation of deformation (D5) in the study area consists of brittle structures that are dominantly steeply dipping and trend to the north (Plate 3-7). Minor

faults, fractures, and joints overprint all the earlier deformation described above and rarely display displacements of over 5 m. They are likely related to the development of Eocene extensional faults which bound the Shuswap complex (Journey 1986, Parrish et al. 1988, Johnson and Brown 1996). Although most of the D5 features described above appear to be brittle in this part of the complex, Journey (1986) described discrete west-dipping ductile normal sense shear zones along the western flank of Frenchman Cap dome (Fig. 3-1c) that are possibly related to the Eagle River - Okanagon Valley fault (ERF, OVF) system. These structures pre-date younger brittle extension of probable Eocene age and post-date easterly directed mylonitic fabrics related to Late Cretaceous to Paleocene compression.

Summary

The following is a summary of the relationships between the multiple generations of deformation and metamorphism found in the northern Monashee complex:

- (1) The SCS and related D2 structures are pre-to-early metamorphic and fold a pre-existing foliation surface (D1) that contains low-grade micaceous minerals.
- (2) D2 structures and a rare occurrence of synmetamorphic upright folds assigned to D3 are refolded by pervasive syn-peak metamorphic D4 structures.
- (3) D5 structures, which appear to be related to extensional denudation of the complex, include ductile extensional shear zones and brittle normal faults.
- (5) Low-grade metamorphism is thought to have started during D1, before the initiation of D2 deformation (i.e., SCS), and to have attained peak conditions during the generation of D3 and D4 structures. Peak temperatures continued to persist up to the initiation of extensional deformation (D5), but decreased to low-grade conditions during the final

stages of extension.

Timing constraints of deformation and metamorphism

Summary of geochronology

The geochronologic data presented in Chapter 2 are now reviewed and the results are applied to the timing of the deformation fabrics and regional metamorphism.

For this study, $^{208}\text{Pb}/^{232}\text{Th}$ and dual Pb/U chronometry were performed on monazite and zircon from six strategic localities. The $^{208}\text{Pb}/^{232}\text{Th}$ ages are interpreted to be the most accurate approximation of the time of crystallization (Chapter 2). Thus, the ages referred to are those produced using $^{208}\text{Pb}/^{232}\text{Th}$ chronometry. Of particular significance are 16 monazite fractions extracted from four pelitic schist samples containing peak metamorphic mineral assemblages of kyanite \pm andalusite \pm sillimanite, garnet, biotite \pm muscovite, quartz, plagioclase \pm k-feldspar. These samples were taken from systematically deeper structural levels beneath the Monashee décollement (Figs. 3-7 a and b, and 3-8). Additionally, three of the four pelitic samples were taken from the same lithological unit (unit 7P, Fig. 3-4; Map 2) that occurs in both the upper and lower limbs of the SCS. The data produced enable examination of the timing of deformation and metamorphism with increasing depth.

Sample DG-105-95, unit 7P, highest structural level, ~510 m below MD

Sample DG-105-95 was taken from a kyanite-biotite-muscovite-plagioclase-quartz-bearing pelitic schist of unit 7P, found within the upper, overturned limb of the SCS (Fig. 3-4). This sample represents the highest structural level of all the analyses performed in this study and the closest to the MD of all rocks taken from the Monashee

complex. In both hand sample and thin section a conspicuous foliation (fabric) is present, designated S_4 , defined by the preferred alignment of metamorphic minerals such as kyanite and biotite, consistent with deformation and peak metamorphism being coeval at this location.

The $^{208}\text{Pb}/^{232}\text{Th}$ ages for this sample range from 77.7 ± 0.3 to 66.8 ± 0.3 Ma which is interpreted to be equivalent to the age of syn-peak metamorphism and deformation (D4) at this level. The monazite crystals in this sample have evidently persisted during a complex thermal history which involved a sustained duration of elevated temperatures during and after crystallization. Additionally, some loss of U evidently occurred.

Sample DG-136-95, unit 7P, ~600 m below MD

This sample was also taken from unit 7P within the upper, overturned limb of the SCS but at a slightly lower structural level (Figs. 3-4, 3-7, and 3-8). The metamorphic assemblage of DG-105-95 consisted of kyanite-sillimanite-K-feldspar-garnet-biotite-plagioclase-quartz. The metamorphic fabric is not as strongly pronounced at this location.

The $^{208}\text{Pb}/^{232}\text{Th}$ ages approximate those produced for DG-105-95, ranging from 73.6 ± 0.3 to 63.4 ± 0.3 Ma, and are interpreted to reflect the timing of peak metamorphism and deformation (D4). This suggests an environment of prolonged peak thermal conditions during and immediately following crystallization. Like DG-105-95, U loss was interpreted to be significant for all fractions analyzed.

Sample DG-122-95, unit 11P, ~2200 m below MD

DG-122-95, a kyanite-garnet-biotite-quartz-plagioclase-bearing pelitic schist of unit 11P represents an intermediate structural level, located within the overturned limb immediately proximal to the hinge of the SCS (Fig. 3-4). Deformation of the peak metamorphic mineral assemblage is prevalent, with thin sections showing a definite alignment of biotite and kyanite defining the main fabric within the rock interpreted to have formed during S_4 . The quartz grains appear to have been dynamically recrystallized and elongated, suggestive of mylonitization.

The $^{208}\text{Pb}/^{232}\text{Th}$ ages are substantially younger and closely grouped at this locality versus higher structural levels, ranging from 61.8 ± 0.3 to 57.6 ± 0.2 Ma (Fig. 3-7a and 3-8) possibly suggesting a shorter duration of crystallization at a younger time. Additionally, the U loss for the fractions in this sample is interpreted to be minor, indicating a more simple thermal history at this level.

Sample DG-167-95, unit 7P, lowest structural level, ~3010 m below MD

Located within the lower, upright limb of the SCS at the structurally lowest level sampled in this study, DG-167-95 was taken from a kyanite-sillimanite-biotite-muscovite-plagioclase-quartz-garnet-bearing pelitic schist of unit 7P. Thin section analyses showed that most of the kyanite, sillimanite, and biotite are preferentially oriented, defining the main penetrative foliation of this rock which parallels the main westerly to northwesterly dipping penetrative foliation (S_4). However, one garnet crystal does display a preserved fabric defined by an alignment of quartz inclusions at a high angle to the main fabric. It is difficult to establish which generation of deformation this belongs to because of the paucity of preserved pre- S_4 fabrics at all other localities.

The $^{208}\text{Pb}/^{232}\text{Th}$ ages are tightly clustered, ranging from 59.9 ± 0.3 to 59.4 ± 0.2

Ma, significantly younger than the ages produced at the highest structural levels. The data for this sample are interpreted to be indicative of a closed-system environment where crystallization of monazite was of short duration and U loss insignificant, suggesting a much simpler thermal history than those located at higher structural levels (Chapter 2).

Timing of deformation and metamorphism

The timing of D1 can only be qualitatively interpreted as pre-dating the SCS (D2) event. Likewise, the SCS and its minor structures can only be loosely constrained given the lack of data needed to accurately quantify this generation of deformation. However, general timing constraints can be applied which take into account the information presented above and previously published geochronology. The SCS and associated D2 structures can be no older than the youngest dated lithology they deform, which is ~388 Ma for a pyroclastic horizon belonging to unit 10AP (Scammell and Parrish 1993). Additionally, this timing may be further constrained by palinspastically restoring Cordilleran deformation that is considered to have occurred prior to the Late Cretaceous. This restoration suggests that the deformation front was still to the west of the Monashee complex at that time (Brown 1997, work in progress).

To constrain the minimum age limit of the SCS (D2), its relationship to D4 must be considered. At outcrop scale, the peak metamorphic D4 structures penetratively overprint the macroscopic-scale SCS and through thermally aided deformation undoubtedly modified the pre-existing structure of the SCS. Furthermore, it is quite plausible that the generation of D4 structures was part of the continuing high-temperature development of the SCS. Thus, the D4 structures that we observe today at the outcrop-

scale represent a snap shot of the latest stages in the evolution of the SCS. Thus, D2 is interpreted to be pre-D4 and pre- to syn-peak metamorphism, whereas D4 is thought to be syn-D2 and syn-peak metamorphism. Both of these generations of deformation are overprinted by peak mineral assemblages, suggesting that these structures were likely completed prior to the termination of peak conditions and the most recent mineral growth. Accordingly, the minimum age limit for completion of D2 and D4 can only be bracketed by the overprinting ductile and brittle structures of D5. D5 is thought to be related to the extensional denudation of the complex (as discussed earlier), which is interpreted to have initiated at least by 59-58 Ma (Parrish et al. 1988, Parrish 1995). A summary of the above interpretations is provided in the diagrammatic table of Figure 3-5.

Thermotectonic models

Apparent metamorphic age inversion_

The monazite data are interpreted to reflect the timing of peak metamorphism at each locality based on thin section analyses which displayed monazite crystals intergrown with the peak mineral assemblages. Two cross sections have been constructed at an acute angle to each other (Fig. 3-7 a and b), which show the estimated position of the sample localities with respect to the SCS and the extrapolated position of the Monashee décollement overhead. Figure 3-8 is an X-Y plot illustrating the relationship of monazite ages to depth below MD. From these figures it is clear that the timing of peak metamorphism is consistently younger with increasing structural depth. This inversion is consistent with the results of J.L Crowley (unpublished data 1997) produced further south within the Monashee complex where zircon, monazite, titanite, and hornblende ages illustrate a younging of peak thermal conditions at progressively

lower structural levels beneath MD.

Another observed trend is the consistent decrease in the spread of ages for each sample with increasing structural depth (Fig. 3-8) beneath MD, with the greatest range found closest to the décollement (DG-105-95, ~10 Ma) as opposed to the tight clustering found at the deepest level (DG-167-95, ~0.5 Ma). This trend has also been noted by J. L. Crowley (unpublished data 1997), and he interprets this to reflect a decreasing duration of peak thermal conditions at structurally deeper levels. However, within the limits of this study and the data generated, there is not sufficient evidence to corroborate or refute this interpretation. Nevertheless, based on the observations made above one can conclude that monazites from rocks sampled closest to the Monashee décollement experienced a more complex thermal history and grew at an earlier period of time than those located deeper in the tectonic pile.

Rapid Paleocene burial and Eocene denudation (Parrish 1995)

The observations and interpretations made above concerning the apparent inversion of peak metamorphic ages and the decrease in duration of elevated temperatures with depth seem on the surface to be consistent with the model proposed by Parrish (1995). As pointed out earlier, Parrish argues that the Monashee complex was rapidly underthrust beneath the hot Selkirk allochthon during the Paleocene, causing a thermal inversion which resulted in an inverted Barrovian metamorphism. This was followed immediately by rapid exhumation of the complex and the allochthon during an episode of Eocene extension. Parrish bases these conclusions in part on petrographic evidence presented by Journeay (1986) and the abundant geochronologic data produced within and around the complex that suggest a brief thermal peak of 600-700°C at

approximately 60-55 Ma.

Simply put, the complex begins to heat up from the top down resulting in monazite (and peak metamorphic assemblage) growth closest to the heat source (the Selkirk allochthon) where sufficient elevated temperatures are first attained. As the thermal front progresses downward through the footwall, subsequent growth of monazite occurs, post-dating those found at higher levels. Eventually, as the front reaches its deepest levels (i.e., DG-167-95) the onset of Eocene extensional denudation occurs, which in turn allows for the partial exhumation and quenching of the upper level samples while the lower levels are still in an environment hot enough to allow the growth of peak metamorphic minerals. As the rapid exhumation of the tectonic pile continues, deeper level rocks are cooled at shorter and shorter times following their attainment of peak temperatures. These factors together result in the observed inversion of metamorphic ages, decrease in durations of elevated temperatures with depth, and more regionally, the inversion of metamorphic isograds.

Problems with the heat transfer model

The new geochronologic and structural data presented in this study appear to be inconsistent with a model of thermal inversion as presented by Parrish (1995). The monazite Pb/Th ages, which are considered to be the best approximation for the timing of peak metamorphism, are not consistent with rapid burial of the complex initiating in the Paleocene. Monazite belonging to sample DG-105-95 began to crystallize at least by 77.7 ± 0.3 Ma, suggesting that elevated thermal conditions due to substantial tectonic

burial were reached prior to the Paleocene. Additionally, observations and interpretations presented herein suggest that rocks closest to the overlying heat source (Selkirk allochthon) were maintained at peak thermal conditions for at least 10 Ma, doubling the time predicted by Parrish. This prolonged duration of elevated temperatures is difficult to reconcile with model studies by England and Thompson (1984) and Ruppel and Hodges (1994), which indicate that any thermal inversion would have been relaxed in only a few million years. Thus, the duration of elevated temperatures indicated by the data should have allowed for nearly complete thermal relaxation of the isotherms, erasing any evidence of inverted isograds.

Another limitation of the thermal inversion model invoked by Parrish (1995) is that it does not consider the potential role played by deformation processes. It will be demonstrated that without invoking a significant component of mechanical modification, the distribution of ages found in this study is difficult to reconcile. There is at least an 18.3 Ma age difference between the initiation of monazite growth for the highest and lowest structural levels sampled (DG-10-95 and DG-167-95). With initiation of growth assumed to be analogous to the timing of peak metamorphism at these levels and with the structural distance between them calculated at ~1.7-2.5 km (Figs. 3-7 and 3-8), then a thermal inversion model would require an extremely slow rate of conductively driven heat diffusion from the overlying allochthon. A first order approximation of the vertical distance (Z) that would be penetrated in 18.3 Ma (t) by heat conducted from the hot overthrust Selkirk allochthon has been calculated using the following equation modified from Hargraves (1981):

$$Z = \sqrt{\kappa \times t} \quad [6]$$

Where κ is thermal diffusivity in continental crust which is estimated to be between $\sim 1.2 \times 10^{-6} \text{ m}^2 \text{ s}^{-1}$ to $6.0 \times 10^{-7} \text{ m}^2 \text{ s}^{-1}$ (England and Thompson 1984), assuming a constant heat source of $2.5 \times 10^6 \text{ J K}^{-1} \text{ m}^{-3}$ and average crustal conductivities of $1.5 \text{ W m}^{-1} \text{ K}^{-1}$ to $3.0 \text{ W m}^{-1} \text{ K}^{-1}$. As a result, a vertical separation of ~ 18.6 - 26.3 km between the highest and lowest sample localities is required, equal to at least ten times the actual calculated distance. Conversely, if it had taken 18.3 Ma for the heat to penetrate the restricted vertical distance of ~ 1.7 - 2.5 km , an inexplicably low heat diffusivity value of approximately $5.0 \times 10^{-9} \text{ m}^2 \text{ s}^{-1}$ would be required.

Coupled thermomechanical model

To overcome the apparent difficulties of applying a simple thermal inversion model, a coupled thermomechanical model is proposed (Fig. 3-9) using lines of reasoning similar to those put forward by Jamieson et al. (1996). In this model substantial easterly directed shear strain and attendant attenuation in the footwall led to the apparent preservation of inverted diachronous metamorphism.

Thermochronologic and structural data presented above suggest the SCS was initiated in pre-peak metamorphic conditions and was modified by diachronous and penetrative syn-peak metamorphic deformation. In the earliest stages of Cordilleran deformation within the western limit of the Monashee complex, the SCS is presumed to have evolved significantly west of its present-day position in a cool environment as a buckle fold (Fig. 3-9b). With time, progressive burial (maximum thickness ~ 20 - 25 km ;

Fig. 3-9 a-2) and heating contribute to an increase in the mean ductility of the rocks being deformed, leading to an overall decrease in their ductility contrast and thus a change in fold mechanism from buckling to passive flow. During this flow, hot rocks at deeper structural levels would be translated eastward relative to the underlying rocks, resulting in the present fold geometry (Fig. 3-9). During this time (~78-59 Ma) the deformation front is presumed to be located a significant distance to the east (~ 94-237 km) where the tectonic pile is of minimal thickness with little or no heat production. This distance can be determined using a simple geometric calculation:

$$D = v / \tan \beta \quad [7]$$

where D is the distance (east) to the leading edge of the tectonic wedge (or front), v is the maximum vertical thickness (~20-25 km) above the SCS, and β is the angle of critical taper (Suppe 1981) of the tectonic wedge with the horizontal (~6-12°, based on reconstruction by Johnson and Brown 1996).

Figure 3-9 diagrammatically illustrates that during the onset of Cordilleran deformation (ca. 100-77 Ma, Brown 1997 work in progress), the western flank of the Monashee complex began to deform in a break thrust fashion (Willis 1893). Stratigraphy is folded in an anticline-syncline geometry proximal to the surficial expression of the progressing thrust front. In time, the connecting limbs of the anticline-syncline pair are sheared, overthrusting the hanging-wall anticline and preserving a footwall syncline. As overthrusting progresses there is an increase in the mean ductility of lithologies due to the heat provided by tectonic burial to ~20-25 km and to a lesser extent from the hot

allochthon. This leads to a reduced contrast in ductility of the lithologies which allows the SCS to approximate a passive flow fold. Figure 3-9b demonstrates how rocks presently found in the overturned limb of the SCS (A') may have been translated eastward up to 11 km from their original position (A) along passive flow lines at a rate of approximately 0.6 mm/a for ~18 Ma. Conversely, rocks located in the lower limb (B') traveled significantly smaller distances (~1.5 km) for a lesser amount of time (possibly 0.5 to 1 Ma). At approximately 59 Ma the tectonic pile rapidly denudes via erosion, doming, and extensional unloading beneath the Columbia River and Okanagan Valley faults (Parrish et al. 1988, Johnson and Brown 1996), quenching the heat and preserving the present configuration of inverted peak metamorphic ages found in the footwall.

Summary of current thermotectonic model

This model incorporates a coupled thermomechanical effect with a clear role for shear strain and a probable but less important role for heat transfer from the advancing allochthon. The systematic nature of the change in ages also argues against local heating due to transmission of fluids in which you would expect a more random distribution of ages with depth. As a result the diachronous and upward increase in peak metamorphic ages within the footwall across the SCS is accomplished via mechanical juxtaposition while requiring no downward transmission of heat from the overlying allochthon. Although it is recognized that some downward heat transmission is to be expected, it appears that in this part of the MC the diachronous distribution of peak metamorphic assemblages is largely a result of syn-metamorphic progressive deformation. Accordingly, applying this model to the more regional scale of the MC would require a significant component of thermally aided deformation and rapid exhumation as opposed

to heat transfer from above to satisfy the present distribution of inverted metamorphic ages and isograds (Figs. 3-2, 3-3, 3-7a, and 3-8).

Conclusions

- (1) Structural evidence suggests that the Sibley Creek syncline deforms a pre-existing foliation surface. Therefore, the Sibley Creek syncline post-dates the earliest generation of deformation affecting the cover sequence stratigraphy of the Monashee complex.
- (2) There are at least five discernible generations of deformation found in the Sibley Creek syncline area. These generations are local markers of progressive deformation, but each generation evolves diachronously as a function of structural depth beneath the Selkirk allochthon.
- (3) Major tectonic loading of the complex occurred at least by 77.7 Ma and continued until approximately 59 Ma when it was rapidly denuded.
- (4) An analysis of the structure and geochronology of the area indicates that the pattern of dates relative to the overlying allochthon is consistent with distributed ductile deformation of isograd surfaces by substantial east-directed shear strain and attendant attenuation in the footwall, leading to relative lateral transfer of rocks preserving evidence of inverted diachronous metamorphism. Previous tectonic models that attribute the distribution of diachronous and inverted peak metamorphic assemblages solely to conductive heating from a hot overthrust heat source are rejected.

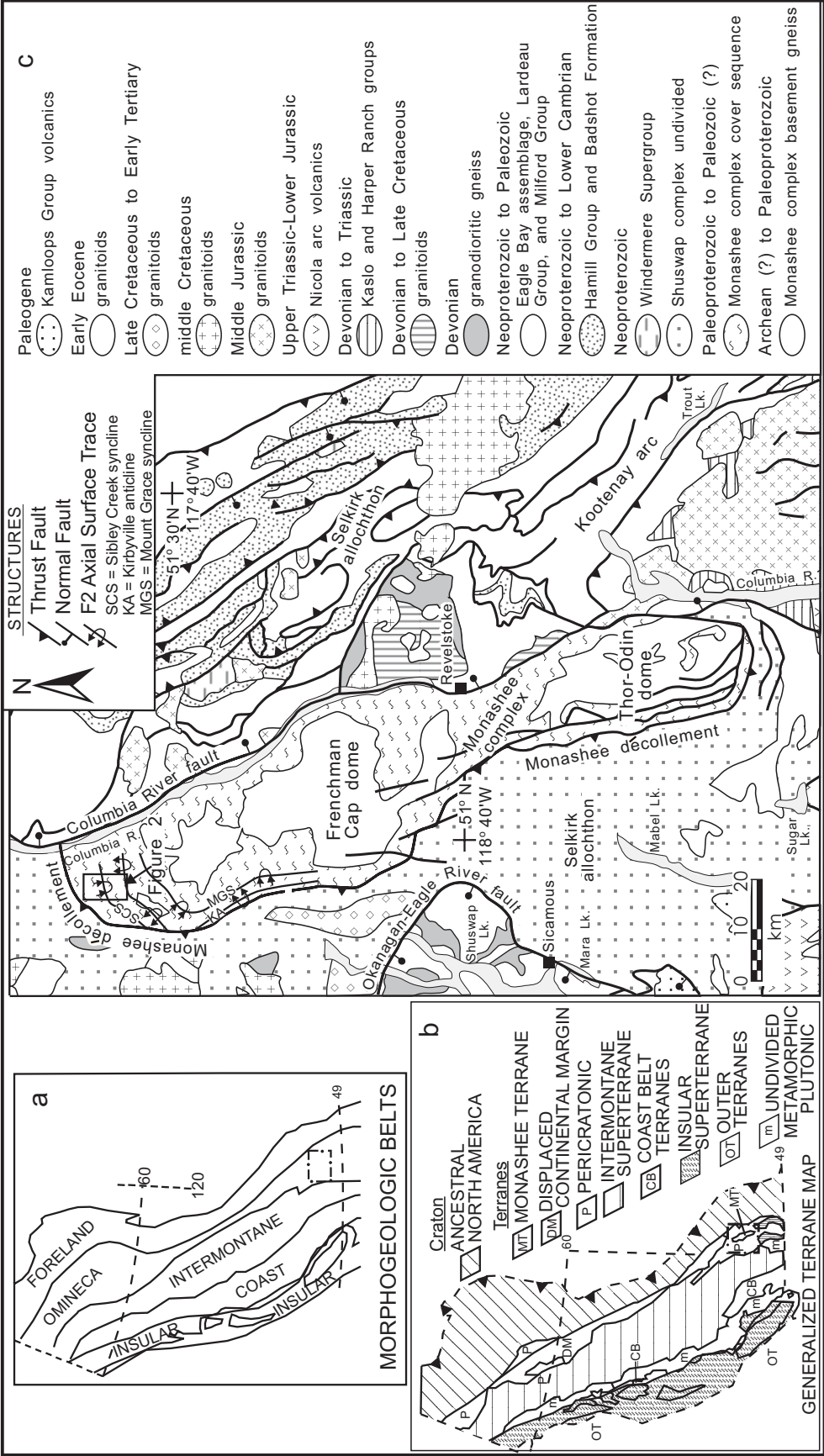
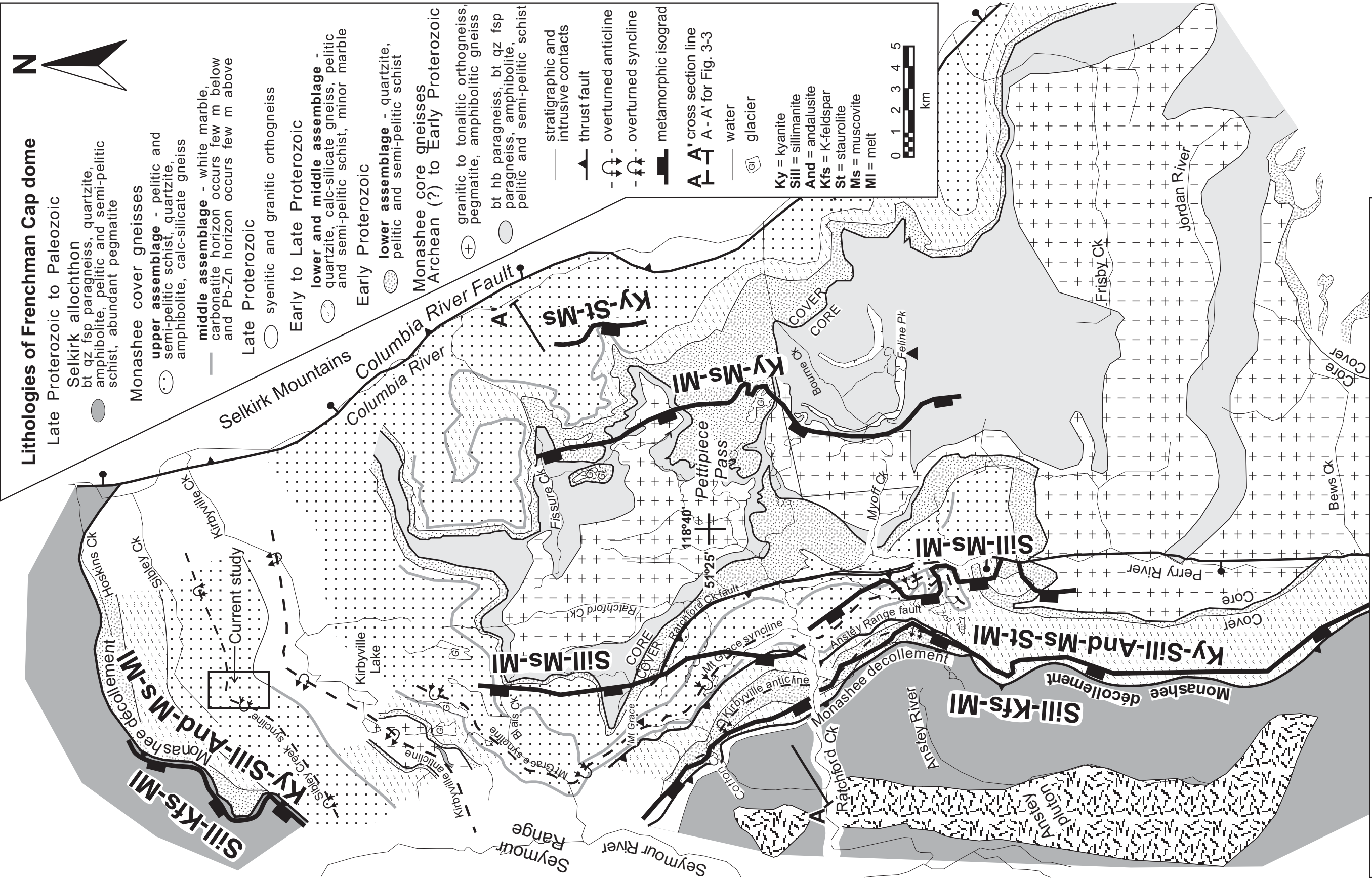


Figure 3-1. (a & b) morphologic belts and terranes of the Canadian Cordillera, modified from Scammell and Brown (1990). Box inset in (a) outlines the map location for (c) within British Columbia and the Omineca Belt. (c) tectonic map of southeastern Omineca belt, located in the hinterland of the Canadian Cordillera, modified from Scammell and Brown (1990) and Wheeler and McFeely (1991). Included are the major lithologies of the Monashee complex, located within the footwall of the Monashee décollement, and the hanging wall lithologies of the Selkirk allochthon. Where possible the relative timing of lithologies are provided.



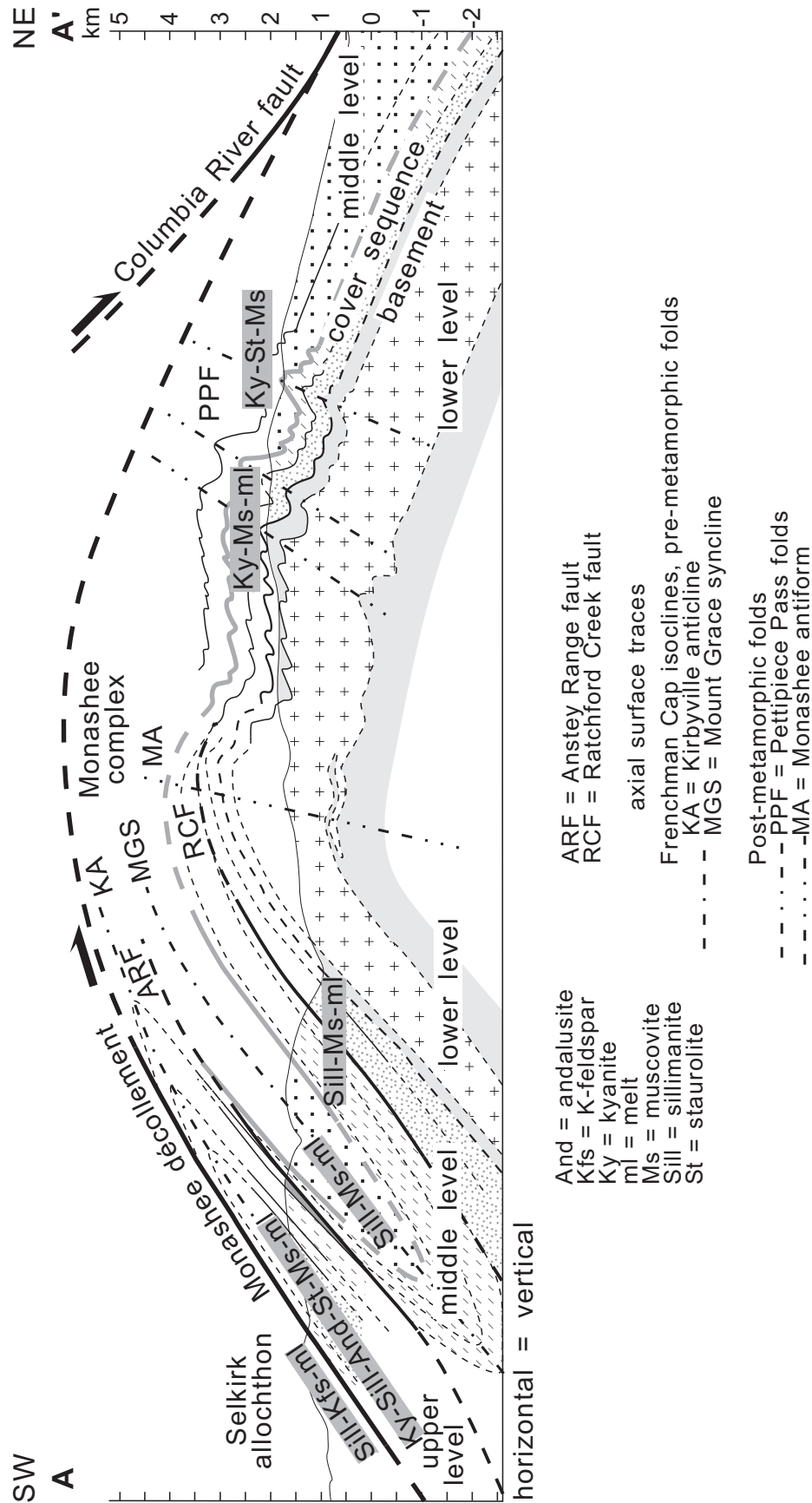
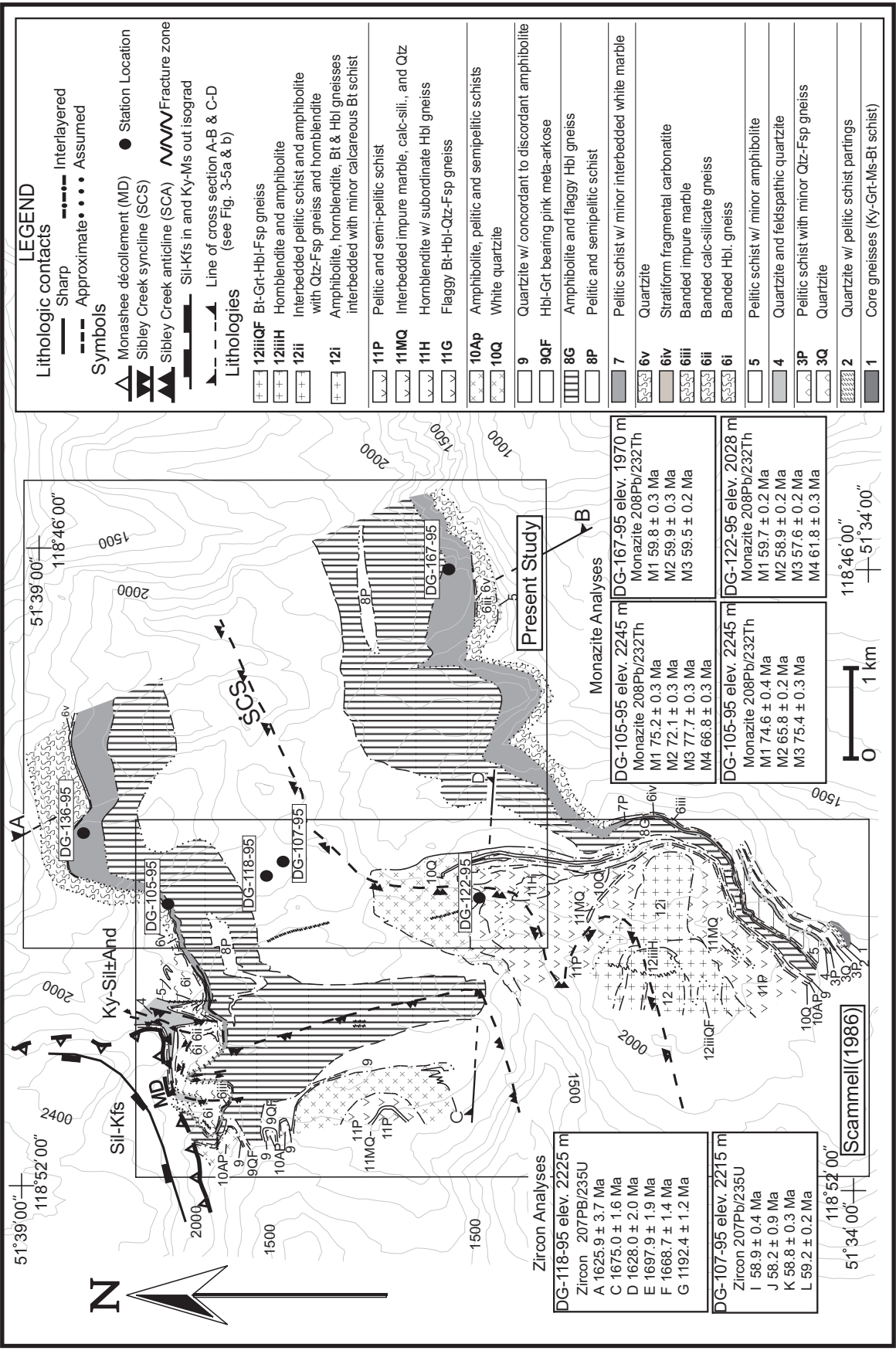
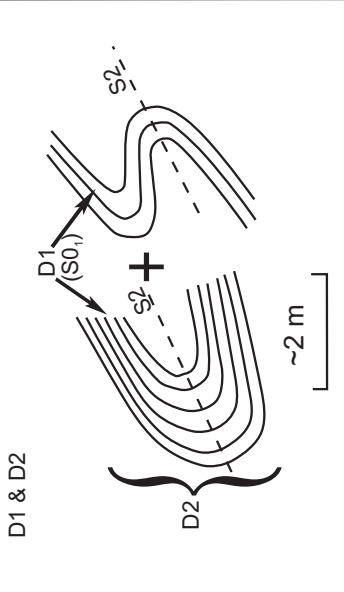
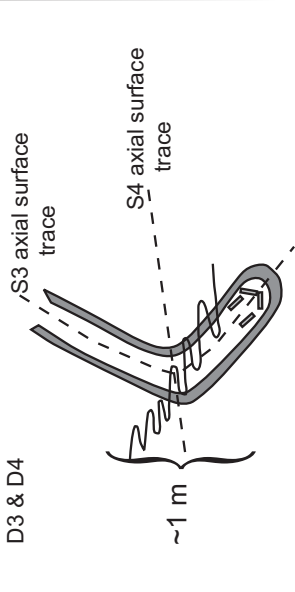
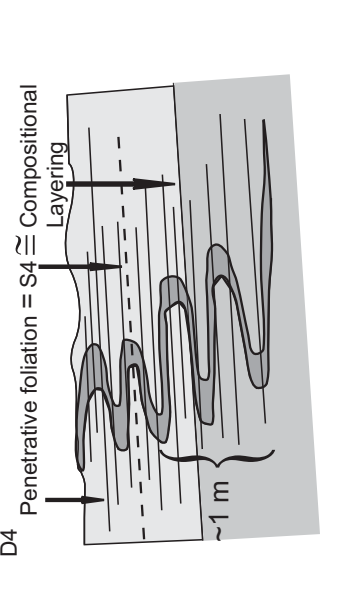


Figure 3-3. Cross section of northern Frenchman Cap dome, taken from J.L. Crowley (in preparation, 1997), modified after Journeay (1986), showing approximate structural position of the metamorphic mineral assemblages in pelitic schists of the cover sequence (data from Journeay (1986) and references therein). Assemblages in the basement are not shown because it is uncertain whether the minerals grew during Proterozoic or early Tertiary metamorphism. Location of section and patterns for rock units are shown in Fig. 3-

Figure 3-4. Lithologic compilation map of northern Frenchman Cap dome incorporating detailed mapping (1:15 000) of Scammell (1986) and the current study. Sample locations (eg. DG-105-95) for this study's geochronology (both monazite and zircon analyses) are included. A-B and C-D indicate cross-sections lines for this chapter. Contour interval is every 100 metres.



Schematic of structures associated with designated phases of deformation (D1, D2, D3, & D4)		Description of structural characteristics	Timing for phases of deformation
	D1 & D2	<p>D1 - very rare in unit 9 quartzite proximal to the hinge zone of the Sibley Creek syncline (SCS)</p> <ul style="list-style-type: none"> - observable as a fabric that contains Muscovite-Biotite +/- Chlorite, folded around D2 structures <p>D2 - rare, in competent layers such as the unit 9 quartzite, proximal to SCS hinge</p> <ul style="list-style-type: none"> - tight, 1-2 m folds that have proper vergence (S₂ or M) with respect to SCS - hinges shallowly plunge to the west-northwest 	<p>D1 - pre-D2, pre-SCS</p> <p>D2</p> <ul style="list-style-type: none"> - younger than youngest age of deposition (~388 Ma, Scammell and Parrish 1993) - possibly younger than Late Cretaceous - pre- to syn-D3 and D4 - pre- to syn-peak metamorphic - overprinted by D5 deformation <p><388 Ma or Late Cretaceous;</p>
	D3 & D4	<p>D3 - observed in only two locations throughout the field area</p> <ul style="list-style-type: none"> - upright, tight folds that fold metamorphic minerals such as Kyanite, biotite, and hornblende 	<p>D3 - folds some metamorphic minerals</p> <ul style="list-style-type: none"> - refolded by D4, i.e., pre-D4 <p>~syn-metamorphic (77.7-59.4 Ma), but outlasted by peak conditions and mineral growth</p>
D4		<p>D4 - these structures are penetrative throughout the field area</p> <ul style="list-style-type: none"> - they have shallow, west-plunging hinges and axial planes - usually tight, asymmetrical, overturned and reclined, sometimes disharmonic; main fabric is defined by alignment of peak metamorphic mineral assemblages; some peak minerals grow over these structures 	<p>D4 - deforms peak metamorphic mineral assemblages, but also overgrown by some; therefore, can be associated with peak metamorphism but did not outlast it</p> <ul style="list-style-type: none"> - overprints SCS; therefore, post-dates initiation of SCS event - overprinted by D5 deformation ~syn-SCS, ~syn-metamorphic (77.7-59.4 Ma), and pre-D5 (Eocene, 59-58 Ma)
<p>Figure 3-5. Diagrammatic table of the structures identified in northern Monashee complex, within the footwall of the Monashee décollement. Structures are presented with respect to superposition and metamorphism.</p>			

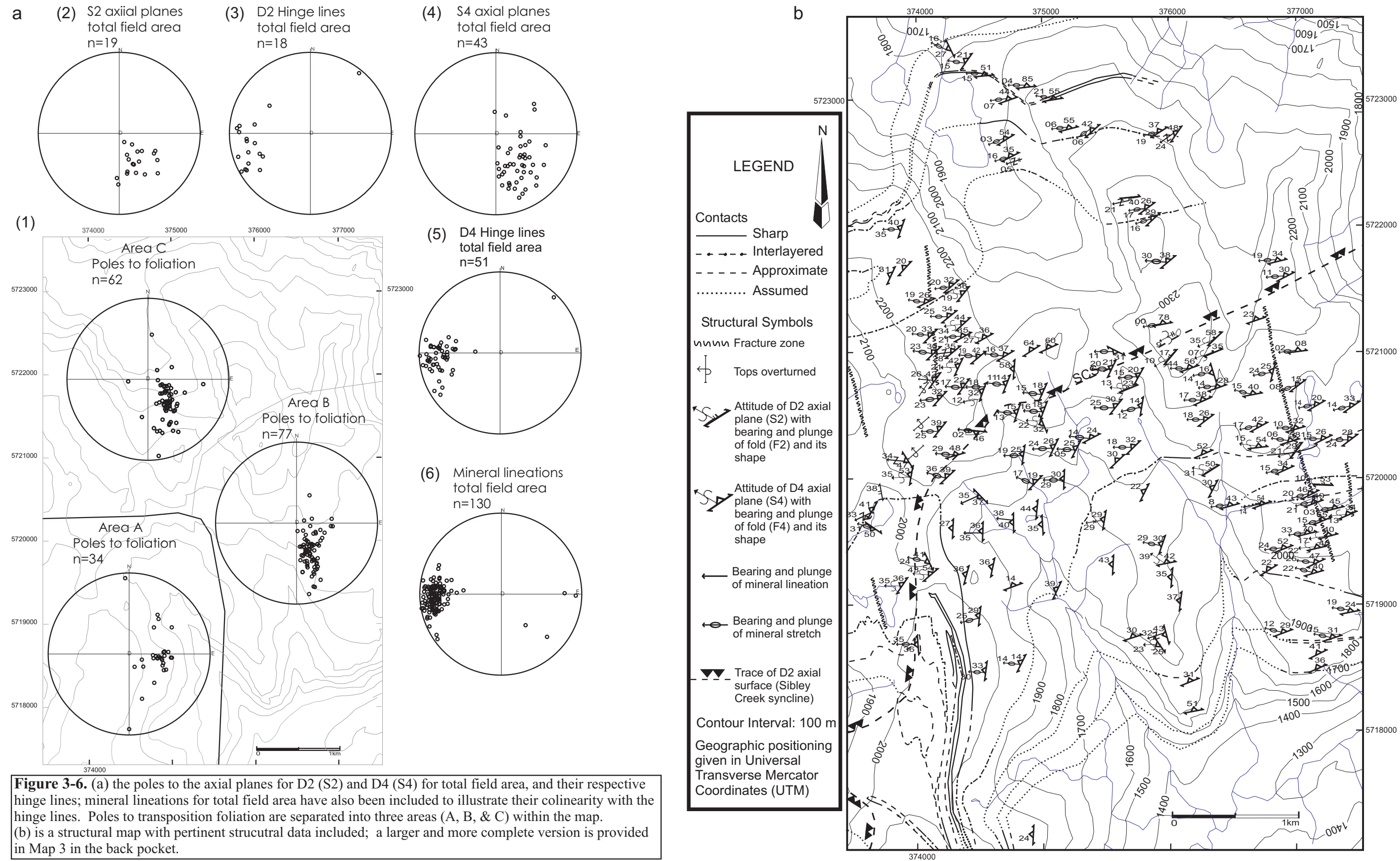
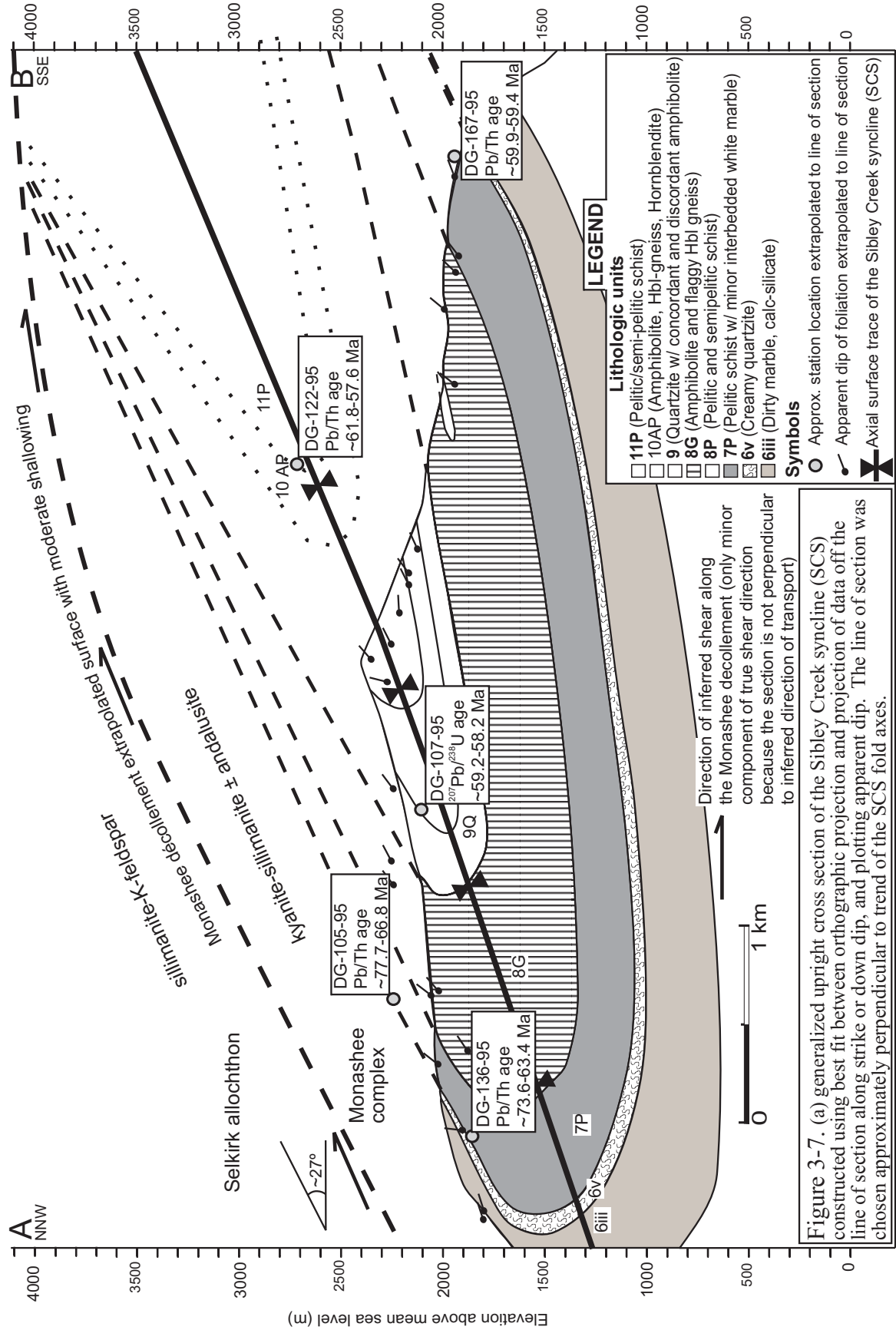
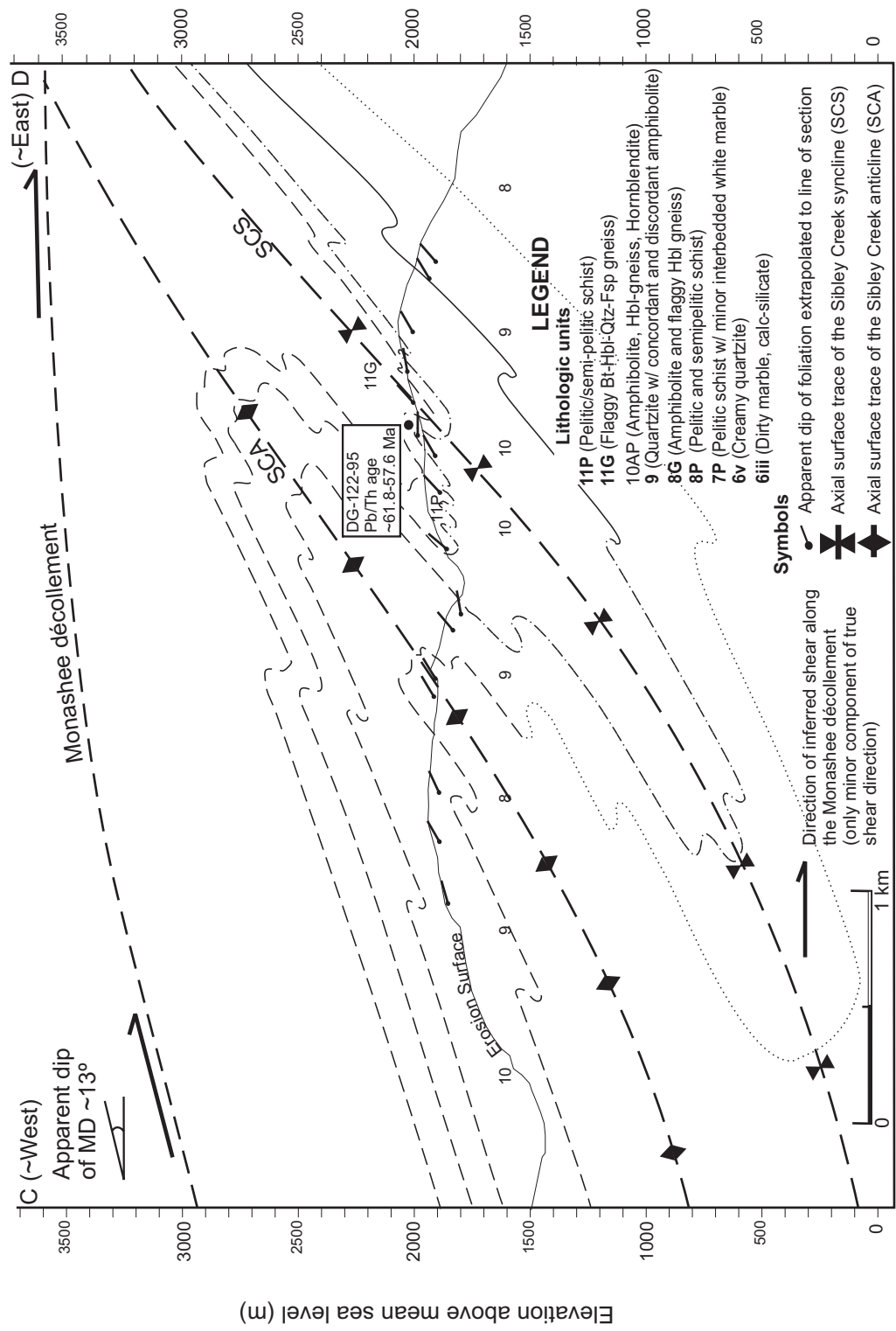


Figure 3-6. (a) the poles to the axial planes for D2 (S2) and D4 (S4) for total field area, and their respective hinge lines; mineral lineations for total field area have also been included to illustrate their colinearity with the hinge lines. Poles to transposition foliation are separated into three areas (A, B, & C) within the map. (b) is a structural map with pertinent strucutral data included; a larger and more complete version is provided in Map 3 in the back pocket.





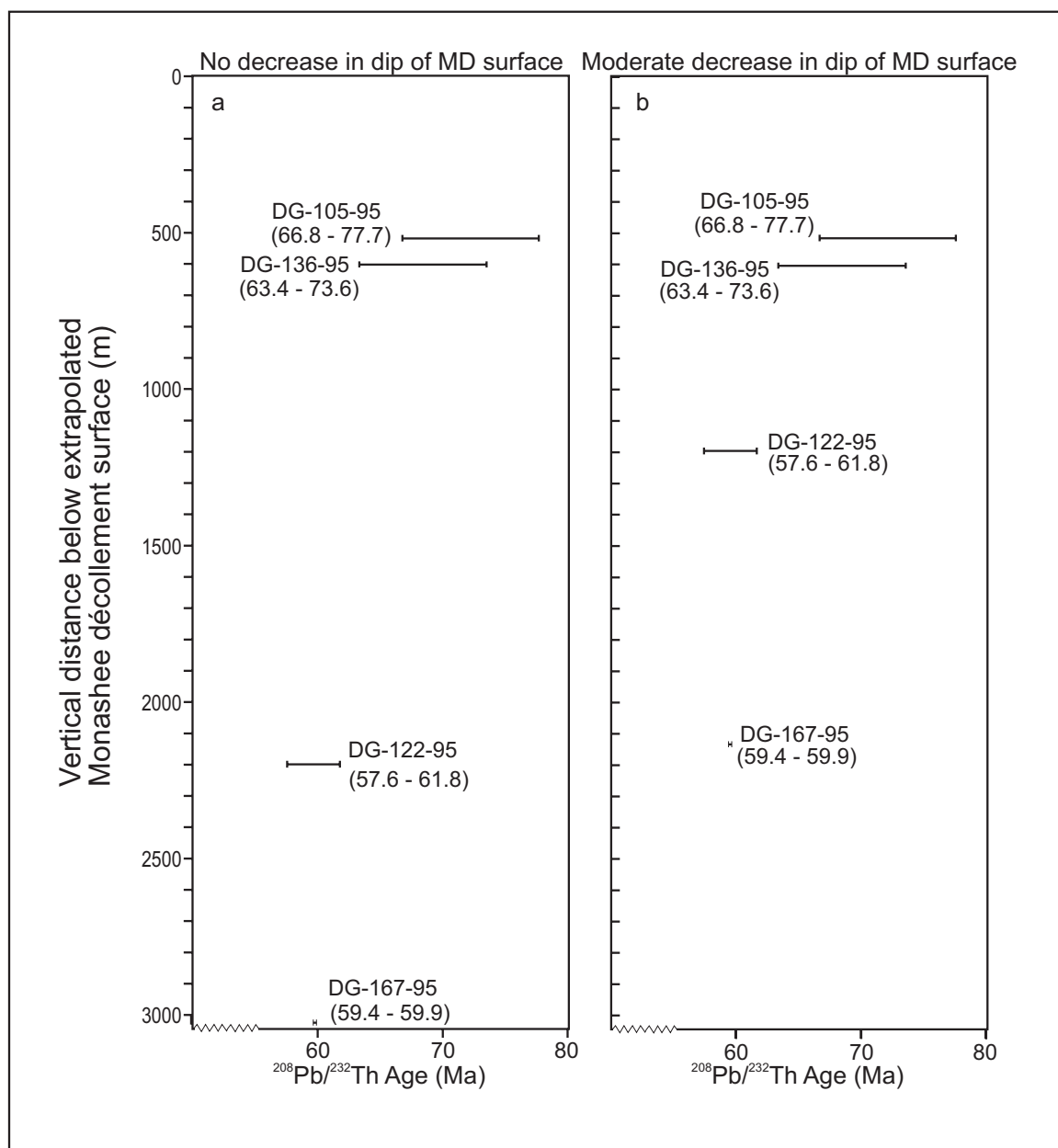


Figure 3-8. Age versus depth (below Monashee décollement, MD) plot illustrating the downward younging and decrease in spread of metamorphic ages within the northern Monashee complex. Plot (a) assumes no decrease in dip of the MD thrust surface, whereas (b) incorporates a moderate decrease.

Figure 3-9a & b. Schematic thermotectonic model for northern Monashee complex. Figures 3-7 a-1 through a-4 illustrate the progressive burial and deformation of the Monashee complex with time. Cordilleran deformation and burial of the Monashee complex beneath the Selkirk allochthon initiates previous to 77 Ma (a-1) and diachronously progresses until ca. 59 Ma (a-4) when the tectonic load is maximum (~20-25 km) and extensional unloading is thought to have initiated (Parrish 1988 and references therein). The Sibley Creek syncline (SCS) originates (pre 77 Ma, a-1) as a buckle fold in a cool environment, but evolves into a thermally aided passive flow fold with increased heat and tectonic load (a-2 to a-4). Rocks initially located to the west are buried and heated first, and are laterally transported over rocks to the east which reach peak temperatures and depths at a later time. Figure 3-7 b illustrates a scaled cross section of the SCS and the flow lines of the rocks initially found to the west as they are transported eastward in a passive flow fashion resulting in the present day geometry of the SCS.

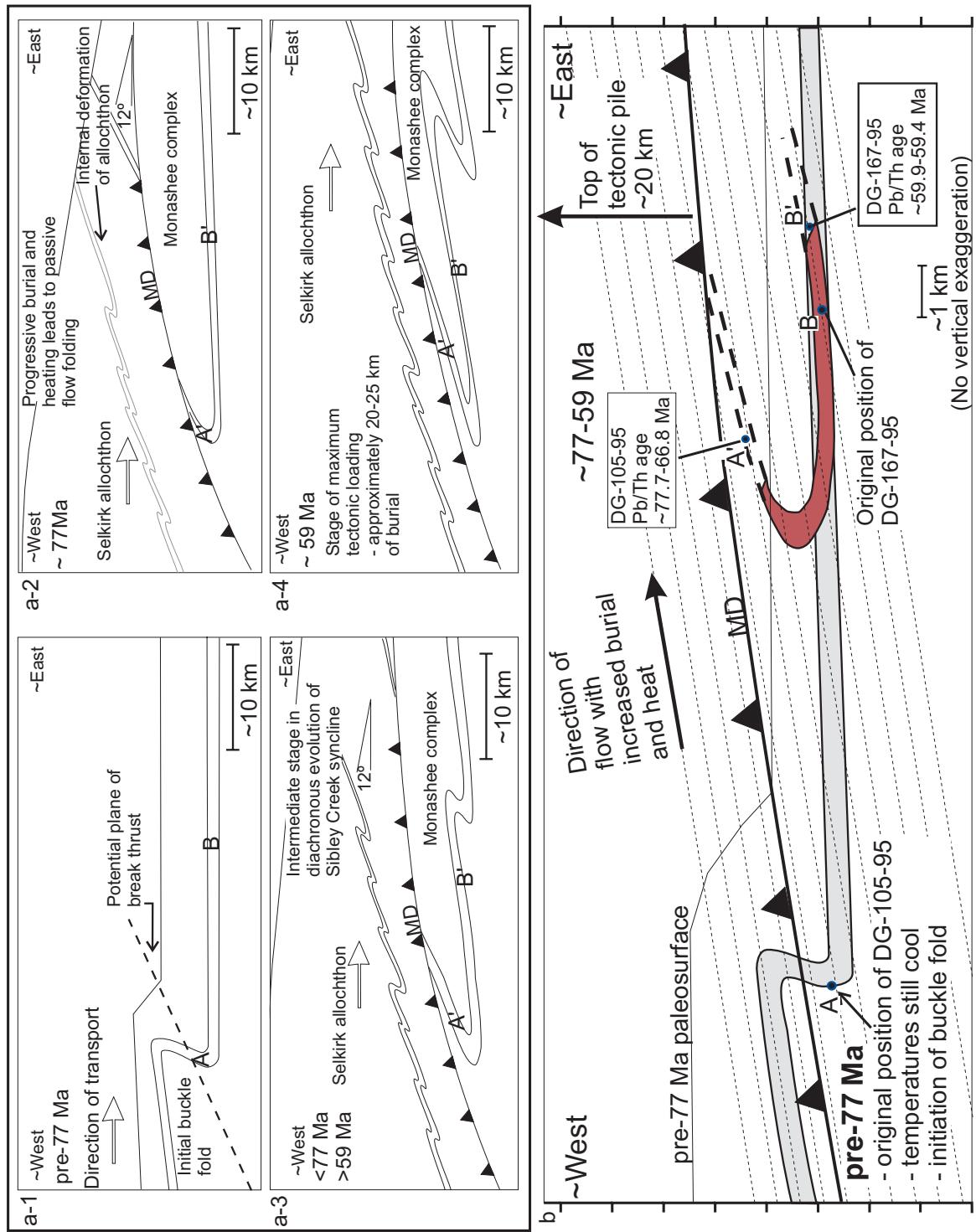




Plate 3-1. Facing northeast, a profile of the kilometre scale Sibley Creek syncline (SCS) is found preserved within a cliff face of the competent unit 9 quartzite. The line drawing below superimposed on a scan of the above photo highlights the geometry of the SCS.



~1 km



Plate 3-2. Facing north, looking down on a smooth unit 9 quartzite face found in the core of the Sibley Creek syncline (SCS). The photo above and scanned image with superimposed line drawing display primary cross-bedding structures which indicate tops down, agreeing with their location in the upper, overturned limb of the SCS. Primary structures such as these within the SCS have also been described by Scammell (1986) and Brown (1980).

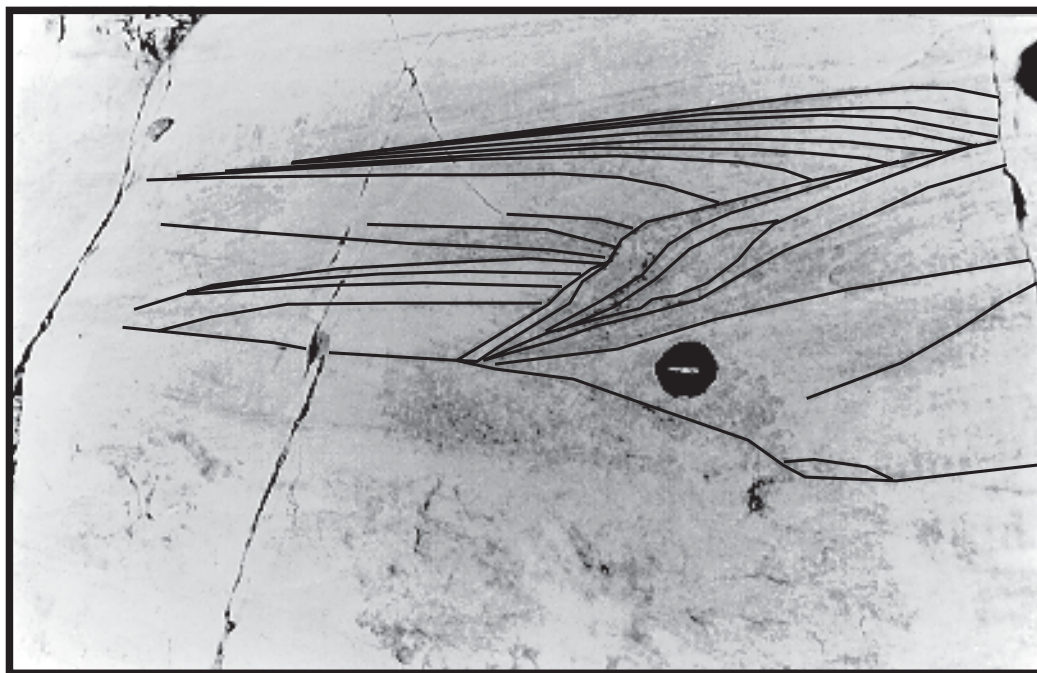
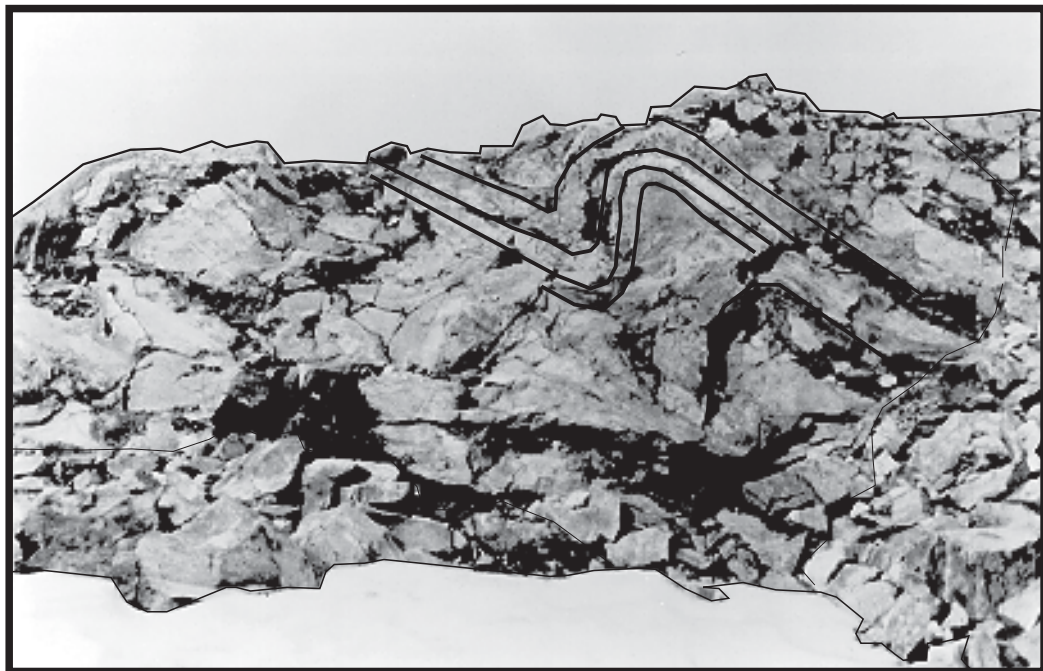




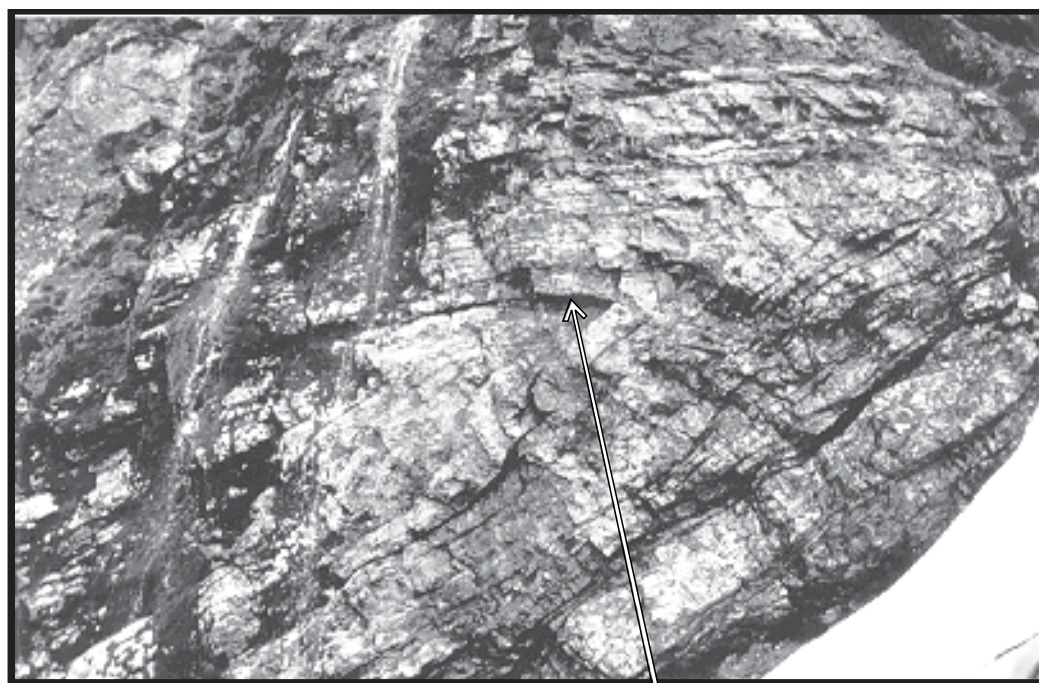
Plate 3-3. Facing east and located in the eastern flank of the current study, this S-shaped, south-verging fold is interpreted to be parasitic to the kilometre scale Sibley Creek syncline (SCS, D2). Folds such as these were found only in close proximity to the hinge zone of the SCS, within the competent unit 9 quartzite.



~1 m



Plate 3-4. Facing west, the above photo and scanned image below illustrate another example of a D2 structure found in the unit 9 quartzite within the lower upright limb of the Sibley Creek syncline (SCS). A foliation surface (S01) defined by the preferred orientation of Ms, Bt, \pm Chl is folded around the hinge of this structure, indicating at least one earlier generation of deformation.

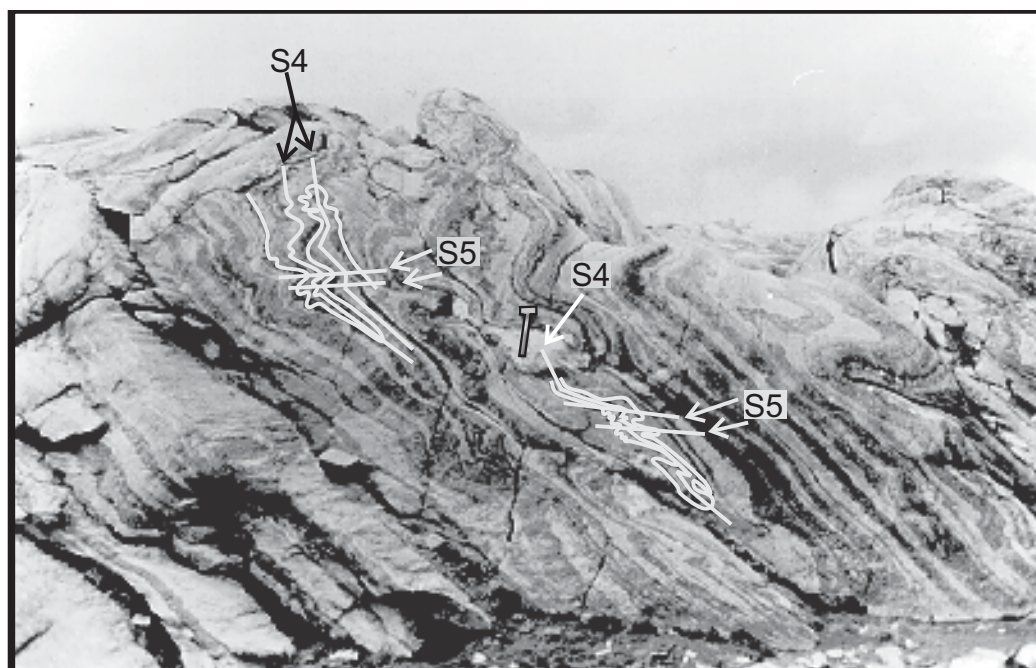


~1 m

S01 foliation surface containing Ms, Bt, \pm Chl folded by a F2 fold interpreted to be parasitic to the SCS



Plate 3-5. Facing west, looking at a outcrop of arenitic and mafic gneiss found in unit 9Q within the upright, lower limb of the Sibley Creek syncline. The above photograph and the digitally enhanced scanned photo beneath illustrate at least two generations of deformation superimposed upon each other at this outcrop. The first observable phase is interpreted to be the tight, upright folds of D3 (F3) which have nearly vertical axial planes. Superimposed upon this are smaller D4 folds (F4) that have sub-horizontal axial planes, which rework the D3 axial planes. Both sets of folds deform peak mineral assemblages and have hinges shallowly plunging to the west.



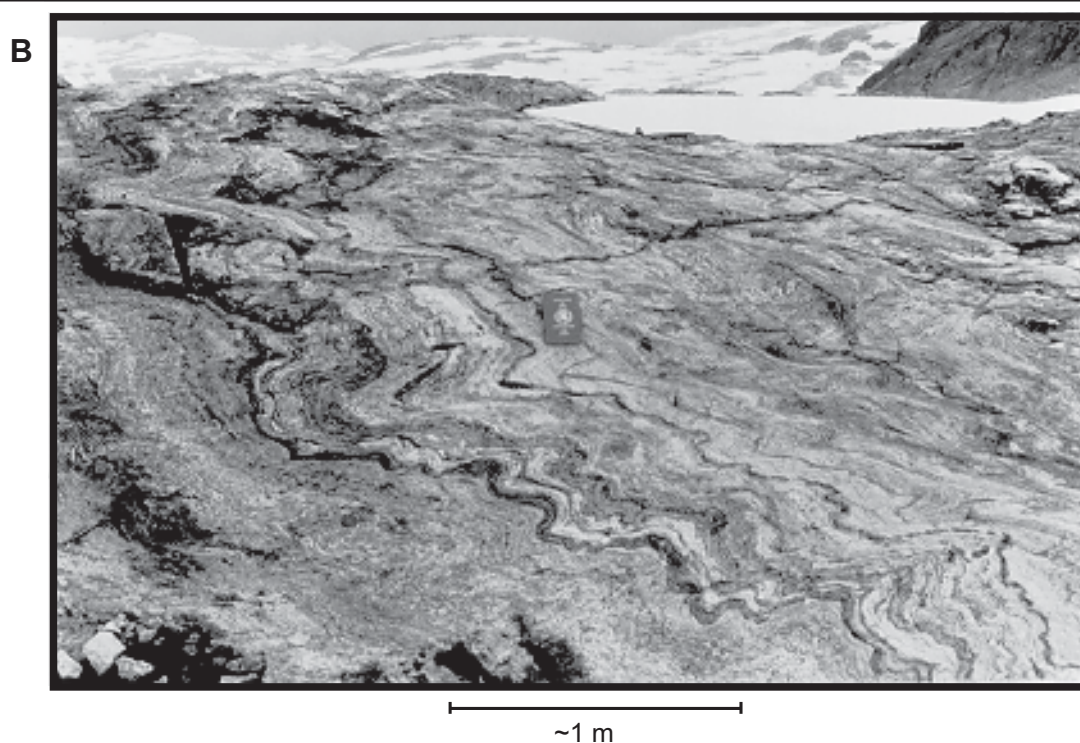
~1 m



Plate 3-6. Fourth generation of deformation (D4)

A. This photo shows a coarse grained pegmatite folded within a dirty marble matrix of unit 6iii. Facing WNW, this photo illustrates a characteristic D4 fold (F4) that is tight to isoclinal, with sub-horizontal axial planes, and shallow west plunging hinges.

B. Facing west, looking at another F4 fold, but with a different geometry. These are reclined, disharmonic folds which deform peak minerals such as kyanite and hornblende of unit 8G. Hinges plunge moderately to the west.





~10 m

Plate 3-7. Facing north, looking at a late brittle normal fault (D5) with apparent down to the east sense of displacement. This brittle feature and most other joints, fractures, and faults found in this study trend mainly to the north. They are interpreted to be associated with the late stages of tectonic unloading of the Monashee complex facilitated by extensional faulting along the Eocene Columbia River and Okanagan Valley faults.

Blank page

Chapter 4. Summary of conclusions

In light of the new data presented in this thesis the following conclusions have been made:

(1) Reverse discordance in U-Pb space for monazite analyses is caused by excess ^{206}Pb .

(2) The calculation proposed by Schärer (1984) can correct this problem only if the monazite grew in an ideal stable environment which meets all the criteria for the calculation. Unfortunately, these criteria are seldom met for most rocks found in high-grade metamorphic terranes that have experienced significant deformation.

(3) The $^{208}\text{Pb}/^{232}\text{Th}$ chronometer is an essential tool for monazite geochronology for the following reasons:

(a) It is immune to the problem of excess ^{206}Pb caused by an initial disequilibrium of ^{230}Th or any other intermediate daughter isotope disequilibrium concerning monazite U-Th-Pb systematics.

(b) The use of both Pb/U and Pb/Th chronometry has illustrated that U loss in metamorphic monazite from high-grade deformed terranes is fairly ubiquitous and is undetectable using only Pb/U chronometry.

(c) The $^{232}\text{Th} - ^{208}\text{Pb}$ chronometer is mostly unaffected by this phenomenon, and the ages produced are the best estimate for the timing of monazite crystallization.

(4) The U correction outlined in Chapter 2 (equation [4]) is a valid process for correcting the Pb/U ratios and ages. Although, it cannot be relied upon to account for the actual amount or timing of U loss, it does correct for the U loss and also illustrates the commonality of U loss in U-bearing minerals.

(5) The residual discordance of the corrected data in U-Th-Pb space may be caused by

an initial disequilibrium of ^{231}Pa in the ^{235}U - ^{207}Pb decay chain, but further U-Th-Pb systematics studies concerning this problem need to be performed before any hard conclusions can be made.

(6) Within the field area for the current study, burial, heating, and growth of peak metamorphic assemblages had to have initiated during the Late Cretaceous on or before the oldest monazite date produced (77.7 ± 0.3 Ma). Additionally, the monazite ages produced in this study suggest that there is a systematic inversion of peak metamorphic ages and that the higher level samples grew for a longer duration of time in a more complex thermal regime.

(7) Structural evidence suggests that the SCS deforms a pre-existing foliation surface. Therefore, the Sibley Creek syncline post-dates the earliest generation of deformation affecting the cover sequence stratigraphy of the Monashee complex.

(8) There are at least five discernible generations of deformation found in the SCS area. These generations are local markers of progressive deformation, but each generation evolves diachronously as a function of structural depth beneath the Selkirk allochthon.

(9) Major tectonic loading of the complex occurred at least by 77.7 Ma and continued until approximately 59 Ma, when it was rapidly denuded by a combination of extensional faulting and erosion.

(10) An analysis of the structure and geochronology of the area indicates that the pattern of dates relative to the overlying allochthon is consistent with distributed ductile deformation of isograd surfaces by substantial east-directed shear strain and attendant attenuation in the footwall, leading to relative lateral transfer of rocks preserving evidence of inverted diachronous metamorphism. Previous tectonic models that attribute the distribution of diachronous and inverted peak metamorphic assemblages solely to

conductive heating from a hot overthrust heat source are rejected.

REFERENCES

- Armstrong, R.L., Parrish, R.R., van der Heyden, P., Scott, K., Runkle, D., and Brown, R.L. 1991. Early Proterozoic basement exposures in the southern Canadian Cordillera: core gneiss of Frenchman Cap, Unit 1 of the Grandforks Gneiss and the Vaseaux Formation. *Canadian Journal of Earth Sciences*, **28**: 1169-1201.
- Bacon, M.P., and Rosholt, J.N. 1982. Accumulation rates of ^{230}Th , ^{231}Pa , and some transition metals on the Bermuda Rise. *Geochimica et Cosmochimica Acta*, **46**: 651-666.
- Bhattacharya, D.S., and Das, K. K., 1983. Inversion of metamorphic zones in the lower Himalaya at Gangtok, Sikkim, India. *Journal of Geology*, **91**: 98-102.
- Bordet, P. 1961. Recherches géologiques dans l'Himalaya du Népal, région du Makalu. Paris, centre Nationale de Recherche Scientifique, 275 p.
- Brown, R.L. 1980. Frenchman Cap dome, Shuswap complex, British Columbia: a progress report. *In*: Current Research, part A. Geological Survey of Canada, Paper 80-1A, pp. 47-51.
- Brown, R.L., and Journeay, J.M. 1987. Tectonic denudation of the Shuswap metamorphic terrane of southeastern British Columbia. *Geology*, **15**: 142-146.
- Brown, R.L., Journeay, J.M., Lane, L.S., Murphy, D.C., and Rees, C.J. 1986. Obduction, backfolding and piggyback thrusting in the metamorphic hinterland of the southeastern Canadian Cordillera. *Journal of Structural Geology*, **8**: 255-268.
- Brown, R.L., Carr, S.D., Johnson, B.J., Coleman, V.J., Cook, F.A., and Varsek, J.L. 1992. The Monashee décollement of the southern Canadian Cordillera: a crustal scale shear zone linking the Rocky Mountain Foreland Belt to lower crust beneath accreted terranes. *In* Thrust Tectonics. *Edited by* K.R. McClay, pp. 357-364.
- Brunel, M., and Kienast, J.R. 1986. Etude petrostructurale des chevauchements ductiles himalayens sur la traversale de l'Everest-Makalu (Népal oriental). *Canadian Journal of Earth Sciences*, **23**: 1117-1137.
- Carr, S.D. 1990. Late Cretaceous-early Tertiary tectonic evolution of the southern Omineca Belt, Canadian Cordillera. Unpublished Ph.D. thesis, Carleton University, Ottawa, ON.
- Carr, S.D. 1991. Three crustal zones in the Thor-Odin-Pinnacles area, southern Omineca Belt, British Columbia. *Canadian Journal of Earth Sciences*, **28**: 2003-2023.

- Carr, S.D. 1992. Tectonic setting and U-Pb geochronology of the Early Tertiary Ladybird leucogranite suite, Thor-Odin-Pinnacles area, southern Omineca Belt, British Columbia. *Tectonics*, **11**: 258-278.
- Cook, F.A., Varsek, J.L., Clowes, R.M., Kanasewich, E.R., Spencer, C.S., Parrish, R.R., Brown, R.L., Carr, S.D., Johnson, B.J., and Price, R.A. 1992. Lithoprobe crustal reflection cross section of the southern Canadian Cordillera. 1. Foreland Thrust and Fold Belt to Fraser River fault. *Tectonics*, **11**: 12-25.
- Dodson, M.H. 1973. Closure temperature in cooling geochronological and petrological systems. *Contributions to Mineralogy and Petrology*, **40**: 259-274.
- England, P.C., and Molnar, P. 1993. The interpretation of inverted metamorphic isograds using simple physical calculations. *Tectonics*, **12**: 145-157.
- England, P.C., and Thompson, A.B. 1984. Pressure-Temperature-Time paths of regional metamorphism I. Heat transfer during the evolution of regions of thickened continental crust. *Journal of Petrology*, **25-4**: 894-928.
- Faure, G. 1986. Mass spectrometry. *In* Principles of isotope geology. 2nd Edition. Wiley, New York, NY, pp. 61-63.
- Gabrielse, H., and Yorath, C.J. 1991. Tectonic synthesis. *In*: Geology of the Cordilleran Orogen in Canada. *Edited by* H. Gabrielse, and C.J. Yorath. Geological Survey of Canada, Geology of Canada, No. 4, pp. 677-705.
- Grujic, D., Casey, M., Davidson, C., Hollister, L., Kundig, R., Pavlis, T., and Schmid, S. 1996. Ductile extrusion of the Higher Himalayan Crystalline in Bhutan: Evidence from quartz microfabrics. *Tectonophysics*, **260**: 21-43.
- Oxburgh, E.R. 1981. Heat flow and magma genesis. *In* Physics of magmatic processes. *Edited by* R.B. Hargraves. Princeton University, Princeton, New Jersey, Chapter 5, pp.xx-xx.
- Heaman, L.M., and Parrish, R.R. 1991. U-Pb geochronology of accessory minerals. *In* Applications of radiogenic isotope systems to problems in geology. *Edited by* L. Heaman and J.N. Ludden. Mineralogical Association of Canada, Short Course Handbook, **19**: 59-102.
- Hofmann, A. 1971. Fractionation correction for mixed-isotope spikes of Sr, K, and Pb. *Earth and Planetary Science Letters*, **10**: 397-402.
- Höy, T. 1982. Stratigraphy and structural setting of stratabound lead-zinc deposits in southeastern B.C. *Canadian Institute of Mining*, **75**: 114-134.
- Höy, T., and Brown, R.L. 1980. Geology of eastern margin of Frenchman Cap dome.

- Ministry of Energy, Mines, and Petroleum Resources, Preliminary Map 43.
- Hubbard, M.S. 1989. Thermobarometric constraints on the thermal history of the Main Central Thrust Zone and Tibetan Slab, eastern Nepal Himalaya. *Journal of Metamorphic Geology*, **7**: 19-30.
- Hubbard, M.S. 1996. Ductile shear as a cause of inverted metamorphism: example from the Nepal Himalaya. *The Journal of Geology*, **104**: 493-499.
- Jamieson, R.A. 1986. P-T paths from high temperature shear zones beneath ophiolites. *Journal of Metamorphic Geology*, **4**: 3-22.
- Jamieson, R.A., Beaumont, C., Hamilton, J., and Fullsack, P. 1996. Tectonic assembly of inverted metamorphic sequences. *Geology*, **24**: 839-842.
- Johnson, B.J., and Brown, R.L. 1996. Crustal structure and early Tertiary extensional tectonics of the Omineca Belt at 51° N latitude, southern Canadian Cordillera. *Canadian Journal of Earth Sciences*, **33**: 1596-1611.
- Journeay, J.M. 1986. Stratigraphy, internal strain and thermotectonic evolution of northern Frenchman Cap dome: an exhumed duplex structure, Omineca hinterland, SE Canadian Cordillera. Unpublished Ph.D. thesis, Queen's University, Kingston, ON.
- Journeay, J.M., and Brown, R.L. 1986. Major tectonic boundaries of the Omineca Belt in southern British Columbia: a progress report. Geological Survey of Canada, Paper 86-1A, pp. 81-88.
- Keppler, H., and Wyllie, J. 1990. Role of fluids in transport and fractionation of uranium and thorium in magmatic processes. *Nature*, **348**: 531-533.
- Kretz, R. 1983. Symbols for rock-forming minerals. *American Mineralogist*, **68**: 277-279.
- Krogh, T.E. 1982. Improved accuracy of U-Pb ages by the creation of more concordant systems using an air abrasion technique. *Geochimica et Cosmochimica Acta*, **46**: 637-649.
- Lefort, P. 1975. Himalayas: the collided range. Present knowledge of the continental arc. *American Journal of Science*, **275-A**: 1-44.
- Lefort, P. 1986. Metamorphism and magmatism during the Himalayan collision. *In* Collision tectonics. *Edited by* M.P. Coward and A.C. Ries. Geological Society of London Special Publication 19, pp. 159-172.

- McMillan, W. J. 1970. West flank, Frenchman's Cap gneiss dome, Shuswap terrane, British Columbia. *In* Structure of the Southern Canadian Cordillera. *Edited by* J.O. Wheeler. Geological Association of Canada, Special Paper 6, pp. 99-122.
- McNicoll, V.J., and Brown, R.L., 1995, The Monashee décollement at Cariboo Alp, southern flank of the Monashee complex, southeastern British Columbia, Canada. *Journal of Structural Geology*, **17**: 17-30.
- Parrish, R.R. 1987. An improved micro-capsule for zircon dissolution I U-Pb geochronology. *Chemical Geology (Isotope Geoscience Section)*, **66**: 99-102.
- Parrish, R.R. 1990. U-Pb dating of monazite and its application to geological problems. *Canadian Journal of Earth Sciences*, **27**: 1431-1450.
- Parrish, R.R. 1995. Thermal evolution of the southeastern Canadian Cordillera. *Canadian Journal of Earth Sciences*, **32**: 1618-1642.
- Parrish, R.R., Roddick, J.C., Loveridge, W.D., and Sullivan, R.W. 1987. Uranium-lead analytical techniques at the Geochronology Laboratory, Geological Survey of Canada. *In*: Radiogenic age and isotopic studies: Report 1. Geological Survey of Canada, Paper 87-2, pp. 3-7.
- Parrish, R.R., Carr, S.D., and Parkinson, D.L. 1988. Eocene extensional tectonics and geochronology of the southern Omineca Belt, British Columbia and Washington. *Tectonics*, **7**: 181-212.
- Psutka, J.F. 1978. Structural setting of the Downie Slide, northeast flank of Frenchman Cap gneiss dome, Shuswap Metamorphic Complex, southeastern British Columbia. Unpublished M.Sc. thesis, Carleton University, Ottawa, Canada.
- Ramsay, J.G., and Huber, M.I. 1987. Fold Classification. *In* The techniques of modern structural geology, v. 2: Folds and fractures. London Academic Press, London, UK.
- Read, P.B. 1980. Stratigraphy and structure: Thor-Odin to Frenchman Cap "domes", Vernon east-half map area, southern British Columbia. *In* Current Research, part A. Geological Survey of Canada, Paper 80-1A, pp. 19-25.
- Read, P.B., and Brown, R.L. 1981. Columbia River fault zone: southeastern margin of the Shuswap and Monashee complexes, southern British Columbia. *Canadian Journal of Earth Sciences*, **18**: 1127-1145.
- Reddy, S.M., Searle, M.P., and Massey, J.A. 1993. Structural evolution of the High Himalayan Gneiss sequence, Langtang Valley, Nepal. *In* Himalayan tectonics. *Edited by* P.J. Treloar and M.P. Searle. Geological Society of London Special Publication, **74**: 375-389.

- Reesor, J.E., and Moore, J.M., Jr. 1971. Petrology and structure of Thor-Odin gneiss dome, Shuswap metamorphic complex, British Columbia. Geological Survey of Canada, Paper 81-1A, pp. 169-173.
- Roddick, J.C. 1987. Generalized numerical error analysis with applications to geochronology and thermodynamics. *Geochimica et Cosmochimica Acta*, **51**: 2129-2135.
- Roddick, J.C., Loveridge, W.D., and Parrish, R.R. 1987. Precise U/Pb dating of zircon at the sub-nanogram level. *Chemical Geology (Isotope Geoscience Section)*, **66**: 111-121.
- Royden, L.H. 1993. The steady state thermal structure of eroding orogenic belts and accretionary prisms. *Journal of Geophysical Research*, **98**: 4487-4507.
- Ruppel, C., and Hodges, K.V., 1994. Pressure-temperature-time paths from two-dimensional thermal models: prograde, retrograde, and inverted metamorphism. *Tectonics*, **13**: 17-44.
- Scammell, R.J. 1986. Stratigraphy, structure and metamorphism of the north flank of the Monashee complex, southeastern British Columbia: a record of the Proterozoic crustal thickening. Unpublished M.Sc. thesis, Carleton University, Ottawa, Canada.
- Scammell, R.J., and Brown, R.L. 1990. Cover gneisses of the Monashee Terrane: a record of synsedimentary rifting in the North American Cordillera. *Canadian Journal of Earth Sciences*, **27**: 712-726.
- Scammell, R.J., and Parrish, R.R. 1993. U-Pb zircon chronometry from a metamorphosed felsic volcanoclastic rock in cover gneisses, Monashee terrane, southeastern British Columbia. *Geological Association of Canada, Program with Abstracts* **18**: A93.
- Schärer, U. 1984. The effect of initial ^{230}Th disequilibrium on young U-Pb ages: the Makalu case, Himalaya. *Earth and Planetary Science Letters*, **67**: 191-204.
- Searle, M., Waters, D.J., Rex, A.J., and Wilson, R.N. 1992. Pressure, temperature, and time constraints on Himalayan metamorphism from eastern Kashmir and western Zaskar. *Geological Society of London Journal*, **149**: 753-773.
- Sears, J.W., and Price, R.A. 1978. The Siberian connection: a case for Precambrian separation of the North American and Siberian cratons. *Geology*, **6**: 267-270.
- Suppe, J. 1981. Mechanics of mountain building and metamorphism in Taiwan. *Geological Society of China Memoir*, **4**: 67-89.
- Tilley, C.E. 1925. Preliminary surveys of metamorphic zones in the southern Highlands of Scotland. *Quarterly Journal of Geological Sciences*, **81**: 100-112.

- Treloar, P.J., Williams, M.P., and Coward, M.P. 1989. Metamorphism and crustal stacking in the North India Plate, North Pakistan. *Tectonophysics*, **165**: 167-184.
- Wetherill, G.W. 1953. Discordant uranium-lead ages. *American Geophysical Union Transactions*, **37**: 320-326.
- Wheeler, J.O. 1965. Big Bend map-area, British Columbia. *Geological Survey of Canada, Paper 64-32*, pp. 1-37.
- Wheeler, J.O., and McFeely, P. 1991. Tectonic assemblage map of the Canadian Cordillera and adjacent parts of the United States of America. *Geological Survey of Canada, Map 1712A*, scale 1:2 000 000.
- Willis, B. 1893. The mechanics of Appalachian structures. *United States Geological Survey 13th Annual Report 1891-1892*, **2**: 212-281.

Appendix 1: Errors for Th-Pb chronometry (personal communication, R. Parrish 1996)

Sources of error are approximated as follows:

(1) Errors related to uncertainty in the $^{230}\text{Th}/^{205}\text{Pb}$ ratio of the spike, i.e.,

a = 0.1%, estimated error in the reproducibility of repeated measurements of spike ^{230}Th - ^{205}Pb , calibrated against a standard reference solution

b = the uncertainty in the $^{230}\text{Th}/^{205}\text{Pb}$ ratio of the spike emanating from the absolute uncertainty in the $^{230}\text{Th}/^{232}\text{Th}$ fractionation in the above measurements (a), estimated at $\pm 0.05\%$ /a.m.u.

c = the uncertainty in the $^{230}\text{Th}/^{205}\text{Pb}$ ratio of the spike emanating from the uncertainty in the Pb fractionation in the above measurements (a), estimated at $\pm 0.02\%$

(2) Errors related to uncertainties tied to each individual measurement on monazite or zircon, i.e.,

d = the uncertainty in the $^{230}\text{Th}/^{232}\text{Th}$ fractionation of each individual run on a monazite sample (0.1%)

e = the uncertainty of fractionation in the Pb isotopic ratios for individual runs (0.09% for the 3 a.m.u. difference from 208 to 205)

f = the measured uncertainty in the $^{230}\text{Th}/^{232}\text{Th}$ ratio for each analysis (Th)

g = the measured uncertainty in the $^{207}\text{Pb}/^{205}\text{Pb}$ ratio for each analysis (Pb)

(3) The error introduced by the uncertainty in the common Pb correction, i.e.,

h = $100/((^{208}\text{Pb}/^{204}\text{Pb})_{\text{measured}} - (^{208}\text{Pb}/^{204}\text{Pb})_{\text{Stacey-Kramers model common Pb}})$, in percent for each run,

where the common value is the calculated model composition

Total error propagation would be as follows, assuming that there is no correlation between any of these errors:

$$A = {}^{208}\text{Pb}/{}^{232}\text{Th error (1 } \sigma \text{ in \%)} = \sqrt{(a^2) + (b^2) + (c^2) + (d^2) + (e^2) + (f^2) + (g^2) + (h^2)}$$

$$B = \text{final Pb/Th age error (2 } \sigma \text{ in Ma)} = (2A/100)({}^{208}\text{Pb}/{}^{232}\text{Th age})$$

Appendix 2: Description of spike preparation (as summarized from notes provided by R.R. Parrish)

(1) Pure metal of natural Th, U, and SRM 982 Pb were weighed to $\pm 2 \times 10^{-6}$ g on a calibrated MettlerTM micro-balance and dissolved to make a reference solution whose concentrations and isotopic compositions of Th, U, and Pb are precisely known.

(2) A mixed spike was prepared by obtaining isotopic tracers of ^{230}Th , ^{235}U , ^{233}U , and ^{205}Pb and mixing known amounts of these individual tracers in appropriate isotopic ratios.

(3) The precise isotopic composition of the dual U tracer was determined by the critical mixture measurements following Hofmann (1971). During calibration of the concentrations of ^{230}Th , ^{235}U , ^{233}U , and ^{205}Pb in the spike, U and Pb mass spectrometric measurements were normalized using the known isotopic compositions of the tracer U and the reference solution Pb. In practice, this meant mixing a known weight of each solution, letting the isotopes equilibrate, measuring the isotopic composition of the mixtures, and then performing isotope dilution unmixing calculations following normalization of isotopic compositions of U and Pb. This had to be done several times (10) to obtain adequate reproducibility of inter-elemental isotopic ratios. A successful conclusion to this step enabled high-precision Th-U-Pb geochronology on the chosen samples to proceed.

Appendix 3: Pb/Th age calculations

Constants:									
$^{232}\text{Th}/^{230}\text{Th}$ spike	0.001287	Atomic Weights							
$\lambda^{238}\text{U}/\lambda^{230}\text{Th}$	0.00001685	^{232}Th	232.0382	^{230}Th	230.0331	^{208}Pb	207.9766	$\text{U/Th}_{\text{mineral}} \times \lambda^{238}\text{U}/\lambda^{230}\text{Th} = ^{230}\text{Th}/^{232}\text{Th}$ in sample	
^{230}Th conc. spike (nmol/g)*	6.0615	^{230}Th	230.0331	^{208}Pb	207.9766	*note: [^{230}Th] is mean of ten sets of measurements			
Decay const. for ^{232}Th	4.9475E-11								
Fractionation $^{230}\text{Th}/^{232}\text{Th}$, meas.	0.998								
Th blank (g)	4.00E-12	Avagadro's #		6.02252E+23					
Th blank (nmol)	1.72385E-05								
Batch ID	844-25	844-26	844-27	844-28	849-1	849-2	849-3		
Project#	DAN#1	DAN#1	DAN#1	DAN#1	Z4093	Z4093	Z4093		
Sample#	DG-167-95	DG-167-95	DG-167-95	DG-167-95	DG-136-95	DG-136-95	DG-136-95		
Mineral fraction ID	M-1	M-2	M-3	M-4	M-1	M-2	M-3		
U conc. in sample (ppm)	5142.20	5941.20	4094.40	4571.00	4876.50	4474.80	3882.80		
$^{230}\text{Th}/^{232}\text{Th}$ measured	0.0403392	0.0451316	0.0346207	0.0304937	0.094386	0.145033	0.17755		
$(\text{U/Th})_{\text{mineral}}$ measured ^a	0.116043972	0.10313226	0.110936405	0.114660031	0.124403227	0.111896434	0.123666254		
$^{230}\text{Th}/^{232}\text{Th}$ sample, measured	0.0000019553	0.0000017378	0.0000018693	0.0000019320	0.0000020962	0.0000018855	0.0000020838		
weight of spike (g)	0.0753	0.0901	0.0875	0.093	0.07691	0.0646	0.07347		
weight of sample (g)	0.0000609	0.0000501	0.0000990	0.0001106	0.0000301	0.0000161	0.0000191		
Radiogenic ^{208}Pb (nmol/g)	551.1649	718.4483	456.8493	493.2788	581.2166	527.4915	471.7352		
Calculated U fractionation	0.0619	0.0613	0.0631	-0.0025	0.0455	0.107	0.0677		
$^{208}\text{Pb}/^{204}\text{Pb}$ sample, measured	4998.1	5044.7	4975.6	4281.5	2154.7	3460.5	2668.9		
Calculation of Th concentration									
^{230}Th spike (nmol)	0.45643095	0.54614115	0.53038125	0.5637195	0.466189965	0.3915729	0.445338405		
$(^{230}\text{Th}/^{232}\text{Th})_{\text{fract. corrected}}$, meas.	0.040258522	0.045041337	0.034551459	0.030432713	0.094197228	0.144742934	0.1771949		
^{232}Th sample (nmol)	11.33735955	12.12511318	15.35040004	18.52347922	4.94867785	2.70490221	2.51279425		
^{232}Th conc. sample (nmol/g)	186163.5394	242018.2271	155054.5458	167481.7289	164681.4591	168006.3482	131905.2100		
Th conc. in sample (ppm)	43197.22152	56157.66897	35978.71223	38862.30907	38212.54954	38984.03763	30607.17506		
Age calculation									
$^{208}\text{Pb}/^{232}\text{Th}$	0.002960649	0.002968571	0.002946378	0.002945269	0.003529338	0.003139712	0.003576320		
Error (\pm 1 s.d. in % of ratio)	0.212	0.232	0.206	0.200	0.213	0.208	0.207		
Age (Ma)	59.75290	59.91255	59.46530	59.44296	71.21021	63.36115	72.15644		
Error (\pm 2 s.d. in Ma)	0.25386	0.27778	0.24514	0.23799	0.30357	0.26328	0.29889		

^a As measured by isotope dilution; uncertainty is approximately $\pm 0.5\%$ (2σ)

Appendix 3: Continued

Constants:											
$^{232}\text{Th}/^{230}\text{Th}$ spike	0.001287	Atomic Weights									
$\lambda^{238}\text{U}/\lambda^{230}\text{Th}$	0.00001685	^{232}Th 232.0382									
^{230}Th conc. spike (nmol/g)*	6.0615	^{230}Th 230.0331									
Decay const. for ^{232}Th	4.9475E-11	^{208}Pb 207.9766									
Fractionation $^{230}\text{Th}/^{232}\text{Th}$, meas.	0.998										
Th blank (g)	4.00E-12	Avagadro's # 6.02252E+23									
Th blank (nmol)	1.72385E-05										
Batch ID	849-4	849-5	849-6	849-7	849-8	849-9	849-10				
Project#	Z4093	Z4091	Z4091	Z4091	Z4091	Z4094	Z4094				
Sample#	DG-136-95	DG-105-95	DG-105-95	DG-105-95	DG-105-95	DG-122-95	DG-122-95				
Mineral fraction ID	M-4	M-1	M-2	M-3	M-4	M-1	M-2				
U conc. in sample (ppm)	4884.50	5577.50	6125.70	8084.20	5286.70	3430.20	5600.80				
$^{230}\text{Th}/^{232}\text{Th}$ measured	0.080804	0.097525	0.167657	0.135624	0.252921	0.070625	0.089477				
(U/Th) _{mineral} measured	0.13000	0.24125	0.20032	0.31521	0.43383	0.08959	0.10285				
$^{230}\text{Th}/^{232}\text{Th}$ sample, measured	0.0000021905	0.0000040651	0.0000033753	0.0000053113	0.0000073100	0.0000015096	0.0000017330				
weight of spike (g)	0.05891	0.0542	0.07289	0.06485	0.0531	0.06023	0.06775				
weight of sample (g)	0.0000281	0.0000348	0.0000206	0.0000270	0.0000249	0.0000322	0.0000201				
Radiogenic ^{208}Pb (nmol/g)	575.9386	362.2601	459.0815	414.9626	169.3629	475.929	667.5917				
Calculated U fractionation	0.0714	0.102	0.0639	0.101	0.0525	0.0996	0.109				
$^{208}\text{Pb}/^{204}\text{Pb}$ sample, measured	2722.3	5966.3	7315.9	7025.9	4527.7	12398	7724.2				
Calculation of Th concentration											
^{230}Th spike (nmol)	0.357082965	0.3285333	0.441822735	0.393088275	0.32186565	0.365084145	0.410666625				
($^{230}\text{Th}/^{232}\text{Th}$) _{f_{fact}} , corrected, meas.	0.080642392	0.09732995	0.167321686	0.135352752	0.252415158	0.07048375	0.089298046				
^{232}Th sample (nmol)	4.42769412	3.37515575	2.64008691	2.90376580	1.27476639	5.17943181	4.59848624				
^{232}Th conc. sample (nmol/g)	157850.0576	97126.7842	128471.3824	107746.4118	51195.4373	160851.9196	228780.4101				
Th conc. in sample (ppm)	36627.40371	22537.30742	29810.46957	25001.54903	11879.4708	37323.90257	53085.97856				
Age calculation											
$^{208}\text{Pb}/^{232}\text{Th}$	0.003648644	0.003729765	0.003573414	0.003851289	0.003308164	0.002958802	0.002918046				
Error (\pm 1 s.d. in % of ratio)	0.201	0.203	0.201	0.197	0.205	0.199	0.203				
Age (Ma)	73.61301	75.24663	72.09793	77.69362	66.75501	59.71568	58.89432				
Error (\pm 2 s.d. in Ma)	0.29584	0.30477	0.28966	0.30619	0.27412	0.23713	0.23928				

Appendix 3: Continued

Constants:								
	Atomic Weights							
	²³² Th	²³⁸ U / ²³⁰ Th						
	232.0382	230.0331						
	²⁰⁸ Pb							
	207.9766							
	Avagadro's #		6.02252E+23					
Batch ID	849-11	849-12	849_17a	849_17b	849_18	849-19	849-20	
Project#	Z4094	Z4094	Z4121	Z4121	Z4121	Z4121	Z4121	
Sample#	DG-122-95	DG-122-95	DG-118-95	DG-118-95	DG-118-95	DG-118-95	DG-118-95	
Mineral fraction ID	M-3	M-4	A _{experiment} #9	A _{experiment} #7	B _(error loading filament)	C	D	
U conc. in sample (ppm)	4151.00	9551.10	134.69	134.69	-0.12	362.35	433.45	
²³⁰ Th/ ²³² Th measured	0.071962	0.098628	208.80231	205.731836	745.465936	149.916	139.819011	
(U/Th) _{mineral} measured	0.070015808	0.087729105	1.645651384	1.612760878	-0.164966252	3.088204571	3.601196571	
²³⁰ Th/ ²³² Th sample, measured	0.0000011798	0.0000014782	0.0000277292	0.0000271750	-0.0000027797	0.0000520362	0.0000606802	
weight of spike (g)	0.0605	0.06388	0.0743	0.0743	0.0628	0.07534	0.05959	
weight of sample (g)	0.0000205	0.0000086	0.0000046	0.0000046	0.0000073	0.000005	0.0000042	
Radiogenic ²⁰⁸ Pb (nmol/g)	710.7821	1400.4278	28.3482	28.342	0.6382	40.0367	26.8214	
Calculated U fractionation	0.0848	0.1	0.0795	0.0795	0.0543	0.0983	0.0963	
²⁰⁸ Pb/ ²⁰⁴ Pb sample, measured	11078	18287	195.26	195.26	43.646	412.28	187.01	
Calculation of Th concentration								
²³⁰ Th spike (nmol)	0.36672075	0.38720862	0.45036945	0.45036945	0.3806622	0.45667341	0.361204785	
(²³⁰ Th/ ²³² Th) _{f_{fact} corrected} , meas.	0.071818076	0.098430744	208.3847054	205.3203723	743.9750041	149.616168	139.539373	
²³² Th sample (nmol)	5.10598351	3.93347871	0.00158162	0.00161387	0.00002177	0.00246443	0.00212353	
²³² Th conc. sample (nmol/g)	249072.3663	457381.2453	343.8297	350.8421	2.9817	492.8865	505.6027	
Th conc. in sample (ppm)	57794.43991	106130.2347	79.78604672	81.41319645	0.691858116	114.380407	117.3333884	
Age calculation								
²⁰⁸ Pb/ ²³² Th	0.002853717	0.003061839	0.082448378	0.080782777	0.214040932	0.081229041	0.053048368	
Error (± 1 s.d. in % of ratio)	0.200	0.209	3.183	2.000	12.082	0.987	5.859	
Age (Ma)	57.59784	61.79204	1601.32373	1570.19853	3920.25081	1578.54259	1044.75322	
Error (± 2 s.d. in Ma)	0.22989	0.25866	101.95092	62.79803	947.29776	31.15991	122.42589	

Appendix 3: Concluded

Constants:								
$^{232}\text{Th}/^{230}\text{Th}$ spike	0.001287	Atomic Weights						
$\lambda^{238}\text{U}/\lambda^{230}\text{Th}$	0.00001685	^{232}Th	232.0382					
^{230}Th conc.spike (nmol/g)*	6.0615	^{230}Th	230.0331					
Decay const. for ^{232}Th	4.9475E-11	^{208}Pb	207.9766					
Fractionation $^{230}\text{Th}/^{232}\text{Th}$, meas.	0.998							
Th blank (g)	4.00E-12	Avagadro's #		6.02252E+23				
Th blank (nmol)	1.72385E-05							
Batch ID	849-21	849-22	849-23	849-24	849-25	849-26	849-27	
Project#	Z4121	Z4121	Z4121	Z4121	Z4096	Z4096	Z4096	
Sample#	DG-118-95	DG-118-95	DG-118-95	DG-118-95	DG-107-95	DG-107-95	DG-107-95	
Mineral fraction ID	E	F	G	H _(Th fractionated badly)	I	J	K	
U conc. in sample (ppm)	352.96	108.96	391.94	326.88	537.94	367.71	757.50	
$^{230}\text{Th}/^{232}\text{Th}$ measured	83.262885	118.772659	60.409979	155.289853	177.21693	325.994734	216.034517	
(U/Th) _{mineral} measured	1.55607	1.81504	1.53293	4.56924	57.12502	51.64111	67.41238	
$^{230}\text{Th}/^{232}\text{Th}$ sample, measured	0.0000262197	0.0000305834	0.0000258298	0.0000769916	0.0009625566	0.0008701528	0.0011358987	
weight of spike (g)	0.05851	0.06867	0.05791	0.06239	0.07532	0.07485	0.07204	
weight of sample (g)	0.000004	0.0000118	0.000005	0.0000065	0.0000504	0.0000271	0.0000310	
Radiogenic ^{208}Pb (nmol/g)	85.5323	22.2918	92.6962	26.6465	0.1151	0.0635	0.117	
Calculated U fractionation	0.0745	0.0899	0.08	0.086	0.0667	0.0871	0.0995	
$^{208}\text{Pb}/^{204}\text{Pb}$ sample, measured	452.64	502.66	1307.2	414.22	45.867	41.2	44.965	
Calculation of Th concentration								
^{230}Th spike (nmol)	0.354658365	0.416243205	0.351021465	0.378176985	0.45655218	0.453703275	0.43667046	
($^{230}\text{Th}/^{232}\text{Th}$) _{fraction, corrected} , meas.	83.09635923	118.5351137	60.28915904	154.9792733	176.8624961	325.3427445	215.602448	
^{232}Th sample (nmol)	0.00381157	0.00297582	0.00537051	0.00195327	0.00199008	0.00080927	0.00146011	
^{232}Th conc. sample (nmol/g)	952.8935	252.1883	1074.1011	300.5024	39.4858	29.8623	47.1005	
Th conc. in sample (ppm)	221.1192833	58.52089243	249.2453601	69.7387672	9.179878181	6.941275448	10.95399113	
Age calculation								
$^{208}\text{Pb}/^{232}\text{Th}$	0.089760610	0.088393484	0.086301188	0.088673178	0.002914975	0.002126427	0.002484052	
Error (\pm 1 s.d. in % of ratio)	0.599	0.294	0.234	4.073	13.641	38.614	15.653	
Age (Ma)	1737.40370	1712.03115	1673.13835	1717.22460	58.83243	42.93419	50.14597	
Error (\pm 2 s.d. in Ma)	20.81230	10.08262	7.81906	139.89427	16.05084	33.15743	15.69831	

Appendix 4. Calculations for corrected U loss Pb/U and/or Pb/Th ages

Constants: $\lambda_{238} = 1.5513\text{E-}10 \text{ a}^{-1}$ $\lambda_{235} = 9.8485\text{E-}10 \text{ a}^{-1}$ $\lambda_{232} = 4.9475\text{E-}11 \text{ a}^{-1}$													
Batch ID	844-25	844-26	844-27	844-28	849-1	849-2	849-3	849-4					
Project#	DAN#1	DAN#1	DAN#1	DAN#1	Z4093	Z4093	Z4093	Z4093					
Sample#	DG-167-95	DG-167-95	DG-167-95	DG-167-95	DG-136-95	DG-136-95	DG-136-95	DG-136-95					
Mineral Fraction ID	M-1	M-2	M-3	M-4	M-1	M-2	M-3	M-4					
U/Th mineral, model ^a	0.116219	0.103765	0.1109634	0.114514	0.13072	0.11641	0.13024	0.13740					
U/Th mineral, measured	0.11604	0.10313	0.11094	0.11450	0.12440	0.11190	0.12367	0.13000					
% Difference: measured vs. model	0.15053	0.61391	0.02430	0.01242	5.07686	4.03763	5.31753	5.69259					
Loss of U or Th	U loss	U loss	U loss	U loss	U loss	U loss	U loss	U loss					
Th conc. sample (ppm)	43197.222	56157.669	35978.712	38862.309	38212.550	38984.038	30607.175	36627.404					
Th sample (nmol)	11.337406	12.125157	15.35046	18.523554	4.9486994	2.7049129	2.5128052	4.4277143					
U conc. sample (ppm)	5142.20	5941.20	4094.40	4571.00	4876.50	4474.80	3882.80	4884.50					
U sample (nmol)	1.3156374	1.2504947	1.7029246	2.1239109	0.6156341	0.3026701	0.3107491	0.5756028					
Weight of sample (g)	0.0000609	0.0000501	0.0000990	0.0001106	0.0000301	0.0000161	0.0000191	0.0000281					
New U (nmol) using % difference	1.3176181	1.2581718	1.7033387	2.1212103	0.6468890	0.3148908	0.3272734	0.6083696					
New ²³⁵ U conc. (nmol/g)	155.787	180.827	123.887	138.098	155.005	140.830	123.702	156.169					
Conc. ²⁰⁷ Pb (nmol/g)	9.484	10.9692	7.504	8.403	11.2425	9.0581	9.0486	11.7141					
New ²³⁸ U conc. (nmol/g)	21479.976	24932.383	17081.554	19041.017	21372.084	19417.605	17056.003	21532.587					
²⁰⁶ Pb conc. (nmol/g) ^b	199.71299	232.44325	158.0528	176.11065	237.3555	191.7683	191.8387	247.2285					
Corrected ²⁰⁷ Pb/ ²³⁵ U	0.0608778	0.0606614	0.0605713	0.0608479	0.0725299	0.0643195	0.0731485	0.0750091					
Corrected ²⁰⁷ Pb/ ²³⁵ U error (1 σ) ^c	0.1870000	0.2250000	0.1810000	0.1820000	0.3659155	0.2727974	0.3105149	0.2729933					
Corrected ²⁰⁷ Pb/ ²³⁵ U age (Ma)	60.00577	59.79863	59.71234	59.97713	71.09741	63.29455	71.68284	73.44177					
$\pm 2 \sigma$ error on age (Ma)	0.22442	0.26909	0.21616	0.21832	0.52031	0.34533	0.44517	0.40098					
Corrected ²⁰⁶ Pb/ ²³⁸ U	0.0092976	0.0093229	0.0092528	0.0092490	0.0111059	0.0098760	0.0112476	0.0114816					
Corrected ²⁰⁶ Pb/ ²³⁸ U error (1 σ) ^c	0.11	0.151	0.098	0.087	0.3048166	0.2318694	0.2495325	0.2271329					
Corrected ²⁰⁶ Pb/ ²³⁸ U age (Ma)	59.65949	59.82115	59.37334	59.34894	71.19838	63.35248	72.10181	73.59345					
$\pm 2 \sigma$ error on age (Ma)	0.13125	0.18066	0.11637	0.10327	0.43405	0.29379	0.35983	0.33431					

^a As determined from radiogenic daughter products of U and Th. (U/Th)_{model} values that have been corrected for excess ²⁰⁶Pb

have been included in the calculations for DG-167-95 and DG-122-95.

^b Corrected ²⁰⁶Pb (nmol/g) values from Appendix 4 are used in DG-167-95 and DG-122-95.

^c For DG-167-95 and DG-122-95 the ²⁰⁷Pb/²³⁵U and ²⁰⁶Pb/²³⁸U error = sqrt [(corrected ²⁰⁶Pb error (Appendix 4))² + (original Pb/U error)²].

Appendix 4. continued

Batch ID	849-5	849-6	849-7	849-8	849-9	849-10	849-11	849-12
Project#	Z4091	Z4091	Z4091	Z4091	Z4094	Z4094	Z4094	Z4094
Sample#	DG-105-95	DG-105-95	DG-105-95	DG-105-95	DG-122-95	DG-122-95	DG-122-95	DG-122-95
Mineral Fraction ID	M-1	M-2	M-3	M-4	M-1	M-2	M-3	M-4
U/Th mineral, model	0.24166	0.19861	0.33311	0.46598	0.0925248	0.1051104	0.0714967	0.088055
U/Th mineral, measured	0.24125	0.20032	0.31521	0.43383	0.08959	0.10285	0.0700158	0.0877291
% Difference: measured vs. model	0.17112	0.85927	5.67926	7.41212	3.27531	2.19882	2.11515	0.37145
Loss of U or Th ^d	U loss	Th loss	U loss	U loss	U loss	U loss	U loss	U loss
Th conc. sample (ppm)	22537.307	29810.470	25001.549	11879.471	37323.903	53085.979	57794.44	106130.23
Th sample (nmol)	3.3751838	2.6401052	2.9037971	1.2747852	5.1794483	4.598503	5.1059964	3.933491
U conc. sample (ppm)	5577.50	6125.70	8084.20	5286.70	3430.20	5600.80	4151.00	9551.10
U sample (nmol)	0.8142623	0.5288561	0.9153049	0.5530367	0.4640291	0.4729509	0.3575004	0.3450816
Weight of sample (g)	0.0000348	0.0000206	0.0000270	0.0000249	0.0000322	0.0000201	0.0000205	0.0000086
New Th or U (nmol) using % difference	0.8156558	2.662790	0.9672875	0.5940285	0.4792276	0.4833503	0.3650621	0.3463634
New ²³² Th or ²³⁵ U conc. (nmol/g)	169.010	129573.995	258.438	171.778	107.163	173.151	128.225	289.997
Conc. ²⁰⁸ or ²⁰⁶ Pb (nmol/g)	13.0576	459.0815	20.6566	11.7531	6.5109	10.3074	7.3514	18.1796
New ²³⁸ U conc. (nmol/g)	23303.099	N/A	35633.491	23684.788	14775.682	23874.128	17679.683	39984.821
²⁰⁶ Pb conc. (nmol/g)	273.7298	N/A	432.2506	246.7662	137.2954	218.8127	158.5323	384.3806
Corrected ²⁰⁸ or ²⁰⁷ Pb/ ²³² Th or ²³⁵ U	0.0772593	0.0035430	0.0799285	0.0684202	0.0607568	0.0595282	0.0573320	0.0626889
Corrected error (1 σ %)	0.2124298	0.2750876	0.1996422	0.2102165	0.0980000	0.1100000	0.1210000	0.1020000
Corrected age (Ma)	75.56497	71.48549	78.07772	67.19915	59.88993	58.71324	56.60631	61.73769
$\pm 2 \sigma$ error on age (Ma)	0.32104	0.39330	0.31175	0.28253	0.11738	0.12917	0.13699	0.12594
Corrected ²⁰⁶ Pb/ ²³⁸ U	0.0117465	N/A	0.0121305	0.0104188	0.0092920	0.0091653	0.0089669	0.0096132
Corrected ²⁰⁶ Pb/ ²³⁸ U error (1 σ %)	0.2038956	N/A	0.1916299	0.2045433	0.059	0.076	0.067	0.072
Corrected ²⁰⁶ Pb/ ²³⁸ U age (Ma)	75.28150	N/A	77.72748	66.81619	59.62339	58.81399	57.54686	61.67446
$\pm 2 \sigma$ error on age (Ma)	0.30699	N/A	0.29790	0.27334	0.07036	0.08940	0.07711	0.08881

^d U or Th (nmol) corrected depending on determination of whether loss of U or Th occurred; subsequent calculations are based on this premise.

Appendix 4. continued

Batch ID	849_17a	849_17b	849-19	849-20	849-21	849-22	849-23	849-24
Project#	Z4121	Z4121	Z4121	Z4121	Z4121	Z4121	Z4121	Z4121
Sample#	DG-118-95	DG-118-95	DG-118-95	DG-118-95	DG-118-95	DG-118-95	DG-118-95	DG-118-95
Mineral Fraction ID	A _{experiment #9}	A _{experiment #7}	C	D	E	F	G	H
U/Th mineral, model	1.530222	1.530222	3.095017	5.252101	1.422678	1.587050	0.783699	2.320724
U/Th mineral, measured	1.645651	1.612761	3.088205	3.601197	1.556067	1.815037	1.532929	4.569235
% Difference: measured vs. model	7.54332	5.39392	0.22060	45.84321	9.37595	14.36551	95.60169	96.88834
Loss of U or Th	Th loss	Th loss	U loss	U loss	Th loss	Th loss	Th loss	Th loss
Th conc. sample (ppm)	79.78605	81.41320	114.38041	117.33339	221.1193	58.52089	249.2454	69.73877
Th sample (nmol)	0.0015817	0.00161396	0.0024647	0.0021238	0.0038118	0.002976	0.0053708	0.0019536
U conc. sample (ppm)	134.6900	134.6900	362.35	433.45	352.96	108.96	391.94	326.88
U sample (nmol)	0.00260293	0.00260293	0.0076115	0.0076482	0.0059314	0.0054016	0.0082233	0.0089263
Weight of sample (g)	0.000046	0.000046	0.000005	0.000042	0.000004	0.0000118	0.000005	0.0000065
New Th or U (nmol) using % difference	0.001701	0.001701	0.0076283	0.0111544	0.004169	0.003404	0.010505	0.003846
New ²³² Th or ²³⁵ Th or U conc. (nmol/g)	369.780	369.780	10.985	19.123	1042.273	288.429	2101.033	591.735
Conc. ²⁰⁸ Pb or ²⁰⁶ Pb (nmol/g)	28.3482	28.3482	46.0928	52.0486	85.5323	22.2918	92.6962	26.6465
New ²³⁸ U conc. (nmol/g)	N/A	N/A	1514.666	2636.676	N/A	N/A	N/A	N/A
²⁰⁶ Pb conc. (nmol/g)	N/A	N/A	424.863	482.749	N/A	N/A	N/A	N/A
Corrected ²⁰⁷ Pb/ ²³⁵ U	0.0766623	0.0766623	4.1958266	2.7217831	0.0820632	0.0772869	0.0441193	0.0450311
Corrected ²⁰⁷ Pb/ ²³⁵ U error (1 σ %)	4.45944155	2.76048218	0.9524774	5.8227613	0.8083384	0.3480876	0.3111180	5.7536905
Corrected ²⁰⁷ Pb/ ²³⁵ U age (Ma)	1492.99221	1492.99221	1673.20479	1334.41933	1594.13024	1504.71463	872.63859	890.28113
$\pm 2 \sigma$ error on age (Ma)	133.15823	82.42757	31.87380	155.40010	25.77193	10.47545	5.42987	102.44804
Corrected ²⁰⁶ Pb/ ²³⁸ U	N/A	N/A	0.2804996	0.1830900	N/A	N/A	N/A	N/A
Corrected ²⁰⁶ Pb/ ²³⁸ U error (1 σ %)	N/A	N/A	0.9518788	5.8231364	N/A	N/A	N/A	N/A
Corrected ²⁰⁶ Pb/ ²³⁸ U age (Ma)	N/A	N/A	1593.87778	1083.83332	N/A	N/A	N/A	N/A
$\pm 2 \sigma$ error on age (Ma)	N/A	N/A	30.34357	126.22619	N/A	N/A	N/A	N/A

Appendix 4. concluded

Batch ID	849-25	849-26	849-27
Project#	Z4096	Z4096	Z4096
Sample#	DG-107-95	DG-107-95	DG-107-95
Mineral Fraction ID	I	J	K
U/Th mineral, model	55.218112	67.934783	75.930144
U/Th mineral, measured	57.125019	51.641113	67.412384
% Difference: measured vs. model	3.45341	31.55174	12.63530
Loss of U or Th	Th loss	U loss	U loss
Th conc. sample (ppm)	9.17988	6.94128	10.953991
Th sample (nmol)	0.00199392	0.00081068	0.0014634
U conc. sample (ppm)	537.94	367.71	757.50
U sample (nmol)	0.11390278	0.04186438	0.0986539
Weight of sample (g)	0.0000504	0.0000271	0.0000310
New U (nmol) using % difference	0.002063	0.0550733	0.1111191
New ²³⁵ U conc. (nmol/g)	40.927	14.633	25.810
Conc. ²⁰⁷ Pb (nmol/g)	0.1151	0.6566	1.3666
New ²³⁸ U conc. (nmol/g)	N/A	2017.593	3558.678
²⁰⁶ Pb conc. (nmol/g)	N/A	13.510	27.864
Corrected ²⁰⁷ Pb/ ²³⁵ U	0.0028123	0.0448713	0.0529485
Corrected ²⁰⁷ Pb/ ²³⁵ U error (1 σ %)	13.6747736	9.9448612	2.1056010
Corrected ²⁰⁷ Pb/ ²³⁵ U age (Ma)	56.76291	44.56893	52.38803
$\pm 2 \sigma$ error on age (Ma)	15.52440	8.86464	2.20617
Corrected ²⁰⁶ Pb/ ²³⁸ U	N/A	0.0066959	0.0078298
Corrected ²⁰⁶ Pb/ ²³⁸ U error (1 σ %)	N/A	9.9198598	2.1018507
Corrected ²⁰⁶ Pb/ ²³⁸ U age (Ma)	N/A	43.02067	50.27731
$\pm 2 \sigma$ error on age (Ma)	N/A	8.53518	2.11351

Appendix 5 Minerals identified in thin section and hand specimen

Sample	Unit, Lithology	Quartz	Plagioclase	K-feldspar	Muscovite	Biotite	Chlorite	Garnet	Kyanite	Sillimanite	Andalusite	Calcite	Hornblende	Actinolite	Tourmaline	Pyroxene	Epidote	Apatite	Zircon	Monazite	Rutile	Titanite	Opakes
DG-105-95	7P, Pelitic schist	X	X		X	X		X	X								X		X	X			X
R224 ^a	7P, Pelitic schist	X	X	X	X	X	X	X	X		X						X	X	X				X
RS183 ^a	7P, Pelitic schist	X	X	X	X	X	X	X	X	X	X				X								X
RS20 ^a	7P, Pelitic schist	X	X		X	X	X	X	X	X	X									X			X
DG-136-95	7P, Pelitic schist	X	X	X		X		X	X	X											X		X
DG-167-96	7P, Pelitic schist	X	X		X	X		X	X	X	X										X		X
DG-122-95	11P, Pelitic schist	X	X		X	X		X	X		X									X			X
R140 ^a	11P, Pelitic schist	X	X	X	X	X	X		X		X								X				X
R20 ^b	11P, Pelitic schist	X	X		X	X	X	X	X	X	X							X	X	X			X
R36 ^b	11P, Pelitic schist	X	X		X	X	X	X	X		X							X	X	X			X
DG-118-95	9Q, Felsic Pyroclastic	X	X					X					X	X		X		X	X	X		X	X
DG-107-95	9Q, Mafic dyke	X	X		X	X	X	X				X				X		X	X	X		X	X

^a All mineral assemblages for samples beginning with 'R' were previously identified by Scammell (1986) in thin section and hand specimen. These samples were chosen based on their proximity to samples examined in this study (in bold).

^b Samples from Scammell (1986) that are not spatially close to samples in this study (i.e., DG-122-95), but are from the same lithologic unit (unit 11P).